

Dissertation
submitted to the
Combined Faculties of the Natural Sciences and Mathematics
of the Ruperto-Carola University of Heidelberg, Germany
for the degree of
Doctor of Natural Sciences

Put forward by
Anton Prosekin
born in: Sterlitamak, Russia
Oral examination: 3rd July, 2013

Propagation and radiation of
ultrarelativistic particles in magnetic fields
in different astrophysical environments

Referees: Prof. Dr. Felix Aharonian
Prof. Dr. Stefan Wagner

Zusammenfassung

Diese Doktorarbeit stellt die Ergebnisse der theoretischen Untersuchungen verschiedener Szenarien für die Ausbreitung und Strahlung ultrarelativistischer Teilchen in Abhängigkeit von den sie umgebenden Magnet- und Strahlungsfelder dar.

Im ersten Teil wird, ausgehend von einer analytischen Lösung der Boltzmann-Gleichung in der Näherung für kleine Winkel, eine genaue Berechnung der Winkel-, Energie- und Zeitverteilungen der ultra-energiereichen Protonen, der durch Synchrotronstrahlung von sekundären Elektronen und Positronen erzeugten Gammastrahlung sowie der sekundären Neutrinos von den Quellen der kosmischen Strahlung dargestellt unter Berücksichtigung einer Magnetfeldumgebung der Stärke $B \sim 10^{-9}$ G.

Der zweite Teil behandelt die Erklärung der TeV-Gamma-Strahlung von fernen Blazaren durch sekundäre Gammastrahlung von kosmischer Strahlung entlang der Sichtlinie bei Anwesenheit schwacher Magnetfelder der Stärke $B \sim 10^{-15}$ G. Wir haben dabei die Möglichkeit der Entdeckung von TeV-Strahlung von Blazaren mit Rotverschiebungen größer als $z = 1$ untersucht.

Schliesslich wird im letzten Kapitel die Strahlung geladener Teilchen in den extrem starken Magnetfelder von kompakten Objekten wie Pulsar und schwarzes Loch untersucht. Wir haben dabei die Bereiche und den Übergang zwischen Synchrotron- und Krümmungsstrahlung analysiert und die starke Empfindlichkeit der Strahlungsspektren vom Steigungswinkel (pitch angle) aufgezeigt.

Abstract

The thesis work presents the results of theoretical studies of different scenarios for the propagation and the radiation of ultrarelativistic particles depending on the environment determined by the magnetic and low energy radiation fields.

First, using the analytical solution of Boltzmann equation in the small-angle approximation, we have accurately calculated the angular, energy, and time distributions of the ultrahigh energy protons, gamma rays produced by synchrotron radiation of secondary electrons and positrons, and secondary neutrinos from the source of cosmic rays embedded in the magnetized environment of the level of $B \sim 10^{-9}$ G.

The second part considers the scenario explaining TeV gamma radiation from distant blazars by secondary gamma rays produced by cosmic rays along the line of sight in the weak magnetic field of the level of $B \sim 10^{-15}$ G. We have studied the possibility of detection of TeV radiation from blazars with redshifts greater than $z = 1$.

Finally, the last chapter of the work is addressed to the radiation of charged particles in the extremely strong magnetic fields of compact objects such as pulsar and black hole. We have studied the synchrotron and curvature radiation regimes and transition between them showing the strong sensitivity of radiation spectra on the pitch angle.

Contents

| | | |
|----------|--|-----------|
| 1 | Introduction | 1 |
| 1.1 | Ultrahigh energy cosmic rays | 1 |
| 1.2 | Sources of UHE cosmic rays | 5 |
| 1.3 | Intergalactic magnetic field | 7 |
| 1.4 | Multi-messenger approach | 8 |
| 1.5 | Synchrotron gamma rays | 10 |
| 1.6 | Small-angle approximation | 12 |
| 2 | Gamma-ray signatures of UHE cosmic-ray propagation | 13 |
| 2.1 | Steady state distribution functions | 13 |
| 2.2 | The spectral and angular distributions of protons, photons and neutrinos | 18 |
| 2.2.1 | Protons | 18 |
| 2.2.2 | Electrons | 25 |
| 2.2.3 | Gamma rays and neutrinos | 29 |
| 2.3 | An impulsive source: arrival time distributions | 34 |
| 2.4 | Discussion | 38 |
| 2.5 | Summary | 40 |
| | Appendix A: The Green function for spherically symmetric source | 41 |
| | Appendix B: Distribution function of electrons | 42 |
| | Appendix C: Distribution of arrival times in the case of "impulsive" source . . | 44 |
| | Appendix D: Emissivity function of synchrotron radiation in random magnetic fields | 49 |
| 3 | Cosmologically distant UHE cosmic-ray accelerators | 51 |
| 3.1 | Cosmologically distant sources | 51 |
| 3.2 | Energy budget | 52 |
| 3.3 | Gamma-ray source | 56 |
| 3.4 | X-ray emission | 57 |
| 3.5 | Discussion | 60 |
| 3.6 | Summary | 61 |
| | Appendix: Angular size of sources at large redshifts | 61 |

| | | |
|----------|--|------------|
| 4 | The case of weak intergalactic magnetic fields | 64 |
| 4.1 | Time structure of gamma-ray signals | 64 |
| 4.2 | Basic estimates and scaling laws | 67 |
| 4.3 | Semi-analytical description | 70 |
| 4.4 | Numerical Monte-Carlo calculations | 77 |
| 4.5 | Discussion | 79 |
| 4.6 | TeV gamma rays from distant blazars | 85 |
| 4.7 | Rectilinear propagation and deflections | 87 |
| 4.8 | Energy requirements | 89 |
| 4.9 | Case study: a blazar at $z = 1.3$ | 92 |
| 4.10 | Discussion | 95 |
| 4.11 | Summary | 96 |
| | Appendix: Distribution function in the expanding space | 97 |
| 5 | Synchrocurvature radiation in a strong magnetic field | 103 |
| 5.1 | Introduction | 103 |
| 5.2 | General comments | 104 |
| 5.3 | Local trajectory | 107 |
| 5.4 | Radiation spectrum | 109 |
| 5.5 | Numerical implementation | 111 |
| 5.6 | Astrophysical implications | 113 |
| | 5.6.1 Outer Gap | 113 |
| | 5.6.2 Polar Cap | 120 |
| | 5.6.3 Protons in the Black Hole magnetosphere | 121 |
| 5.7 | Summary | 126 |
| | Appendix: Energy losses in the quantum regime | 130 |
| | Bibliography | 133 |

1 Introduction

1.1 Ultrahigh energy cosmic rays

Ultrahigh energy (UHE) cosmic rays are charged particles with energies $E \gtrsim 10^{18}$ eV. The detection of cosmic rays of such energies is a quite rare event. Following the general trend (with some variations) of changing the flux with energy $\sim E^{-2.7}$, the UHE cosmic rays come with rate about 1 particle per km^2 per century at $\sim 10^{20}$ eV [1, 2, 3]. The main strategy to increase the possibility of registration is construction of detectors with the large area and time exposure. The feasible way to meet this requirement is ground-based arrays of detectors or fluorescence telescopes which use the atmosphere as a part of a detector [4, 5]. The collision of UHE particle with air matter produces the cascade of secondary particles called extensive air shower. The array of detectors collect the secondary particles determining the energy and the arrival direction. The fluorescence telescopes detect the radiation from the ionized and excited gas molecules produced during propagation of charged particles of the air shower. The detection of the event using both techniques allows to reconstruct the arrival direction more accurately. Unfortunately, the combined events have smaller statistics [6].

Thus the detection of UHE cosmic rays is indirect. This creates additional difficulties in the determination not only the energy and direction but even the type of the detected particle. All this uncertainties along with low statistics result in quite contradictory reports from different observatories detecting UHE cosmic rays. In some cases the picture becomes unclear because the conflicting trends are consistent within systematic uncertainties, as it has happened with mystery of the heavy nuclei composition at highest energies detected by Auger [7, 8, 9]. At the same time the problem of chemical composition is a very important question from the point of view of particle physics. The study of extensive air showers allows investigation of the interactions for currently non-reachable by accelerators range of energies. The conflict in the determination of chemical cosmic-ray composition may indicate that the models of interactions and cascade development for different primaries do not reflect the real physical situation. Therefore the astrophysical methods become important in clarification of this question. At relatively high statistics the combination of other two measurables - energy and small and large scale

anisotropies - may be very useful for the solution of this problem [10].

In spite of uncertainties even the general properties the UHE cosmic-ray flux imply the far-reaching conclusions. The existence of particles with $\sim 10^{20}$ eV by itself poses very important questions. First of all, it is the question of the acceleration mechanisms and the closely related to it the question of the possible astrophysical objects where these scenarios could be realised. The theoretical studies of these issues should not only explain existence of the detected highest energies but also predict the principle limit for maximum attainable energies in the known types of astrophysical sources. This will help to understand better the physics of these objects as well as their influence on the local environment and the evolution of the Universe as whole. However, to relate these issues to observations the problem of cosmic-ray propagation should be solved.

The propagation of cosmic rays in the interstellar and intergalactic medium is determined mainly by the interactions with radiation backgrounds and the influence of the magnetic fields [11, 12, 13, 14, 15, 16, 17]. The former affects the energy of cosmic rays whereas the latter has an effect on the direction of propagation. In the presence of magnetic fields the trajectory of charged particles becomes entangled and the reconstruction of the initial direction becomes difficult or impossible. Moreover, in most cases the traversed magnetic fields are very uncertain or unknown. Thus, the information which can help to distinguish the particular source is lost [18], although the energy of the particle can give some information about the type of the source.

Nevertheless, the extreme energies of UHE cosmic rays imply distinctive features which are advantageous compared with cosmic rays of lower energies. In spite of the poor knowledge of intergalactic magnetic fields we can claim that their strength is quite low. The models of magnetic field generation connect the strength with the density of the surrounding matter [16, 19]. It means that in the dilute medium of intergalactic space the strength of the magnetic fields is much smaller than the typical strength of the galactic magnetic fields. The different type of large-scale structures - from clusters of galaxies to superclusters and voids - should represent different levels of the intergalactic magnetic fields [20, 21, 22, 23]. Since the density of the large-scale structures varies for many orders of magnitude the value of the magnetic fields changes significantly for different environments as well. The upper limit of intergalactic magnetic fields outside clusters of galaxies is established on the level of several nanoGauss. This is about three order of magnitude lower than typical strength for normal galaxies and clusters of galaxies. Such level of magnetic fields allows cosmic rays propagate significant distances without large deflections. If the intergalactic magnetic field is much smaller than nG level the cosmic rays of lower energies could be potentially useful for realisation of so-called "cosmic-ray astronomy". But it should be noted that the galactic magnetic field would

have a significant impact on these cosmic rays. The combination of weak magnetic fields of the order of nG with large energy of cosmic rays $\sim 10^{20}$ eV leads to the giroradius of the order 100 Mpc which is of the order of size of elements of large-scale structure - filaments and voids. Thus UHE cosmic rays can traverse filaments preserving most of the information about their source. In voids the rectilinear character of propagation could be retained for much larger distances. Because the largest gravitationally bound structure is a cluster of galaxies, the magnetic fields of different clusters could not be correlated and the largest correlation length of intergalactic magnetic field should be of the order of size of typical galaxy cluster which is 1 Mpc. Thus the propagation of UHE cosmic rays on large distances has a character of small-angle diffusion where each scattering is induced by the next traversed cluster.

The approximate retention of the initial direction along with the detected distribution of arrival directions suggests the extragalactic nature of UHE cosmic-ray sources. Indeed, this distribution has isotropic character [24, 25]. If the sources locate inside the Galaxy, the arrival direction would be preferentially concentrated close to the Galactic plane. Moreover, the galactic magnetic field are not able to confine the UHE cosmic rays inside the Galaxy, since the their giroradius even in the relatively strong galactic magnetic field is still large than the size of the Galaxy. The last argument has to do with the acceleration to ultrahigh energies which is difficult to associate with the galactic sources and the overall energy budget of the Galaxy [26, 10].

The extragalactic nature of UHE cosmic rays increases the number of potential sources. Taking into consideration the increase of uncertainty for the determination of initial direction with distance, the discovery of the UHE cosmic-ray sources becomes more difficult problem. However, there is the second, independent, factor which is important for reduction of the number of observable sources. The interaction of UHE cosmic rays with cosmic microwave background (CMB) radiation leads to significant energy losses for particles with energies $\sim 10^{20}$ eV [27]. Thus the interaction establishes the "horizon" beyond which the particles of highest energies could not come. This reduces the number of potential sources of highest cosmic rays and increases the chances for their association with known astrophysical objects.

Unfortunately, in spite of the fact that UHE cosmic rays of $\sim 10^{20}$ eV presents such unique combination of properties for the identification of cosmic ray sources, their low flux restricts the realisation of "cosmic-ray astronomy". The recent observations reveals a steep decline above $3 \cdot 10^{19}$ eV in the cosmic ray spectrum [1, 2, 3]. This feature resembles the predicted end of the spectrum due to interaction with CMB called the Greisen-Zatsepin-Kusmin (GZK) cutoff [28, 29]. There is another possible explanation of the cutoff feature related to the maximum attainable energy at the acceleration.

Many acceleration models predict the maximum acceleration energy at the same energy domain where the GZK cutoff is expected. It is not excluded that the cutoff is the combination of both factors. The increase of statistics with the study of anisotropy of arrival directions as well as the improvement of the acceleration models will help to distinguish these two cases.

In addition to the energy changes, the interactions with background radiation fields introduces the changes of cosmic-ray chemical composition via different photo-disintegration processes. The main effect of these processes on the propagation of nuclei is that the light nuclei with mass number $A < 20$ cannot travel further than several tens of megaparsecs without being disintegrated [30]. After the propagation of the distance greater than ~ 50 Mpc only protons and iron nuclei survive. Thus the chemical composition of the observed UHE cosmic rays should be proton-iron mixture. The dominance of heavy nuclei at highest energies would be possible if the initial composition consists mostly of iron group nuclei. This could happen because the maximum energy of protons attainable at the accelerator is less than the energy of iron nuclei with larger electric charge. The observations of the shower maximum produced in atmosphere by UHE cosmic rays by most of the detectors indicate the predominately proton composition. The only exception from this tendency, which was mentioned above, is the unexplained change towards heavy primaries above 10^{19} eV in the data of Auger Observatory [7, 8, 9]. Therefore in the first approximation the study of UHE cosmic ray propagation can be restricted to consideration of pure proton composition.

Because the matter of intergalactic medium is very diluted the UHE cosmic rays interact mostly with the background radiation fields: cosmic microwave background (CMB) and extragalactic background light (EBL). For UHE cosmic rays the interaction with CMB radiation is dominant since it is more dense and less energetic. The EBL photons become more important for cosmic rays of lower energies. The UHE protons interact with background photons via pair production and photohadronic processes. The less energetic process is electron-positron pair production, also known as Bethe-Heitler process. This is an electromagnetic process of the electron-positron pair production by photon in the vicinity of charged nucleus. Thus it is relevant not only for protons but also for heavier nuclei. The pair production decreases the energy of heavy nucleus during propagation without change of mass number. The cross section of Bethe-Heitler process exceeds the cross section of photohadronic processes by 2 orders of magnitude [31, 32]. This results in more frequent interactions via pair production process. But since at each interaction the proton loses only a small ($\sim m_e/m_p$) part of the energy, the energy loss rate due to pair production process is much less than the energy loss rate due to photohadronic interactions.

The protons start interact with CMB photons via pair production at energy $\sim 10^{18}$ eV. The threshold for the photohadronic processes with CMB photons is $\sim 6 \cdot 10^{19}$ eV. At energies greater than this threshold the dominant energy losses are due to photohadronic processes. The photohadronic processes consist of several channels [33]. At low energies close to threshold the photon is absorbed by the nucleon exciting baryon resonance with its subsequent decay. The decay results in the production of nucleon and mesons most of which are pions. At the same energies the direct pion production occurs with smaller probability. At high energies the total cross section is approximately energy-independent and the interactions are dominated by inelastic multiparticle production. All secondary mesons are short-lived particles producing in the subsequent chain of decays electrons, positrons, gamma rays, and neutrinos of different flavours. Unlike the electromagnetic pair production the photohadronic interactions occurs quite rarely but the amount of energy lost at each collision is large varying from 13% at the threshold to about 40% at energies 10^{22} eV [31]. Thus the propagation of UHE cosmic rays is restricted by several interaction lengths relative to photohadronic processes. The average interaction length of protons is about ~ 10 Mpc. At every interaction the proton loses $\sim m_\pi/m_p \sim 15\%$ of its energy. Thus UHE protons can propagate in average the distance of 100 Mpc before lose their energy. More specifically, 90% of protons detected at energies $E \gtrsim 10^{20}$ eV have travelled less than 130 Mpc, whereas 90% of protons detected with energies $E \gtrsim 6 \cdot 10^{19}$ eV have not travelled more than 200 Mpc [34]. Therefore the sources of the detected cosmic rays should be located in our local Universe. The appearance of GZK feature in the cosmic-ray spectrum indicates the lack of relatively close sources of UHE cosmic rays. The distance to the sources should be of about several interaction lengths and the most of the sources of the detected cosmic rays should be located below the GZK horizon.

1.2 Sources of UHE cosmic rays

In the searching of sources of UHE cosmic rays the additional factor should be taken into account. The arrival directions of the detected cosmic rays should be correlated with the most powerful sources. The general considerations shows that the maximum possible energy of acceleration is in direct ratio with overall luminosity of the sources. The first condition that should be fulfilled is the so-called Hillas criterion which describes the sources parameters allowing to bound particles of maximum energy in the acceleration region. It arise from the fact that the size of the source should be larger that the giroradius of accelerated particle. Besides the size of the source there is another principle restrictive factor. The electromagnetic fields (mostly magnetic fields) are responsible

for radiation of the particles. The energy losses due to electromagnetic radiation is the lower limit factor which restraint the maximum acceleration energy. Additionally the interaction with matter in the source will increase the energy losses affecting on the maximum energy. The electromagnetic radiation could occur in two major regimes: synchrotron and curvature radiation. Since at the curvature radiation the energy losses is less energetic and the curvature of the magnetic field responsible for this radiation is connected to the size of the source, this mechanism could be considered for the estimation of optimal electromagnetic energy at the source. Thus combining the limiting factors of the radiation and the size of the source we can find the total electromagnetic energy in the acceleration region [26]

$$W \simeq \frac{1}{9} \frac{\sqrt{1 + \eta^2}}{\eta} \frac{E_{max}}{(mc^2)^4}, \quad (1.1)$$

where η is the ration of electric to magnetic strength which is typically less than unity. This estimate gives the value $W \simeq 3 \cdot 10^{51}$ erg for the maximum energy of protons $E_{max} = 10^{20}$ eV. Moreover, taking into account ultrarelativistic bulk motion the estimates favour to the gamma ray bursts (GRBs)[35, 36, 37] and active galactic nuclear jets(AGNs). In the latter type of sources the hadronic models are more preferential compared to the leptonic one. Here it should be mentioned that the magnetars is sometimes considered as an another candidate type of UHE cosmic-ray sources. The Ref. [10], comparing acceleration time with the dynamical time of the outflow, have estimated the luminosity of the source to accelerate the particles to $E_{max} = 10^{20} E_{20}$ eV as $L > 10^{45} Z^{-2} E_{20}^2$ erg/s.

The only sources which possess luminosities of $L > 10^{45}$ erg/s are FR II/FSRQ radio-galaxies. However the arrival directions of cosmic rays detected by the Auger mostly correspond to less energetic Seyfert galaxies in the nearby Universe < 75 Mpc and do not correlate with the local FR II galaxies. The possible reason for the discrepancy could be in the underestimation of the magnetic fields or the heavy nuclei composition. Also the AGN flares could meet the acceleration requirements of UHE cosmic rays being transient sources which are not easy to identify. Considering the low statistics it is more promising to search the correlation rather with large scale distribution of the matter in the local Universe than with individual sources. For example, the well-known clusterization of the Auger events around the closest AGN Centaurus A could be explained not only by the source itself but also by the Centaurus cluster which is located in the direction of Cen A but much further away [10].

1.3 Intergalactic magnetic field

The general picture of the magnetic field influence on the propagation of UHE cosmic rays have been discussed above. The details of the magnetic field generation and its influence on the cosmic-ray deflections is discussed here. From the observations of different galactic environments it is possible to extract information about Galactic magnetic fields. The Faraday rotation measurements of radio sources provide us with the information about the strength of magnetic fields in the direction parallel to the line of sight. The starlight polarisation data and synchrotron emission gives information about perpendicular component of the field. The Galactic magnetic field consist of the regular and the turbulent components. The regular component have the configuration similar to the structure of spiral arms of the Galaxy with the strength $\sim 3\mu G$ in the vicinity of the Earth[38]. The turbulent component is less certain and depends on the direction of observation. The regular component is responsible for the translation of the cosmic-ray source image as a whole whereas the turbulent component distorts this image. The study of their effect on the UHE cosmic-ray propagation indicates the deflections not greater than $\sim 10^\circ Z(40\text{EeV}/E)$ for the particle of charge Z and energy E .

The knowledge of the intergalactic magnetic field is less certain. The Faraday rotation measurements of the magnetic field in the core of clusters of galaxies give estimates of the level $\sim 1 - 40\mu G$. In the less dense environment outside clusters the upper limit for the intergalactic magnetic field is estimated as $\langle B_{\parallel}^2 \lambda \rangle \lesssim 10^{-8} \text{GMpc}^{1/2}$ with coherent length $\lambda \lesssim 1 \text{ Mpc}$ [39, 11]. For measurements of the lower of magnetic fields limit the gamma rays from blazars can be used. The propagation of high energy gamma rays is not free. Interacting with the low energy radiation background (mostly with EBL) they create electron-positron pairs. In their turn the electrons and positrons upscattering on CMB photons produce high energy gamma rays. Thus the electromagnetic cascade develops. Acting on the charged part of the electromagnetic cascade the intergalactic magnetic fields scatter the initial direction of the primary photon. This leads to the extended gamma-ray emission around point source and causes delays of gamma-ray flares. The electromagnetic cascade produces a lot of low energy gamma rays. The influence of the intergalactic magnetic fields on the low energy part of the cascade produces the suppression of the part of the spectrum. The value of this suppression is determined by the strength of intervening magnetic fields. The suppression of the flux as well as time delays have been used by different authors to establish the lower limits of the order of $B \sim 10^{-16} - 10^{-15} \text{ G}$ [40, 41, 42, 43]. The detection (although debatable, see Neronov2011) of the pair halos in the stacked images of a large number of sources has been revealed by Ref. [44].

The problem of the structure of the intergalactic magnetic fields is related to the question of their origin [45]. If the origin of the magnetic fields in the primordial Universe [46], they should permeate all structures being amplified in the dense regions due to dynamical effects of the large-scale structure formation. In the case of the magnetic pollution from galaxies the intergalactic magnetic fields should be concentrated mostly in the dense regions and highly suppressed in the voids [47]. In both cases the dynamical amplification plays important role but the final result considerably depends on the initial conditions which is provided by the origin of seeded magnetic fields. In the simulations of the large-scale structure of inhomogeneous intergalactic magnetic fields the different initial assumptions lead to different final structures and filling factors of the magnetic fields. Thus the simulations Refs. [39, 13] assumed the magnetic seeds generated by Biermann battery effect around accretion shocks whereas Ref. [14] seeded the homogeneous magnetic field at redshift $z \sim 20$. Consequently, the difference in the final magnetic fields causes the different influence on the propagation of the cosmic rays: for protons with energy $E > 100$ EeV Refs. [13] indicates the deflection of $10^\circ - 20^\circ$ whereas Ref. [14] gives the deflection of less than a degree. Another approach of inhomogeneous magnetic field modelling is the scaling of the strength with the density of underlying matter as it was done by Ref. [16].

1.4 Multi-messenger approach

Summing aforesaid, the interaction of cosmic rays with the background radiation restricts the cosmic-ray astronomy to the nearby Universe around 100 Mpc. The uncertainties in the knowledge of the intergalactic magnetic fields also limits the identification of the UHE cosmic rays. Having this in mind it becomes promising to use so-called multi-messenger approach. The interactions of UHE cosmic rays with CMB can provide us with the information about cosmic-ray propagation in the form of secondary gamma rays and neutrinos which are devoid of the drawback being deflected by intergalactic magnetic fields. The neutrino astronomy does not depend on the magnetic fields at all and the possibility of its realisation is related to the luminosity and spectrum of cosmic rays [48, 49]. The gamma-ray signal from the propagating UHE cosmic rays can originate from the different mechanisms depending on the strength of intergalactic magnetic fields. Because of the interaction with the radiation backgrounds the high energy gamma rays initiate electromagnetic cascades which are influenced by the magnetic fields deflecting electrons in the cascade. The detection of a strong signal from the cascade is possible in the case of weak magnetic fields of the order of $B \sim 10^{-15}$ G and less [50]. The magnetic field of such strength weakly deflect electrons over their effective interaction length,

therefore the most of the flux is concentrated along the initial direction of the primary gamma rays. The suppression of the flux would be observed at the low energy part of the gamma ray spectrum. From the other side, the flux at high energies depends on the distance from the origin of the cascade. For distances greater than several hundred Mpc the gamma-ray flux at TeV energies is significantly attenuated due to the conversion of these gamma rays to lower energy part of the cascade. Considering that the UHE cosmic rays convert the most of the energy to the secondary particles at first several tens of Mpc due to the photomeson production, the very distant sources will be observed only at low energy gamma rays and their flux will be attenuated due to deflection of the low energy part of the cascade[43]. From the other hand, if the most of the luminosity is in cosmic rays of $E < 10^{19}$ eV and the energy losses primarily due to pair production, the secondary gamma rays can be produced on much larger distances initiating the cascade closer to the observer. In this case the gamma rays of TeV energies could be observed from the distant sources from which the intrinsic TeV radiation should be considerably attenuated [51, 52, 53, 54]. This mechanism is not related to the identification of UHE cosmic-ray sources but it can explain the hard spectra of blazars and TeV radiation for the distant blazars as it is discussed in the Chapter II.

The electrons of the low energy part of the cascade become to be isotropized if the intergalactic magnetic field is stronger than $B \gg 10^{-14}$ G. The deflection angle in the cascade can be estimated as follows. The main contribution to the deflection comes from the lowest energy electrons. We can estimate the deflection angle of the electron producing the gamma rays with the energy E_γ induced by the magnetic field B over the effective inverse Compton cooling length in the Thomson regime. Then the deflection angle in the cascade is $\theta \approx 0.63^\circ (1\text{TeV}/E_\gamma)(B/10^{-14}\text{G})$. The full isotropization for TeV gamma rays begins at the magnetic field $B \sim 10^{-12}$ G. To estimate the the length of the cascade development one can notice that the cooling length of the electrons $E_e \sim 20$ TeV producing the gamma rays of the energy ~ 1 TeV is about tens of kpc. It is much smaller than the interaction length of their parent gamma rays which is about several tens of Mpc. Since the interaction length of the gamma rays relative to the pair production rapidly decreases with the increase of energy, the interaction length of the lowest energy gamma rays could be taken as the cascade development length. Thus the gamma rays of the energy 1 TeV are produced at the distance about several tens of Mpc from the particle initiating the cascade. Considering that the UHE cosmic rays produce the secondary particles initiating cascade at the distance about several tens of Mpc from their source, the final isotropized particles give a very dilute halo [55] contributing in this way to the extragalactic gamma-ray background radiation [56, 57, 58]. Even the conservative estimates shows that angular size of the halo is larger than the field of view

of Cherenkov telescopes and thus such halo would be hardly detectable [59].

1.5 Synchrotron gamma rays

The promising mechanism for the identification of UHE cosmic ray sources can operate if the intergalactic magnetic field is enough strong. The source embedded in the environment of the strong magnetic field could be seen in the synchrotron radiation of the secondary electrons produced by the UHE protons in photomeson interactions [60, 61, 17, 19, 62]. The galaxy clusters and filaments of the large-scale structure can provide the magnetic field of the order of $B \sim 10^{-9}$ G favourable for this scenario. The presence of the strong magnetic field is required only for the region $10 - 20$ Mpc around the source. In this case UHE cosmic rays lose a significant part of the energy producing secondary electrons, positrons, gamma rays, neutrinos inside this region. The electrons (positrons) radiate their energy in the form of synchrotron GeV gamma rays passing less than Mpc. The interaction length of the gamma rays produced in photomeson processes with the cosmic radio background is several Mpc. The electron-positron pair produced at this interaction also radiates synchrotron gamma rays. Thus the most of the energy lost by UHE protons is converted to the synchrotron radiation of secondary electrons on the distance of several Mpc. It is important to note that in photomeson interactions the secondary gamma rays are more energetic than electrons and positrons. At the interaction with the cosmic radio background the gamma rays transfer the most of the energy to the one component of the pair. Therefore the electrons(positrons) from the pair production are more energetic than the electrons and positrons produced in photomeson interactions.

For the realisation of the discussed scenario the two requirements concerning to the magnetic field should be fulfilled. The electron should emit most of its energy via synchrotron radiation. This situation occurs if the energy losses due to synchrotron radiation are dominant over the inverse Compton losses due to interaction with the CMB radiation. For the magnetic field $B = 10^{-9}$ G the regime of dominant synchrotron losses occurs for the electrons with energy $E_e \approx 10^{18}$ eV. The typical production energy for secondary particles is about 5% of the energy of the parent proton for electrons and positrons and 10% for the gamma rays. Taking into account the maximum energy of UHE protons $\sim 10^{21}$ eV one can find that there is no production of the electrons which would radiate predominantly via synchrotron mechanism if the magnetic field is less than $B \sim 10^{-10}$ G. This imposes the lower limit on the strength of magnetic field for the realisation of the mechanism under consideration. The upper limit is determined from the condition of the small deflections for charged particles. In the magnetic field of

the order of 10^{-7} G the UHE protons of $\sim 10^{20}$ eV have the giroradius about 1 Mpc. It means they are deflected at large angle before they interact and produce the secondary particles. In such magnetic field the electrons are isotropized before emission their energy in the initial direction. Therefore a lot of radiation is lost and the mechanism becomes less efficient. Additionally the radiation becomes more energetic and the synchrotron gamma rays start to interact with the background radiation initiating cascades which further dilute the gamma-ray flux.

In the favourable range of the magnetic field strength $B \sim 10^{-7} - 10^{-9}$ G the deflection of the UHE protons is small in the region of the photomeson production and the secondary electrons radiate most of their energy on the almost rectilinear part of the trajectory. Thus the synchrotron gamma rays have small deflection angles relative to the initial proton directions. The initial radial directions of the protons transforms to the narrow beam of gamma rays. Thus the source of UHE cosmic rays would appear as point-like source of gamma rays although the formation of the radiation occurs in the extended region.

The energy spectrum and flux of synchrotron radiation of secondary electrons from photomeson interactions of protons with CMB radiation have been studied in Ref. [61]. The calculations have been limited by the first 10 Mpc range of propagation of protons, assuming that at this stage protons propagate radially without significant deviations, and the secondary electrons move along the same direction before they emit synchrotron photons. While this approximation gives a correct estimate of the flux, it does not specify the angle within which the radiation is confined. This approach ignores also the non-negligible tails of distribution of synchrotron radiation formed at the later stages of propagation and interactions of protons.

In the case of quasi-continuous operation of an extragalactic accelerator of protons over timescales exceeding the typical delay time due to the deflection in the magnetic field, the energy and angular distributions of protons, as well as accompanying photons and electrons, can be accurately described by the steady-state solutions of the transport equations. Generally, this is the case of a continuous proton accelerator of age $T \geq 10^6$ yr. In the case of shorter activity of the source (an "impulsive accelerator") or solitary events like gamma-ray bursts, relatively simple analytical solutions of the arrival time distributions of protons, gamma-rays and neutrinos can be obtained within an approximation when the energy losses of protons are ignored. We consider the cases of "continuous" and "impulsive" proton accelerations in Sections 2.1 and 2.3, respectively.

1.6 Small-angle approximation

The realization of the small-angle multiple scattering considerably simplifies the description of propagation of protons through a scattering medium. In particular, in the small-angle approximation the term $\mathbf{v} \frac{\partial f}{\partial \mathbf{r}}$ of the Boltzmann transport equation can be presented in a form allowing analytical derivation of the steady state solution. Because of smallness of the single scattering angle one can write the elastic collision integral in the Fokker-Planck approximation. To expand the distribution function into series in terms of the single scattering angle one should have a smooth function of this angle. This condition is satisfied if one neglects unscattered part of the distribution function that has very sharp angle dependency. Such an approximation is justified in the case of multiple scattering.

The approach provides solutions that can be applied to the various cases which, independent of the details of the scattering medium, are characterized only by the average scattering angle per unit length $\langle \theta_s^2 \rangle$. The scattering process depends on the particle energy, i.e. $\langle \theta_s^2 \rangle$ is a function of energy. During the propagation through the medium between two scattering centers, the energy of particles is gradually decreased due to different dissipative processes. If the change of energy in each action of interaction is considerably smaller than the initial energy, one can use the continuous energy loss approximation. It should be noted that in the approach described here the processes responsible for the scattering and the energy loss of particle are not required to be the same. The particle scattering could have elastic character and do not cause energy losses. On the other hand, the effect of deflection of particles from their original direction due to the processes responsible for energy losses might be negligibly small. This is the case of the problem considered below. One can safely ignore the change of the direction of primary particles as well as the production angles ($\theta \sim 1/\gamma$) of the secondary products (gamma-rays, electrons, neutrinos) due to all relevant processes including photo-meson and pair production, inverse Compton scattering, synchrotron radiation.

2 Gamma-ray signatures of UHE cosmic-ray propagation

2.1 Steady state distribution functions

The aim of this section is to derive distribution functions for protons and accompanying them secondary particles propagating through the galactic and extragalactic magnetic fields for a spherically symmetric point source of protons. However, it is technically more convenient to consider first a source emitting protons in a given (fixed) direction. In this case we have a preferential direction along the infinitely narrow beam emitted by the source. Let us choose z-axis along this direction. Because of the scattering, particles deviate from the initial course. To define the deviation we introduce angles θ_x and θ_y between the direction of propagation \mathbf{n} and the coordinate planes YOZ and XOZ, respectively. If \mathbf{n} is close to z-axis, the angles θ_x and θ_y are small and can be treated as components of two-dimensional vector $\boldsymbol{\theta}$ in the XOY plane, where the absolute value of $\boldsymbol{\theta}$ corresponds to the deflection angle between \mathbf{n} and the z-axis. Then we can write $\mathbf{n} \approx (\theta_x, \theta_y, 1 - \frac{\theta^2}{2}) = (\boldsymbol{\theta}, 1 - \frac{\theta^2}{2})$.

The retention of the second-order term $\theta^2/2$ in the expansion of n_z allows us to take into account the effects relating to the elongation of the path like delay time, but does not give any considerable contribution to steady-state solution. Therefore we divide the problem into two sub-problems. In the first part of the chapter we solve the steady-state equation that takes into account the energy losses but ignores the elongation of particle trajectories. The results of these calculations are relevant to the "continuous" source of protons and describe the energy and angular distributions of protons and accompanying neutrinos and synchrotron radiation of secondary electrons produced during the propagation of protons. In the second part of the chapter we calculate the distributions of arrival times of protons, neutrinos and gamma-rays in the case of an "impulsive" source. In this case the arrival time delays directly depend on the elongation of trajectory. The time-dependent solutions for distribution functions presented in Section 2.3 are limited by the approximation in which the energy losses of protons are neglected.

Thus, to derive the steady-state solution of the transport equation we assume $\mathbf{n} \approx (\theta_x, \theta_y, 1) = (\boldsymbol{\theta}, 1)$. Let us denote by $\boldsymbol{\rho} = (x, y)$ the perpendicular displacement in the plane XOY. For a point source characterized by a monoenergetic and infinitely narrow beam of protons emitted along the z-axis we obtain the equation for Green function $G(\mathbf{r}, \boldsymbol{\theta}, E)$ of the Boltzmann steady-state transport equation in the approximations of a small-angle multiple scattering and continuous energy losses:

$$\left(\frac{\partial}{\partial z} + \boldsymbol{\theta} \frac{\partial}{\partial \boldsymbol{\rho}} - \frac{\langle \theta_s^2 \rangle}{4} \frac{\partial^2}{\partial \boldsymbol{\theta}^2} - \frac{\partial}{\partial E} \bar{\epsilon} \right) G(\mathbf{r}, \boldsymbol{\theta}, E, E_0) = \frac{1}{c} \delta(z) \delta(\boldsymbol{\rho}) \delta(\boldsymbol{\theta}) \delta(E - E_0). \quad (2.1)$$

Here we take into account that the particles are ultrarelativistic $|\mathbf{v}| = c$. The solution of Eq. (2.1) is obtained in Ref. [63] for the propagation of charged particles passing through a layer of matter. The features of this solution are comprehensively discussed in Ref. [64]. Using the notations introduced in Ref. [64], the Green function can be written in the form:

$$G(\mathbf{r}, \boldsymbol{\theta}, E, E_0) = \frac{\delta(S(E, E_0) - z)}{c \bar{\epsilon}(E) \pi^2 \Delta} \exp \left(- \frac{A_1 \boldsymbol{\rho}^2 - 2A_2 \boldsymbol{\theta} \boldsymbol{\rho} + A_3 \boldsymbol{\theta}^2}{\Delta} \right), \quad (2.2)$$

where S is the traveled distance that is uniquely related to the energy loss rate $\bar{\epsilon}(E) = |dE/dz|$:

$$S(E, E_0) = \int_E^{E_0} \frac{dE'}{\bar{\epsilon}(E')}, \quad (2.3)$$

and

$$\Delta = A_1 A_3 - A_2^2. \quad (2.4)$$

The δ -function in Eq. (2.2) points to the fact that we neglect the elongation of trajectory so the traveled distance is equal to z as if particles propagate strictly along z-axis. Taking the relation between energy and z into account, A_i can be written in the following form:

$$A_i(E_0, z) = \int_0^z \langle \theta_s^2 \rangle(z') (z - z')^{i-1} dz'. \quad (2.5)$$

It is easy to recognize the physical meanings of the coefficients A_1, A_2 and A_3 ; A_1 is the mean square deflection angle, A_3 is the mean square displacement, and A_2 is the mean value of $\boldsymbol{\theta} \boldsymbol{\rho}$ at the distance z :

$$A_1 = \langle \boldsymbol{\theta}^2 \rangle_z, \quad A_2 = \langle \boldsymbol{\theta} \boldsymbol{\rho} \rangle_z, \quad A_3 = \langle \boldsymbol{\rho}^2 \rangle_z. \quad (2.6)$$

For the treatment of the case of spherically symmetric point source of protons, let us rewrite Green function in the form which is independent of choice of the coordinate system. After the replacements

$$\boldsymbol{\theta} \rightarrow \boldsymbol{n} - \boldsymbol{n}_0, \quad \boldsymbol{\rho} \rightarrow \boldsymbol{r} - r\boldsymbol{n}_0, \quad z \rightarrow r, \quad (2.7)$$

where \boldsymbol{n}_0 is the direction of the emission, \boldsymbol{n} is the direction of particle motion at the point \boldsymbol{r} , we find

$$G(\boldsymbol{r}, \boldsymbol{n}, \boldsymbol{n}_0, E, E_0) = \frac{\delta(S(E, E_0) - r)}{c\bar{\epsilon}(E)\pi^2\Delta} \times \exp\left(-\frac{A_1(\boldsymbol{r} - r\boldsymbol{n}_0)^2 - 2A_2(\boldsymbol{r} - r\boldsymbol{n}_0)(\boldsymbol{n} - \boldsymbol{n}_0) + A_3(\boldsymbol{n} - \boldsymbol{n}_0)^2}{\Delta}\right). \quad (2.8)$$

Performing integration over all directions of the vector \boldsymbol{n}_0 by the saddle point method (see Appendix 2.5), we find

$$G_{sph}(r, \theta, E, E_0) = \frac{\delta(S(E, E_0) - r)}{c\bar{\epsilon}(E)r^2\pi D} \exp\left(-\frac{\theta^2}{D}\right), \quad (2.9)$$

where

$$D = A_1 - 2\frac{A_2}{r} + \frac{A_3}{r^2}. \quad (2.10)$$

Since we have spherically symmetric distribution, the Green function depends only on the distance r from the source and θ which is the angle between the radius-vector from the source to the observation point and the movement direction at this point.

We assume that the spherically symmetric source injects protons into the intergalactic medium with a constant rate:

$$Q_p(\boldsymbol{r}, E) = cJ_p(E)\delta(\boldsymbol{r}). \quad (2.11)$$

The substitution of this expression into

$$f(r, \theta, E) = \int Q(\boldsymbol{r}_0, E_0)G_{sph}(r - r_0, \theta, E, E_0)d\boldsymbol{r}_0dE_0 \quad (2.12)$$

gives

$$f_p(r, \theta, E) = \frac{1}{\bar{\epsilon}(E)} \int_E^\infty \frac{J_p(E_0)}{\pi r^2 D} \exp\left(-\frac{\theta^2}{D}\right) \delta(S(E, E_0) - r) dE_0, \quad (2.13)$$

where D can be written as

$$D(E_0, r) = \frac{1}{r^2} \int_0^r \langle \theta_s^2 \rangle (r') r'^2 dr'. \quad (2.14)$$

For the given energy and spatial distribution of protons we can calculate number of secondary particles from the decays of π -mesons that are produced at interactions between protons and 2.7 K CMBR photons. To obtain the energy distributions of the secondary products - photons, electrons and neutrinos, we use the approximation proposed in Ref. [31]. The energy of protons is ultrarelativistic so we can assume that secondary particles initially move in the same direction as protons. The distribution of second particles can be presented in the form

$$Q(r, \theta, E) = \hat{Q}(f_p(r, \theta, E_p)) \quad (2.15)$$

where \hat{Q} denotes an integral operator. For example, for the energy distribution of protons $J_p(E)$, the energy distribution of photons produced in photomeson interactions is

$$Q_\gamma(E_\gamma) = \hat{Q}_\gamma(J_p(E_p)), \quad (2.16)$$

where

$$\hat{Q}_\gamma(J_p(E_p)) = \int J_p(E_p) f_{ph}(\epsilon) w(E_\gamma, E_p, \epsilon) dE_p d\epsilon. \quad (2.17)$$

Here f_{ph} is the distribution function of CMBR photons, w is the differential interaction rate of the $p\gamma$ interactions, namely, the Bethe-Heitler pair production or photomeson production (see Ref. [31]). Since we are interested in the distribution of ultrarelativistic electrons that weakly deviate in the magnetic field, we can apply the Green function given by Eq. (2.8) to the source function given by Eq. (2.15). Note that \hat{Q} acts only on variable E_p , therefore we can change the order of integration. Tedious calculations (see Appendix 2.5) yield:

$$\begin{aligned} f_e(r, \theta, E_e) = & \frac{1}{c \bar{\epsilon}_e(E_e)} \int_{E_e}^{\infty} dE_{e0} \hat{Q}_e \left[\frac{1}{\bar{\epsilon}_p(E_p)} \int_{E_p}^{\infty} dE_{p0} \right. \\ & \left. \times \frac{J_p(E_{p0})}{r^2} \frac{\exp\left(-\frac{\theta^2}{D_e + D_p}\right)}{\pi(D_e + D_p)} \delta(S - r) \right]. \end{aligned} \quad (2.18)$$

Here S is sum of the distances traveled by proton to the point of interaction with CMRB

and traveled by electron from the point of production to the point r :

$$S = S_p(E_p, E_{p0}) + S_e(E_e, E_{e0}). \quad (2.19)$$

The angular distribution of electrons in Eq. (2.18) is characterized by

$$D_e = A_{e1} - 2\frac{A_{e2}}{r} + \frac{A_{e3}}{r^2}, \quad (2.20)$$

where $A_{ei} = A_{ei}(E_e, E_{e0})$ have the same meaning as in Eq. (2.5), and

$$D_p = \frac{1}{r^2} \int_0^{r_0} \langle \theta_s^2 \rangle r'^2 dr', \quad (2.21)$$

where $r_0 = S_p(E_p, E_{p0})$.

The main channel of production of gamma rays by HE electrons is synchrotron radiation. Applying the modified Eq. (2.130) for the spectrum of synchrotron radiation in chaotic magnetic field to the distribution of electrons given by Eq. (2.18), we find the angular and spatial distributions of gamma ray. Let us describe the procedure as in Eq. (2.15) by

$$Q_s(r, \theta, E_\gamma) = \hat{Q}_s(f_e(r, \theta, E_e)). \quad (2.22)$$

In the general case the distribution function of gamma rays that are characterized by the source function $Q(\mathbf{r}, \mathbf{n}, E)$ and propagate through the absorbing medium with extinction coefficient $k(E)$, is

$$f_\gamma(\mathbf{r}, \mathbf{n}, E) = \frac{1}{c} \int_0^\infty Q(\mathbf{r} - \mathbf{n}\tau, \mathbf{n}, E) e^{-k\tau} d\tau, \quad (2.23)$$

where \mathbf{n} is the direction of movement at the point \mathbf{r} that coincides with the direction of emitting as the propagation of gamma rays is rectilinear. Since emitting electrons have ultrarelativistic energy we assume that the direction of radiation coincide with the electron direction, therefore the distribution function of synchrotron gamma rays for the distribution of electrons given by Eq. (2.18) is

$$f_\gamma(r, \theta, E_\gamma) = \frac{1}{c} \int_0^\infty \hat{Q}_s(f_e(|\mathbf{r} - \mathbf{n}\tau|, \theta_i, E_e)) e^{-k(E_\gamma)\tau} d\tau, \quad (2.24)$$

where θ_i is the angle between \mathbf{n} and $\mathbf{r} - \mathbf{n}\tau$, and θ is the angle between \mathbf{n} and \mathbf{r} . It is convenient to perform the integration over τ using delta-function in Eq. (2.18). For that

we should change the order of integration so the integration over τ becomes internal. Using the features of the delta-function we find

$$\frac{\delta(|\mathbf{r} - \mathbf{n}\tau| - S)}{|\mathbf{r} - \mathbf{n}\tau|^2} = \frac{1}{Sr} \frac{1}{\sqrt{\left(\frac{S}{r}\right)^2 - \sin^2 \theta}} \sum_{i=1}^2 \delta(\tau - \tau_i), \quad (2.25)$$

where $\tau_{1,2} = r(\cos \theta \mp \sqrt{\left(\frac{S}{r}\right)^2 - \sin^2 \theta})$. Since the term corresponding to τ_2 does not contribute to large angles θ_i in exponent (see Eq. (2.18)) we keep only the term corresponding to τ_1 . After performing relevant calculations we obtain:

$$f_\gamma(\mathbf{r}, \theta, E_\gamma) = \hat{Q}_s \left\{ \frac{1}{c^2 \bar{\epsilon}_e(E_e)} \int_{E_e}^\infty dE_{e0} \hat{Q}_e \left[\frac{1}{\bar{\epsilon}_p(E_p)} \right. \right. \\ \left. \left. \times \int_{E_p}^\infty dE_{p0} \tilde{f}_p \eta \left(1 - \frac{S}{r} \right) \eta \left(\frac{S}{r} - \sin \theta \right) \right] \right\}, \quad (2.26)$$

where

$$\tilde{f}_p = \frac{J_p(E_{p0})}{\frac{S}{r} \sqrt{\left(\frac{S}{r}\right)^2 - \sin^2 \theta}} \frac{\exp\left(-\frac{\theta_1^2}{D_e + D'_p}\right)}{\pi r^2 (D_e + D'_p)} e^{-k(E_\gamma) \tau_1}, \quad (2.27)$$

η is Heaviside function. The angle between \mathbf{n} and $\mathbf{r} - \mathbf{n}\tau$ is

$$\theta_1 = \arccos \left(\frac{\sqrt{(S/r)^2 - \sin^2 \theta}}{S/r} \right). \quad (2.28)$$

2.2 The spectral and angular distributions of protons, photons and neutrinos

2.2.1 Protons

Transport of protons substantially depends on the spatial distribution of magnetic fields. The assumption of chaotically oriented magnetic cells is usually used for estimates of the influence of IGMF on cosmic-ray propagation (see, e.g., Ref. [12]). The spectral analysis of the correlation function of the magnetic field fluctuations [38] provides a more appropriate and accurate treatment of the problem. We use this approach for derivation of the mean square deflection angle.

UHE protons propagate large distances in IGMF without considerable deflections.

Indeed, the evaluation of the deflection angle $\delta\theta \simeq \lambda/r_g$ on the correlation length λ is

$$\delta\theta \simeq 9 \times 10^{-3} \left(\frac{\lambda}{1 \text{ Mpc}} \right) \left(\frac{B}{10^{-9} \text{ G}} \right) \left(\frac{10^{20} \text{ eV}}{E} \right) \text{ rad}, \quad (2.29)$$

where $r_g = E/eB$ is the gyroradius of the ultrarelativistic particle. Therefore change of direction of ultrahigh energy protons is small on the scale $\lambda \simeq 1 \text{ Mpc}$. The proton energy can be assumed constant for this scale. Then the proton motion in the magnetic field is described by the equation

$$\dot{\mathbf{v}} = \frac{ec}{E} [\mathbf{v} \times \mathbf{B}(\mathbf{r})]. \quad (2.30)$$

For ultrarelativistic particles $\mathbf{v} = c\mathbf{n}$, where \mathbf{n} is a unit vector. Rewriting the change in velocity over the time Δt in the form $\Delta\mathbf{v} = c\boldsymbol{\theta}$, we find

$$\boldsymbol{\theta} = \int_t^{t+\Delta t} \frac{ec}{E} [\mathbf{n} \times \mathbf{B}(\mathbf{r}(t))] dt. \quad (2.31)$$

Since the deflection angle is small, the trajectory of particle can be considered rectilinear in integration.

Now one should make an assumption about the statistical properties of the magnetic fields. Here we assume that IGMF is a statistically isotropic and homogeneous. While $\langle \boldsymbol{\theta} \rangle = 0$ (since in this case $\langle \mathbf{B} \rangle = 0$), the mean square deflection is

$$\begin{aligned} \langle \theta^2 \rangle &= \left(\frac{ec}{E} \right)^2 \int \langle [\mathbf{n} \times \mathbf{B}_1][\mathbf{n} \times \mathbf{B}_2] \rangle dt_1 dt_2 \\ &= \left(\frac{e}{E} \right)^2 (\delta_{\alpha\beta} - n_\alpha n_\beta) \int \langle B_{1\alpha} B_{2\beta} \rangle dz_1 dz_2, \end{aligned} \quad (2.32)$$

where $\mathbf{B}_{1,2} = \mathbf{B}(\mathbf{r}(t_{1,2}))$. Here we switch to integration over coordinates of particle, directing z -axis along \mathbf{n} .

Eq. (2.32) includes the correlation function of the magnetic field

$$K_{\alpha\beta}(\mathbf{r}_1 - \mathbf{r}_2) \equiv \langle B_\alpha(\mathbf{r}_1) B_\beta(\mathbf{r}_2) \rangle. \quad (2.33)$$

It depends only on the difference $(\mathbf{r}_1 - \mathbf{r}_2)$ because we assume statistical homogeneity of the magnetic field. The mean square of magnetic field is determined as $\langle \mathbf{B}^2 \rangle = K_{\alpha\alpha}(0) = \text{const.}$

To turn to the spectral description, $K_{\alpha\beta}$ should be written as a Fourier integral:

$$K_{\alpha\beta}(\mathbf{r}_1 - \mathbf{r}_2) = \int \tilde{K}_{\alpha\beta}(\mathbf{k}) e^{i\mathbf{k}(\mathbf{r}_1 - \mathbf{r}_2)} \frac{d^3k}{(2\pi)^3}. \quad (2.34)$$

Since $\text{div} \mathbf{B} = 0$, then $K_{\alpha\beta}$ should satisfy the conditions

$$\partial K_{\alpha\beta} / \partial x_{1\alpha} = 0, \quad \partial K_{\alpha\beta} / \partial x_{2\beta} = 0. \quad (2.35)$$

For function $\tilde{K}_{\alpha\beta}$ these conditions take on form $\tilde{K}_{\alpha\beta} k_\alpha = 0$, $\tilde{K}_{\alpha\beta} k_\beta = 0$. Therefore, if there is no preferential direction in space, $\tilde{K}_{\alpha\beta}$ has the following structure:

$$\tilde{K}_{\alpha\beta}(\mathbf{k}) = \frac{1}{2} \left(\delta_{\alpha\beta} - \frac{k_\alpha k_\beta}{\mathbf{k}^2} \right) \Phi(\mathbf{k}^2) \langle \mathbf{B}^2 \rangle. \quad (2.36)$$

Here constant factor $\langle \mathbf{B}^2 \rangle$ is introduced such that $\Phi(\mathbf{k}^2)$ meets the normalization condition:

$$\int \Phi(\mathbf{k}^2) \frac{d^3k}{(2\pi)^3} = \frac{1}{2\pi^2} \int_0^\infty \Phi(\mathbf{k}^2) k^2 dk = 1. \quad (2.37)$$

It is convenient to change variables $z_1 = z + \zeta/2$, $z_2 = z - \zeta/2$ in the integral in Eq. (2.32). Assuming that the traveled distance Δz is much greater than a characteristic scale on which the correlation function tends to zero, one can extend the limits of integration over ζ to infinity. Meanwhile, the traveled distance should be smaller than the distance on which the proton loses its energy appreciably. The integrand depends only on ζ , therefore the integration over dz gives the length of integration interval Δz . The mean square deflection angle is proportional to the traveled distance, so the mean square deflection per unit length is

$$\langle \theta_s^2 \rangle = \left(\frac{e}{E} \right)^2 (\delta_{\alpha\beta} - n_\alpha n_\beta) \int_{-\infty}^{\infty} K_{\alpha\beta}(0, 0, \zeta) d\zeta. \quad (2.38)$$

Integration of $K_{\alpha\beta}$ written in the form of Eq. (2.34) over $d\zeta$ gives $2\pi\delta(k_z)$ that allows us to calculate the integral over dk_z . Then, the integral remains over the components of \mathbf{k} perpendicular to z -axis. Using Eq. (2.36), we obtain

$$\langle \theta_s^2 \rangle = \frac{1}{2} \left(\frac{e}{E} \right)^2 \langle \mathbf{B}^2 \rangle \int \frac{d^2 k_\perp}{(2\pi)^2} \Phi(k_\perp^2). \quad (2.39)$$

The derived result can be written in the form

$$\langle \theta_s^2 \rangle = \frac{\pi}{2} \left(\frac{e}{E} \right)^2 \langle \mathbf{B}^2 \rangle \Lambda, \quad (2.40)$$

where

$$\Lambda = \int \frac{d^3 k}{(2\pi)^3} \frac{1}{k} \Phi(k^2) = \frac{1}{2\pi^2} \int_0^\infty \Phi(\mathbf{k}^2) k dk. \quad (2.41)$$

Taking into account Eq. (2.37), the factor Λ can be treated as the mean value of k^{-1} , $\Lambda = \langle k^{-1} \rangle$.

The calculation of $\langle \theta_s^2 \rangle$ requires the spectral energy distribution of magnetic field. To obtain final form of $\langle \theta_s^2 \rangle$ we assume a power-law spectrum

$$\Phi(k^2) k^2 \sim \begin{cases} \left(\frac{k_0}{k} \right)^\alpha, & k > k_0 \\ \left(\frac{k}{k_0} \right)^\beta, & k < k_0 \end{cases} \quad (2.42)$$

where k_0 is an absolute value of the wave vector corresponding to the maximal scale of correlation λ : $k_0 = 2\pi/\lambda$. It gives

$$\langle \theta_s^2 \rangle = \frac{(\alpha - 1)(\beta + 1)}{4\alpha\beta} \left(\frac{e}{E} \right)^2 \langle \mathbf{B}^2 \rangle \lambda. \quad (2.43)$$

Taking into account the turbulent character of IGMF that has $\langle \mathbf{B} \rangle = 0$, we take $\alpha = 5/3$ which corresponds to the Kolmogorov turbulence. The choice of the parameter β is, to a certain extent, arbitrary. Here we assume $\beta = 1$ which leads to a simple expression for the mean square deflection angle per unit length:

$$\langle \theta_s^2 \rangle = \frac{\lambda}{5} \left(\frac{e}{E} \right)^2 \langle \mathbf{B}^2 \rangle. \quad (2.44)$$

Because of uncertainties related to the spectrum of IGMF, the numerical factor in Eq. (2.44) is somewhat different from the coefficients used in other works (see, e.g., Ref. [12]).

Significant uncertainty in calculations of $\langle \theta_s^2 \rangle$ is related to the absolute value of the correlation length λ . It is expected to be between 100 kpc and 1 Mpc, i.e. comparable to the characteristic distances between galaxies. In the subsequent calculations we normalize the correlation length to $\lambda = 1$ Mpc, but the presented results can be easily recalculated for any λ .

Since the propagation of protons in IGMF can be treated as a set of large number of small chaotic deflections, the problem can be reduced to the diffusion in angle. The

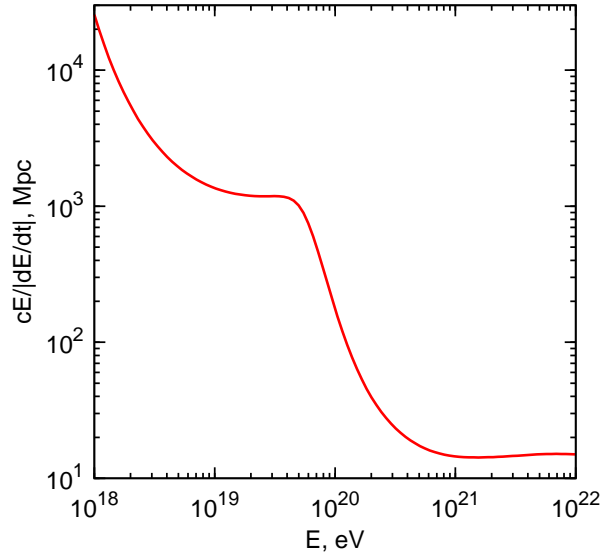


Figure 2.1: The mean free path of protons in the intergalactic medium due to interactions with photons of CMBR.

diffusion coefficient $D(r, E_0)$ given by Eq. (2.14)) contains information about the energy loss and influence of IGMF on propagation, and gives angular distribution of protons at the given point. Since there is a unique correspondence between the energy and r (see Eq. (2.9)) we can rewrite Eq.(2.14) in terms of energy and energy losses per unit length. Substituting Eq.(2.44) into Eq. (2.14), we obtain

$$D(E, E_0) = \frac{\eta}{r^2} \int_E^{E_0} \frac{1}{E'^2} \left(\int_{E'}^{E_0} \frac{dE''}{\bar{\epsilon}(E'')} \right)^2 \frac{dE'}{\bar{\epsilon}(E')}, \quad (2.45)$$

where

$$r = \int_E^{E_0} \frac{dE'}{\bar{\epsilon}(E')}, \quad \eta = \frac{e^2 \lambda}{5} \langle \mathbf{B}^2 \rangle. \quad (2.46)$$

The function $E/\bar{\epsilon}(E)$ based on results of Ref. [31] and implying the mean free path of protons in the intergalactic medium due to the Bethe-Heitler pair-production and photomeson processes at interactions with CMBR, is shown in Fig. 2.1.

Note that for many scenarios described by Eq. (2.1) the same process is responsible for both the angular scattering and the energy losses. But in the case of propagation of protons in the intergalactic medium we deal with two different processes: while the interactions with CMBR lead to energy losses, the angular deflections are caused by multiple scattering on magnetic inhomogeneities.

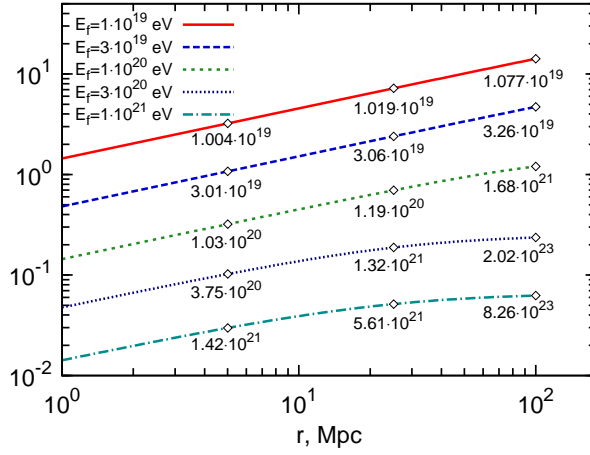


Figure 2.2: The mean deflection angle of protons for the fixed *observed* energy E_f over the distance r . The numbers at the curves indicate the energies which proton had at the distance r from the observer.

The influence of energy losses on the angular distribution of protons can be traced in Fig. 2.2, where mean deflection angle of protons with observed energies E_f is shown as function of traveled distance r . As it is seen from Fig. 2.1, protons with energy smaller than $E = 6 \times 10^{19}$ eV do not suffer noticeable energy losses over the distances ~ 100 Mpc. In this case the diffusion in angular space can be treated as a homogeneous random walk that brings us to the dependence of the mean deflection angle on the travel distance $\propto r^{1/2}$. For protons with initial energy higher than the threshold of photomeson production, the energy of protons gradually decreases which leads to deviation from this simple dependence. In particular, for the given *observed* (final) energy E_f , this effect implies higher original energies, and consequently smaller deflection angles at the initial parts of propagation. This results in a weaker increase of the mean deflection angle with the traveled distance in comparison with loss-free case. This effect is clearly seen from analytical expressions, which is possible to obtain in the case of constant energy loss rate $\left| \frac{dE}{dz} \right| \frac{1}{E} = b = \text{const}$:

$$\langle \theta^2 \rangle \sim \frac{r}{E_f^2} \left(\frac{\zeta^2 - 2\zeta + 2(1 - e^{-\zeta})}{\zeta^3} \right) \Big|_{\zeta=2br}. \quad (2.47)$$

Expanding this expression into series in terms of powers of r we obtain:

$$\langle \theta^2 \rangle \sim \frac{1}{E_f^2} \left(\frac{r}{3} - \frac{br^2}{6} + \dots \right). \quad (2.48)$$

The first term does not depend on the value of b and thereby describes the loss-free

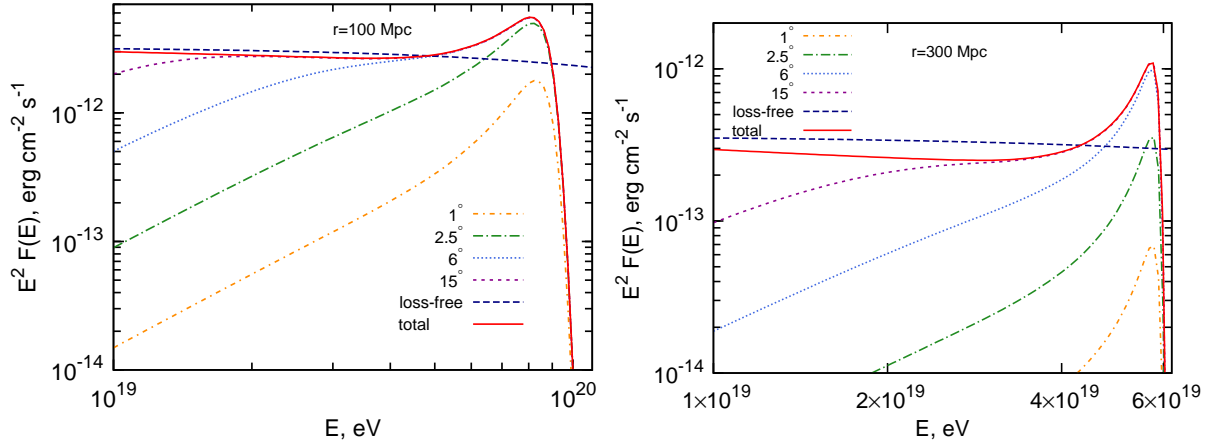


Figure 2.3: Energy flux distribution of protons observed within different angles for the source at the distance $r = 100$ Mpc (left panel) and $r = 300$ Mpc (right panel). The initial spectrum of protons is assumed power-law with an exponential cutoff at $E_0 = 3 \times 10^{20}$ eV, the IGMF is 1 nG.

propagation. The next term takes into account the energy losses and makes the dependence on the distance r weaker. While Eq. (2.47) approximately describes the behavior of mean deflection angle for the final energy $E_f \geq 10^{21}$ eV, the first term of Eq. (2.48) describes the case of $E_f \leq 6 \times 10^{19}$ eV. In Fig. 2.2 the mean deflection angle of protons is given for IGMF $B = 1$ nG. Since the dependence of the average deflection angle on the magnetic field is linear, it is easy to produce plots for other magnetic fields.

In order to indicate the evolution of the energy of protons during their propagation through the 2.7 K CMBR, in Fig. 2.2 we indicate at the corresponding curves, calculated for the fixed observed (final) energies of protons, the energies which protons had at different distances from the observer. For the fixed observed energies exceeding the threshold of photomeson production, the calculated initial energies grow dramatically with the increase of the distance, especially for ≥ 100 Mpc. Therefore any deficit of protons of such high energies in the initial spectrum would result in the cutoff in observed spectrum at the corresponding energies.

The energy distributions of protons at distances 100 Mpc and 300 Mpc are shown in Fig. 2.3 for the initial differential energy spectrum $J_p(E) = J_0 E^{-2} \exp(-E/E_0)$. The total luminosity of the source in CRs with energy above 10^9 eV is taken $L = 10^{44}$ erg/s. The upper dashed lines correspond to the case when protons propagate in empty space; flux is determined by the geometrical factor $1/r^2$. Solid line presents the case when the deflections in the magnetic field are ignored. Comparison of these two curves reveals two features: a bump and a sagging at lower energies. Both features become more prominent with increasing of the distance. The bump preceding the cutoff appears due to strong

growth of energy losses at the threshold of photomeson production (see Fig. 2.1) that makes particles to be accumulated in this energy region; the sagging is a consequence of the energy losses due to the electron-positron pair production (see, e.g., Ref. [32]).

The approximation of continuous energy losses takes into consideration the mean energy losses. In general it provides an acceptable accuracy but some features connected with stochastic properties of interactions should be taken into account for precise description of the spectrum in the cutoff region. The fluctuations in the energy losses do have an impact on the form of the bump and the cutoff in the observed spectrum of protons. It results, in particular, in a smoother cutoff and a broader and lower-amplitude bump [27] compared to the results calculated within the continuous energy losses approximation.

The impact of the magnetic field leads to strong dependence of the energy distribution on the solid angle within which the particles are detected. As it is seen in Fig. 2.3, the flux of protons at highest energies is concentrated along the direction to the source; the protons of lower energies are scattered over large angles.

2.2.2 Electrons

The secondary gamma-rays and neutrinos are tracers of propagation of protons in the intergalactic medium. The first generation gamma-rays from photomeson processes are produced at extremely high energies $E \geq 10^{19}$ eV. They are effectively absorbed due to interactions with the photons of CMBR and the Cosmic Radio Background (CRB) over distance ~ 1 Mpc. Because of the threshold effects, at energies below 10^{14} eV the efficiency of interactions with CMBR dramatically drops, but gamma-rays continue to interact with the infrared and optical photons of the Extragalactic Background Light (EBL). At these energies the mean free path of gamma-rays increases sharply achieving, ~ 100 Mpc at $E_\gamma \sim 10$ TeV, and ~ 1 Gpc at $E \leq 200$ GeV (see, e.g., Ref. [65]). Thus, as long as we are interested in gamma-rays from the sources of highest energy cosmic rays, the energy of gamma-rays should not significantly exceed 1 TeV. In this energy band gamma-rays are produced through the electromagnetic cascade initiated by the products of decays of short-lived mesons from the photomeson interactions and, partly, by electrons from the Bethe-Heitler pair-production process. For the development of an effective cascade the magnetic field should be smaller than 10^{-10} G. Even so, the observer can see the cascade gamma-rays in the direction of the source only in the case of extremely small IGMF, $B \leq 10^{-15}$ G. A collimated beam of gamma-rays of GeV–TeV energies is expected in the case of magnetized intergalactic medium with $B \geq 10^{-9}$ G. These gamma-rays are produced through the synchrotron radiation of $E \geq 10^{19}$ eV

electrons.

Due to very large Lorentz factor of particles, we can assume that secondary products from all interactions under consideration propagate strictly in the direction of the parent particle. Therefore observed angular distribution of gamma rays depends on the influence of IGMF on electrons that produce these gamma rays. To observe the UHECR source in gamma rays it is necessary that producing electrons are only slightly deflected in IGMF.

The almost rectilinear part of the path of electrons is much smaller than distances traveled by protons and is comparable to the typical correlation length, $\lambda \simeq 1$ Mpc. So the scattering of electrons takes place in almost homogeneous magnetic field. But since direction of magnetic field have a random character the scattering occurs in random directions. In case of electrons one can apply the formalism of the multiple scattering to the random single scattering. Indeed, as have been noted the distribution function should be smooth function of angle to write the elastic collision integral in the Fokker-Planck approximation. If all particles are scattered, as in the case of electrons, the distribution function does not include a part with sharp angular distribution corresponding to non-scattered particles.

To obtain the mean square deflection angle per unit length we use expression for deflection angle of ultrarelativistic electron traveled the path on which its energy has changed from the initial energy E' to the final energy E :

$$\theta = \int_E^{E'} \frac{1}{\bar{\epsilon}_e r_g} dE'', \quad (2.49)$$

where $\bar{\epsilon}_e$ is rate of energy losses due to synchrotron radiation and r_g is gyroradius. Taking into account random field orientations we find

$$\langle \theta_s^2 \rangle = \frac{3}{2} \frac{(mc^2)^4}{e^2 E} \left(\frac{1}{E} - \frac{1}{E'} \right) \left(\frac{1}{E} + \frac{2}{3} \frac{1}{E'} \right). \quad (2.50)$$

After substitution this equation into Eq. (2.5) we find the coefficients A_{ei} of the diffusion coefficient D_e in simple analytical forms:

$$A_1 = \frac{5\alpha\beta}{180} \frac{1}{E^4} (7\xi^2 + 14\xi + 9)(1 - \xi)^2, \quad (2.51)$$

$$A_2 = \frac{\alpha\beta^2}{180} \frac{1}{E^5} (19\xi^2 + 22\xi + 9)(1 - \xi)^3, \quad (2.52)$$

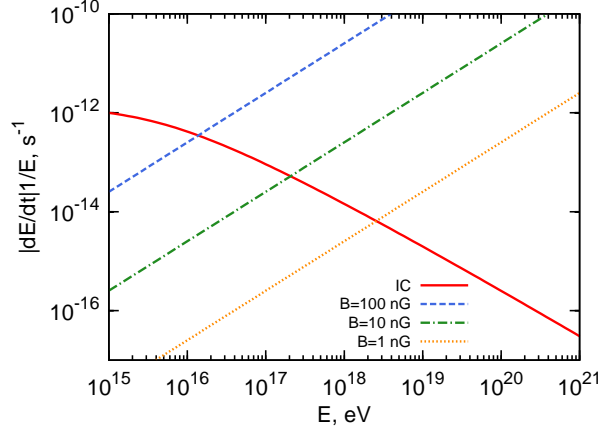


Figure 2.4: Energy loss rates of electrons due to inverse Compton scattering on CMBR photons (solid line) and synchrotron radiation in random magnetic field for $B = 1$ nG, 10 nG, and 100 nG. For electrons of energy $E \gtrsim 10^{19}$ eV the inverse Compton scattering on the radiowaves of CRB becomes comparable or even can exceed the contribution of the Compton scattering on CMBR, however for IGMF $B \gtrsim 1$ nG the synchrotron radiation remains the main cooling channel.

$$A_3 = \frac{\alpha\beta^3}{180} \frac{1}{E^6} (12\xi^2 + 10\xi + 3)(1 - \xi)^4, \quad (2.53)$$

where

$$\alpha = \frac{6}{5} \frac{(mc^2)^4}{e^2}, \quad \beta = \frac{9}{4} \frac{(mc^2)^4}{e^4 B^2}, \quad \xi = \frac{E}{E'}. \quad (2.54)$$

Eq. (2.49) can be written in the form

$$\theta \approx 0.008^\circ \frac{(1 - \xi^2)}{B_{nG} E_{20}^2}, \quad (2.55)$$

where B_{nG} is the magnetic field in units of nanoGauss (nG), E_{20} is final energy in units of 10^{20} eV, $\xi = E/E'$. Here the random orientations of the field are taken into account. This expression allows us to estimate the threshold of isotropization. Indeed, if the electron loses considerable part of its energy, then $\xi \ll 1$ and deflection angle mostly depends on the final energy. The deflection angle becomes quite large (~ 1 radian) in the magnetic of field 1 nG when final energy is $E \approx 2 \times 10^{18}$ eV. For greater magnetic field the threshold of isotropization is shifted to the range of lower energies. It should be noted that for magnetic fields 1 – 100 nG this threshold appears in the energy region where the energy losses due to synchrotron radiation dominate over the inverse Compton scattering (see Fig. 2.4). It means that inverse Compton scattering can be neglected for

electrons under consideration.

Let us estimate the energy of gamma rays produced by electrons with energy exceeding the threshold of isotropization. Using modified Eq. (2.130) for energy distribution of synchrotron radiation in chaotic magnetic fields, we find the energies of electrons that produce synchrotron gamma rays with energy E_γ :

$$E_e = 1.23 \times 10^{14} \sqrt{\frac{E_\gamma}{xB_{nG}}}. \quad (2.56)$$

Here E_e and E_γ are given in units of eV, x is the dimensionless argument of distribution function Eq. (2.134). The latter has a maximum at $x \approx 0.2291$ and exponentially decreases for large x (see Eq. (2.136)). To make sure that observed gamma rays are produced by electrons with energies greater threshold of isotropization we should consider gamma rays with energies $E_\gamma \gtrsim 10^9$ eV. Indeed, electrons with energies corresponding to $x \gtrsim 10$ in the Eq. (2.56) give exponentially small contribution into radiation of gamma rays of the given energy. Therefore, assuming $x = 10$, we find that the contribution of electrons with energies below threshold of isotropization $E_e \lesssim 10^{18}$ eV into radiation of $E_\gamma = 10^9$ eV gamma rays is insignificant. According to Eq. (2.55) the product BE^2 is constant for the isotropization threshold. Since the same combination enters in Eq. (2.56) the minimal energy of gamma rays produced by the electrons under consideration does not depend on the magnetic field.

At interactions of protons with the intergalactic radiation fields the ultrahigh energy electrons are produced via two channels: pair production and photomeson production processes. In the pair production process only a small ($\leq 2m_e/m_p$) fraction of proton energy is converted to the secondary electrons. For the magnetic field of order of nG or larger, the energies of these electrons appear below the threshold of isotropization, thus they do not contribute to the gamma-ray emission emitted towards the observer. The photomeson processes lead to several non-stable secondary particles, such as π , η , K mesons, which decay into high energy gamma rays, neutrinos and electrons. The electrons from the decays of these mesons are produced with energies [31] exceeding the isotropization threshold.

In addition, a significant fraction of electrons is created at interactions of the first generation ("photomeson") gamma-rays with photons of CMBR and CRB. For the model of CRB suggested by [66], the mean free path of gamma-rays of $E \geq 10^{19}$ eV is determined by the interactions with MHz radiowaves; it is of order of several Mpc. Here we neglect by the interaction length assuming that gamma rays interact with CRB immediately after their creation. In this case the particle get additional deflection since it is treated as electron all along. It results in broader angular distribution of observed

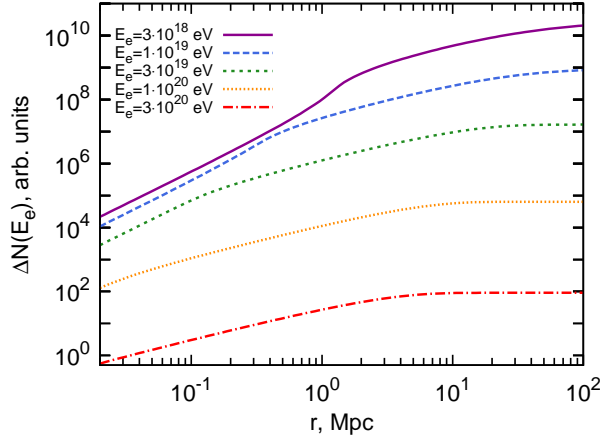


Figure 2.5: Number of electrons of energy E_e located inside a sphere of the radius r .

gamma ray in comparison with exact consideration. The interaction of gamma rays with CRB photons of energy ϵ_R occurs in the regime $\epsilon_R E_\gamma / m_e^2 c^4 \gg 1$. It means that the most of the energy is converted to one of the two electrons. The energy of gamma rays is higher than the energy of electrons produced in the decays of mesons (see, e.g., Ref. [31]). Therefore electrons created by pair production process are more energetic than electrons generated in the decays of nonstable products of photomeson processes. Consequently, the pair-produced electrons result in higher flux of synchrotron radiation than the direct ones from the meson decays.

2.2.3 Gamma rays and neutrinos

The apparent angular size of the synchrotron gamma-ray source depends on the linear size of the emitter itself and the deflection angles of the parent electrons. Both are defined by spatial and angular distributions of electrons, respectively. In the case of spherically symmetric source and small deflection angles of electrons θ_{def} , the source located at the distance r with the gamma-ray emission region of radius d , has an angular size $\vartheta_{obs} \sim 2 \frac{d}{r} \theta_{def}$. The case of isotropically emitted gamma-ray source corresponds to $\theta_{def} \sim 1$. The linear size of the gamma-ray emitter can be evaluated from Fig. 2.5, where is shown the number of electrons of energy E_e located inside the sphere of radius r . The saturation that takes place at large distances shows the absence of electrons in this region. One can see from Fig. 2.5 that the size of the sphere, where the electrons are located, decreases while the energy increases. This is explained by the fact that protons producing electrons of such high energies disappear due to energy losses. For energies below $E_e = 10^{19}$ eV the electrons are not located in a definite region. The electrons with energy below the thermalization threshold form an extended halo. These electrons have

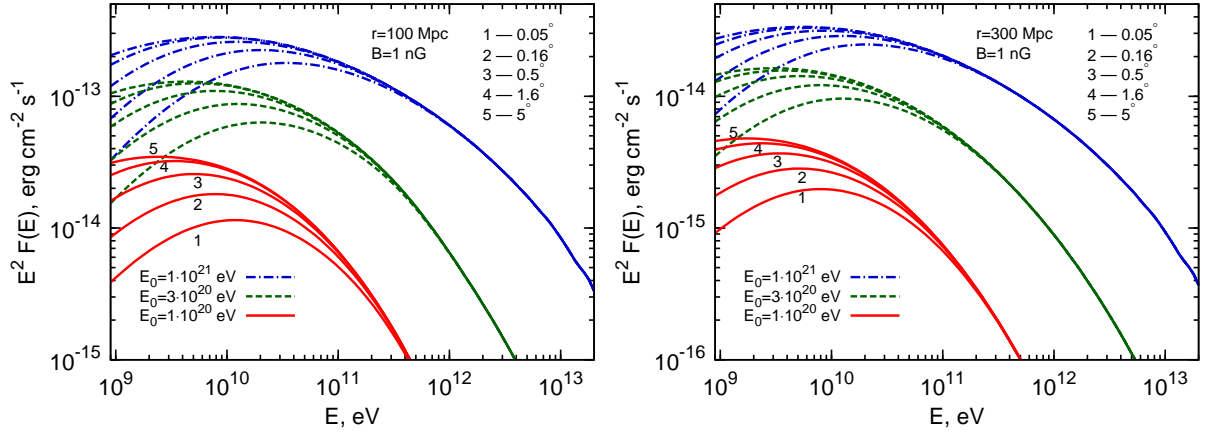


Figure 2.6: Flux distributions of gamma rays observed within different angles in the direction of the source located at the distance $r = 100$ Mpc (left panel) and $r = 300$ Mpc (right panel). Calculations correspond to the IGMF $B = 1$ nG and initial power-law distributions of protons with spectral index $\alpha = 2$ and exponential cutoffs at $E_0 = 10^{20}$ eV; 3×10^{20} eV, and 10^{21} eV. The total power of injection of protons into IGM is 10^{44} erg/s.

energies at which the inverse Compton scattering losses dominates over the energy losses due to the synchrotron radiation. They initiate electromagnetic cascades in the CMBR and EBL photon fields that eventually results in a very extended GeV-TeV gamma ray emission.

The spectral energy distributions (SED) of gamma-rays, $E^2 F(E)$, received within different angles are presented in Fig. 2.6. The fluxes are calculated for the same initial proton energy distribution used in Fig. 2.3. Three series of curves for each of two distances (left and right panels) correspond to different cutoff energies in the initial proton spectrum. One can see that the cutoff energy has significant impact on the flux of gamma rays; it increases the flux, shifts the maximum of SED towards higher energies, and makes narrower the angular distributions. These features have a simple explanation. The increase of the cutoff energy provides more secondary electrons and extends the spectrum of electrons to more energetic region. The latter leads to smaller deflections. It is interesting to note that although the angular distribution of gamma rays is composed of deflections of both protons and electrons, their angular distribution is more narrow compared to the angular distribution of protons (see, Fig. 2.3). This is explained by the fact that the main portion of gamma rays is produced in regions close to the source by the highest energy protons which did not suffer significant energy losses (see, Fig. 2.5), while the multiple scattering in IGMF contributes to the formation of the angular distribution of protons over the entire path from the source to the observer.

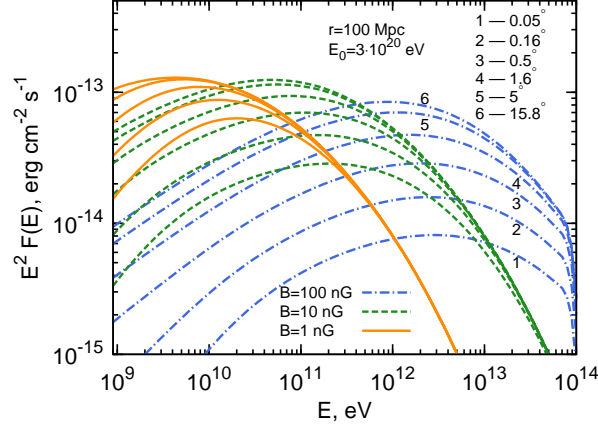


Figure 2.7: Flux distributions of gamma rays observed within different angles in the direction of the cosmic ray source at the distance $r = 100$ Mpc. The calculations are performed for three different IGMF $B = 1$ nG, 10 nG, 100 nG, assuming an initial power-law distribution of protons with spectral index $\alpha = 2$ an exponential cutoff at $E_0 = 3 \times 10^{20}$ eV. The total power of injection of protons into IGM is 10^{44} erg/s. The intergalactic absorption of gamma-rays due to interactions with EBL is not taken into account.

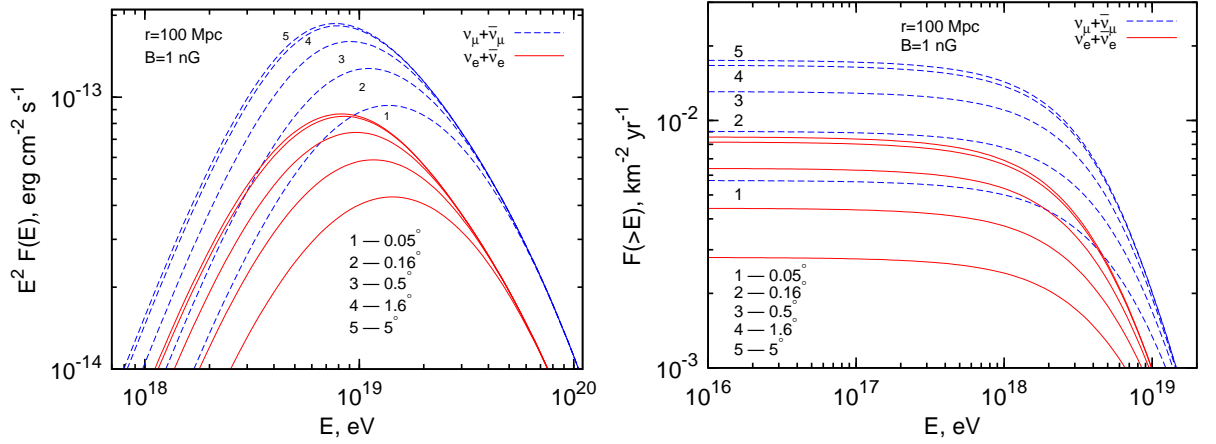


Figure 2.8: The fluxes of neutrinos observed within different angles in the direction of the cosmic ray proton source located at the distance $r = 100$ Mpc. The calculations are performed for the initial power-law distribution of protons with spectral index $\alpha = 2$ and the exponential cutoff at $E_0 = 3 \times 10^{20}$ eV. The IGMF $B = 1$ nG, and the total power of injection of protons into IGM is 10^{44} erg/s. Left panel is spectral energy distributions, right panel is integral fluxes.

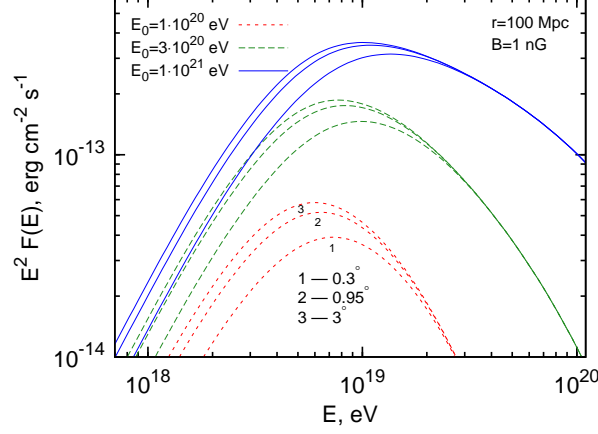


Figure 2.9: The spectral energy distributions of muon neutrinos observed within different angles towards the source of cosmic ray protons located at $r = 100$ Mpc. The calculations are performed for initial power-law distribution of protons with $\alpha = 2$ and three different values of the exponential cutoff: $E_0 = 10^{20}$ eV, 3×10^{20} eV, and 10^{21} eV.

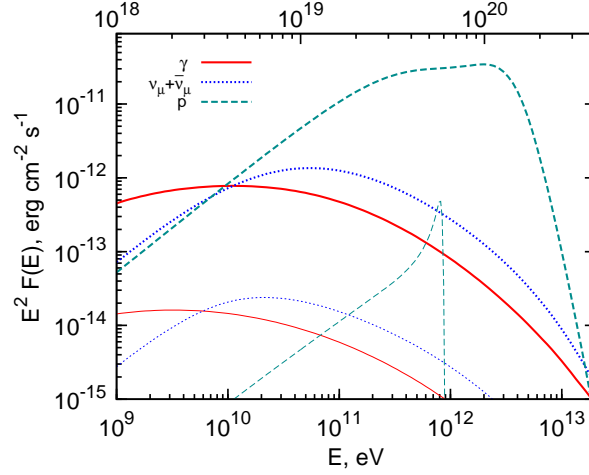


Figure 2.10: The spectral energy distributions of gamma rays, muon neutrinos and protons observed within the polar angle 3° from two identical source located at $r = 30$ Mpc (thick lines) and $r = 300$ Mpc (thin lines). The upper energy scale is for protons and neutrinos, the lower energy scale is for gamma-rays. The calculations are performed for the initial power-law distribution of protons with spectral index $\alpha = 2$, the exponential cutoff $E_0 = 3 \times 10^{20}$ eV, and the total power of injection into IGM 10^{44} erg/s. The IGMF is 1 nG.

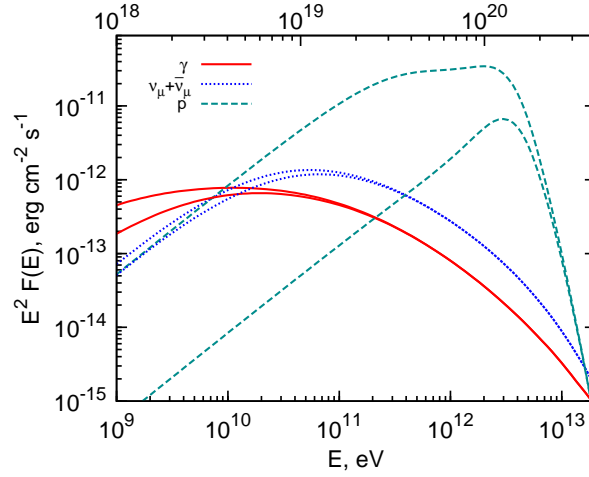


Figure 2.11: The spectral energy distribution of gamma rays, muon neutrinos and protons observed within polar angles 0.3° and 3° towards a source located at $r = 30$ Mpc. The parameters for the IGMF and the proton spectrum are the same as in Fig. 2.10.

Since the angular size of the gamma-ray source is determined by the geometrical factor d/r , the distribution of gamma-rays from a source at the distance $r = 300$ Mpc is narrower than from an identical source located at the distance $r = 100$ Mpc. It is remarkable that at very high energies the source becomes point-like. In particular, at energies above $E_\gamma \approx 5 \times 10^{11}$ eV, the observer will see the gamma-ray source located at the distance of 100 Mpc within an angle smaller than $\theta_{obs} = 0.1^\circ$.

Fig. 2.7 shows the impact of the IGMF strength on the flux distribution of gamma rays. The increase of the magnetic field leads to the shift of the maximum of SED to higher energies. In accordance with Eq. (2.56), the shift of the synchrotron peak is proportional to the strength of the magnetic field since the energy distribution of electrons does not depend on the magnetic field. Finally note that the increase of the magnetic field implies strong deflections which leads to the reduction of the flux and widening of the angular distribution of gamma-rays.

For the sources located beyond 100 Mpc, TeV gamma-rays interact effectively with optical and infrared photons of the Extragalactic Background Light (EBL). The energy-dependent absorption of gamma-rays is characterized by the optical depth $\tau_{\gamma\gamma}$ which depends on the EBL flux and is proportional to the distance to the source. Unfortunately the EBL flux contains quite large uncertainties, especially at the mid and far IR wavelengths which are most relevant to the gamma-ray energy band and the source distances discussed here. The impact of these uncertainties on the intergalactic absorption of gamma-rays is discussed in Ref. [65]. Even for the minimum EBL flux at infrared

wavelengths, the absorption of TeV gamma-rays from sources beyond 100 Mpc can be significant; at multi-TeV energies the optical depth $\tau_{\gamma\gamma}$ exceed 1. Therefore the curves in Figs 2.6, 2.7 and 2.8 should be corrected by multiplying the unabsorbed fluxes to the factor $\exp(-\tau_{\gamma\gamma})$.

The decay of nonstable products of photomeson processes leads to the appearance of extremely high energy electrons (positrons) and neutrinos (antineutrinos). Since the magnetic field does not have an impact on neutrinos, the angular distribution of neutrinos is determined only by the deflection of protons. This leads to more narrow angular distributions of neutrinos compared not only to the distributions of protons (for the same reason described above for gamma-rays) but also compared to the distribution of gamma-rays (because the gamma-ray distribution is additionally broadened due to deflections of electrons). The left panel of Fig. 2.8 shows SED of neutrinos and antineutrinos received within different angles. The right panel of the figure presents the integral fluxes of neutrinos. The impact of the cutoff energy in the initial proton spectrum on the neutrino flux is demonstrated in Fig. 2.9.

For comparison, the spectral energy distributions of protons, gamma rays and muon neutrinos are shown together in Fig. 2.10 and Fig. 2.11 for two distance to the source - 30 Mpc and 300 Mpc.

2.3 An impulsive source: arrival time distributions

Let assume that at the moment $t = 0$ an impulsive spherically-symmetric source injects protons into the intergalactic medium. The multiple scattering of protons in the chaotic magnetic field results in the deviation of the motion of particles from the rectilinear propagation, therefore they arrive to the observer with significant time delays. The arrival time of the proton moving with a speed v_p over the path S is

$$t = \frac{S}{v_p} = \frac{S}{c} + 4.5 \times 10^{-4} \left(\frac{S_{\text{Mpc}}}{100} \right) \left(\frac{10^{18}}{E_{\text{eV}}} \right)^2 \text{ s}. \quad (2.57)$$

For ultrarelativistic protons the second term is negligible, therefore in calculations we adopt $v_p = c$. In this chapter we will study the distribution of the arrival-time delays $\tau = t - r/c$ ignoring the energy losses of particles.

Let denote by $P(\tau, \zeta, r) d\zeta d\tau$ the probability that the proton with arrival direction in the interval $(\zeta, \zeta + d\zeta)$ is detected at the distance r from the source in the time interval $(\tau, \tau + d\tau)$. Here $\zeta = \theta^2$, where θ is the angle between the proton direction at the point \mathbf{r} and the vector \mathbf{r} . It is assumed that P satisfies to the condition of normalization

given by Eq. (2.129). The equation for the function P for a pulse of radiation in the small-angle approximation is obtained in Ref. [67]. In Appendix 2.5 we derive the exact relation between P and the standard distribution function f , and obtain P in a quite different (simpler) way than in Ref. [67]. Namely, our treatment of the problem is based on the solution of equations written for the standard distribution function.

Following to Ref. [67] we introduce the function G which is determined from the equation

$$P(\tau, \zeta, r) = \frac{c}{r^3 \langle \theta_s^2 \rangle^2} G(x, y), \quad (2.58)$$

where the dimensionless parameters x and y are

$$x = \frac{\zeta}{r \langle \theta_s^2 \rangle} = \frac{\theta^2}{r \langle \theta_s^2 \rangle}, \quad y = \frac{c\tau}{r^2 \langle \theta_s^2 \rangle}. \quad (2.59)$$

Function G can be presented in the form of one-dimensional integral

$$G(x, y) = \int_{-\infty}^{\infty} \frac{ds}{2\pi} \tilde{G}(x, s) e^{isy}. \quad (2.60)$$

Here

$$\tilde{G}(x, s) = \frac{z}{j_1(z)} \exp\left(-x \frac{z j_0(z)}{j_1(z)}\right), \quad (2.61)$$

where $z = \sqrt{s/(2i)}$, j_0 and j_1 are spherical Bessel functions:

$$j_0(z) = \frac{\sin z}{z}, \quad j_1(z) = \frac{\sin z}{z^2} - \frac{\cos z}{z}. \quad (2.62)$$

The angular distribution of particles changes with time. It can be shown, by using Eqs. (2.60) and (2.61), that

$$\langle \theta^2 \rangle(\tau) = 4c\tau/r, \quad (2.63)$$

where

$$\langle \theta^2 \rangle(\tau) = \int_0^{\infty} \theta^2 G(x, y) dx \Big/ \int_0^{\infty} G(x, y) dx \quad (2.64)$$

is the mean square deflection angle at the moment τ . Quite remarkably no model parameters enter in (2.63) in an explicit form. Thus, the measurements of θ^2 at different time periods allow an estimate of the distance to the source. This is a nice feature, because it could be the only channel of information about the distance to the source, if the latter is not active anymore.

From Eqs. (2.60) and (2.61) follows that $G(x, y) = 0$ at $y < 0$. We should note also

the useful relation

$$\tilde{G}(x, s) = \int_{-\infty}^{\infty} dy G(x, y) e^{-isy}, \quad (2.65)$$

which allows us to obtain the moments of the function G :

$$m_n \equiv \int_{-\infty}^{\infty} dy y^n G(x, y) = i^n \frac{\partial^n}{\partial s^n} \tilde{G}(x, s) \Big|_{s=0}. \quad (2.66)$$

Let's write down the first three moments:

$$m_0 = 3 e^{-3x}, \quad (2.67)$$

$$m_1 = \frac{3}{20} (1 + 2x) e^{-3x}, \quad (2.68)$$

$$m_2 = \frac{3}{2800} (9 + 36x + 28x^2) e^{-3x}. \quad (2.69)$$

Correspondingly the mean values for $\langle y \rangle$ and $\langle y^2 \rangle$ are

$$\langle y \rangle = \frac{m_1}{m_0} = \frac{1}{20} (1 + 2x), \quad (2.70)$$

$$\langle y^2 \rangle = \frac{m_2}{m_0} = \frac{1}{100} \left(\frac{9}{28} + \frac{9}{7} x + x^2 \right). \quad (2.71)$$

For the dispersion of distribution Δ and the ratio $\frac{\Delta}{\langle y \rangle^2}$ we have

$$\Delta \equiv \langle y^2 \rangle - \langle y \rangle^2 = \frac{1}{1400} (1 + 4x), \quad (2.72)$$

and

$$\frac{\Delta}{\langle y \rangle^2} = \frac{2}{7} \frac{1 + 4x}{(1 + 2x)^2} \leq \frac{2}{7}. \quad (2.73)$$

This implies that we deal with a rather narrow distribution. Rewriting Eq. (2.70) in the form

$$\frac{c\langle \tau \rangle}{r^2 \langle \theta_s^2 \rangle} = \frac{1}{20} \left(1 + \frac{2\theta^2}{r \langle \theta_s^2 \rangle} \right) \quad (2.74)$$

one can see that the measurement of $\langle \tau \rangle$ for the particles with different values of θ allows to estimate $\langle \theta_s^2 \rangle$.

Below we discuss two special cases of practical interest.

A. Detection of protons with arbitrary arrival angles. This is the case discussed in

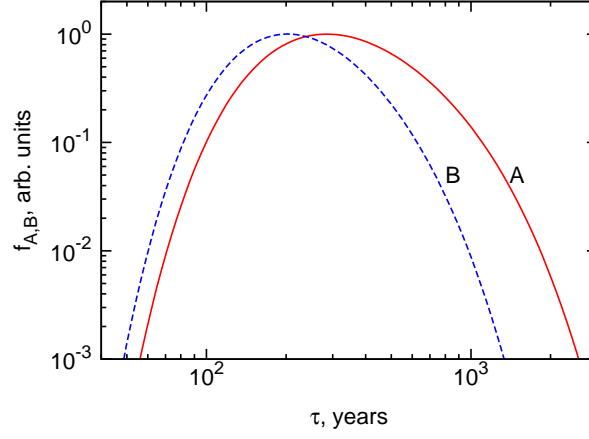


Figure 2.12: The arrival time distributions for the cases **A** (solid line) and **B** (dashed line) discussed in the text. The distance to the source is $r = 10$ Mpc, the energy of protons $E = 10^{20}$ eV, and the strength of the magnetic field $B = 1$ nG. The curves are shown in arbitrary units; for convenience they are normalized to 1 at the points of the maximum of distributions: $\max(f_{A,B}) = 1$.

Ref. [67]. In this case the distribution over τ is described as

$$f_A \equiv \int_0^\infty P(\tau, \zeta, r) d\zeta = \frac{4\pi^2 c}{r^2 \langle \theta_s^2 \rangle} \sum_{n=1}^\infty (-1)^{n-1} n^2 e^{-2\pi^2 n^2 y}. \quad (2.75)$$

with mean values for y :

$$\langle y \rangle = \frac{1}{12}, \quad \langle y^2 \rangle = \frac{7}{720}, \quad \Delta = \frac{1}{360}. \quad (2.76)$$

B. Protons arriving along the radius-vector at the registration point. For this case, substituting $x = 0$ into Eq. (2.60), we obtain

$$f_B \equiv P(\tau, \zeta = 0, r) = -\frac{c}{r^3 \langle \theta_s^2 \rangle^2} \sum_{n=1}^\infty \frac{z_n^2}{j_1'(z_n)} e^{-2z_n^2 y}, \quad (2.77)$$

where $0 < z_1 < z_2 < \dots$ are the zeros of the function $j_1(z)$, located in the region $z > 0$.

The functions f_A and f_B corresponding to Eqs. (2.75) and (2.77) are shown in Fig. 2.12.

As it follows from Eq. (2.58), the arrival time τ enters into P only in the form of combination of the variable y . Since

$$\lg y = \lg \tau - 2 \lg r - \lg \lambda - 2 \lg B + 2 \lg E + \text{const}, \quad (2.78)$$

the curves for other values of the relevant parameters, namely energy E , magnetic field

B , correlation length λ , and the distance to the source r , can be obtained by a simple shift along the τ -axis. However, it should be noted that Eq. (2.58) is obtained in the approximation of ignoring the energy losses of protons. Therefore for the large distances, $r \geq 100$ Mpc, and especially for large energies, $E \geq 10^{20}$ eV, Eq. (2.58) overestimates the arrival time, given that the energy of protons during their propagation significantly exceeds the energy at the registration point (see Fig. 1). Therefore, for large distance Eq. (2.58) should be treated as an upper limit for the time delay. On the other hand, since gamma-rays are produced at the very beginning of propagation of protons (within 10 Mpc or so), the curves calculated for a distance of order of 10 Mpc, provide a quite accurate estimate for the arrival times of gamma-rays.

2.4 Discussion

The angular, spectral and time distributions of UHE protons and the associated secondary gamma-rays and neutrinos propagating through the intergalactic radiation and magnetic fields have been studied based on the relevant solutions of the Boltzmann transport equation in the small-angle and continuous-energy-loss approximations. A general formalism for the treatment of the steady state distributions is provided in the form of relatively simple analytical presentations. The treatment of the secondary products, in particular the synchrotron gamma-radiation of electrons from photomeson interactions is reduced to the consecutive application of the solutions which schematically can be presented as

$$Q_p \rightarrow f_p \rightarrow Q_e \rightarrow f_e \rightarrow Q_\gamma \rightarrow f_\gamma.$$

Here Q_i denotes a source function and f_i denotes a distribution function. Q_p is specified as spherically symmetric source of protons. Q_e is obtained from distribution function of protons as the final product of photomeson interactions using the results Ref. [31]. Electrons generated in the pair production process of the first generation gamma-rays (from the decay of neutral π -mesons) are also included in Q_e . Finally, Q_γ corresponds to the synchrotron radiation of electrons with distribution function f_e formed in the chaotic magnetic field. We consider the case of strong magnetic field, $B \geq 10^{-9}$ G, when the electrons from photomeson interactions are cooled predominantly via synchrotron radiation. Such strong magnetic fields prevent the development of pair cascades at highest energies, and, at the same time, allow very effective conversion of the electromagnetic energy released at photomeson interactions into synchrotron radiation. The latter peaks at GeV and TeV energies. The electromagnetic cascades are developed at lower energies at which the suppression of the Compton cooling due to the Klein-Nishina effect is becom-

ing more relaxed. These sub-cascades are initiated basically by the electrons-positron pairs produced at the inverse Bethe-Heitler process. However, because of deflections of low-energy electrons in chaotic IGMF, the gamma-rays produced during the cascade development lose the directionality. Moreover, if the initial energy distribution of protons extends to 10^{20} eV, the electromagnetic energy released in photomeson interactions greatly exceeds the energy supply from the Bethe-Heitler process. On the other hand, the synchrotron radiation produced by highest energy secondary electrons not only provides an almost 100 % effective conversion into gamma-rays, but also preserves the initial direction of protons as long as the magnetic field does not exceed 10^{-7} G. Remarkably, while the main fraction of synchrotron gamma-rays and the highest energy neutrinos is produced in the proximity of the source, namely within the first ≈ 10 Mpc of the initial path of protons, the latter continue to suffer deflections with an enhanced rate (because of gradual decrease of energy during the propagation through the 2.7 CMBR), until they arrive to the observer. Therefore the gamma-ray and neutrino distributions appear to be more narrow than the angular distribution of protons.

The distribution functions f_p and f_e are obtained by applying the Green function of transport equation to the source functions Q_p and Q_e , respectively. The angular part of f_p and f_e is a normal (Gaussian-like) distribution, the dispersion of which depends on the energy loss rate, the deflection angle per unit length and the distance to the source. f_γ is calculated by integration along optical depth at different angles towards the source.

For specific realizations of the scenario of small-angle deflection of charged particles, assuming that they move in a statistically isotropic and homogeneous turbulent magnetic field with Kolmogorov spectrum, we considered the IGMF in the interval from 10^{-9} to 10^{-7} Gauss and adopted 1 Mpc for the correlation length. The propagation of protons is considered, as long as it concerns the energy losses, as rectilinear with diffusion in angle. Transport of electrons is considered in the homogeneous magnetic field with random direction since their propagation length is of the order or less of 1 Mpc.

Despite the small-angle scatterings, the related elongation of particle trajectories causes significant delays of their arrival time. The problem of propagation of particles can be described by the steady state solutions if the lifetime of the source exceeds the delay times. Otherwise the problem should be treated as a time-dependent propagation of particles injected in the intergalactic medium by an "impulsive" source of extremely high energy protons. This could be the case of solitary events like Gamma Ray Bursts or short periods ($T \leq 10^5$ year) of enhanced activity of active galactic nuclei. In this chapter we discuss the case of an "impulsive" source, ignoring the energy losses of protons. This approximation limits the applicability of the derived time distribution functions to the relatively nearby sources of protons located within 100 Mpc sphere

of the nearby Universe. On the other hand, since the bulk of synchrotron radiation of secondary electrons is produced close the source, $R \lesssim 10$ Mpc, the time-dependent solutions derived for protons, can describe quite accurately the delayed arrival times of synchrotron photons from sources located at cosmological distances.

The results presented in this chapter for gamma-rays are valid for intergalactic magnetic fields in a specific (but perhaps the most realistic) range between $B = 10^{-9}$ – 10^{-7} G. IGMF stronger than 10^{-7} G would lead to large deflections of charged particles, and thus violate the condition of small-angle approximation. On the other hand, IGMF weaker than 10^{-10} G would reduce dramatically the efficiency of the synchrotron radiation since in this case the electrons are cooled predominantly via Compton scattering. The pair cascades initiated by these electrons also lead to GeV and TeV gamma-ray emission, however these cascades form giant (hardly detectable) halos around the sources, unless the magnetic field is extremely weak, smaller than 10^{-15} G.

The realization of the scenario of synchrotron radiation of secondary electrons at the presence of a relatively modest magnetic field, $B \sim 10^{-9}$ G or larger, in the 10 Mpc proximity of the sources of highest energy cosmic rays, has higher chances to be detected, given the compact (almost point like) images at GeV and especially TeV energies, and the very high (10 per cent or more) efficiency of conversion of the energy of protons to high energy synchrotron gamma-rays. The fluxes of gamma-rays, protons and neutrinos shown in Figs. 2.7 – 2.11 are obtained assuming a power-law energy spectrum of protons with $\alpha = 2$ and total injection rate into IGM $L_p(\geq 1\text{GeV}) = 10^{44}$ erg/s. The expected gamma-ray fluxes are close to the sensitivities of *Fermi* LAT at GeV energies and the sensitivity of the Imaging Atmospheric Cherenkov telescope arrays at TeV energies. While the total power of production of highest energy cosmic rays hardly can exceed, except for very powerful AGN, 10^{44} erg/s, in the case of blazars with small beaming angles, the expected fluxes of gamma-rays could be significantly higher. Indeed, in the case of small deflections, the directions of injection of observed particles from the source are close to the observational line. Therefore the results for the spherically symmetric source remain valid also for the narrow jet with solid angle $\Omega_{beam} = \pi\vartheta^2$, where $\vartheta^2 \gtrsim \langle\theta^2\rangle$. Then the required power of the source (to be detected in gamma-rays) is reduced by a factor $\Omega_{beam}/4\pi$ which may be significantly small.

2.5 Summary

In this chapter the analytical solution of the Boltzmann transport equation has been obtained in the limit of the small-angle and continuous-energy-loss approximation. The solution comprises the rectilinear propagation with continuous energy losses and the

diffusion in the angle describing the random scattering in turbulent magnetic field. The Gaussian-like angular distribution is determined by the average deflection angle which depends on the particle energy and statistical properties of the magnetic field. In the calculations the statistically isotropic and homogeneous turbulent magnetic field with Kolmogorov spectrum and typical coherence length $\lambda = 1$ Mpc has been used.

The solution has been applied for the calculation of the energy and angular distributions of UHE protons from the spherically symmetric source embedded in magnetized region with the magnetic field strength of the level of $B = 10^{-9} - 10^{-7}$ G. It allowed us to find the distributions of the secondary particles produced in the photomeson and pair-production interactions of protons with CMB radiation. The ultrahigh energy secondary electrons and positrons lose most of the energy through synchrotron radiation on the nearly rectilinear part of the path producing compact (almost point-like) source of gamma rays in the direction of the source of UHE protons. The considerable part of population of the electrons and positrons is generated by secondary gamma rays through the pair creation on the radio background radiation. The propagation and deflection of the electrons and positrons has been taken into account for the calculation of angular and energy distributions of the synchrotron GeV and TeV gamma rays.

The spectra of the secondary gamma rays, protons and neutrinos and their dependence on the subtending observational angle are presented in Figs. 2.7–2.11 for different distances of the source and for different value of the intergalactic magnetic fields. The expected gamma-ray fluxes are close to the sensitivity of Fermi Lat at GeV energies and the sensitivity of the Imaging Atmospheric Cherenkov telescope arrays at TeV energies for the source with cosmic-ray luminosity $L_p(\geq 1\text{GeV}) = 10^{44}$ erg/s located at the distance 100 Mpc.

Appendix A: The Green function for spherically symmetric source

The Green function for spherically symmetric point source is obtained by integration of Eq. (2.8) over all directions of the vector \mathbf{n}_0 . Let's rewrite Eq. (2.8) in the following form:

$$G(\mathbf{r}, \mathbf{n}, \mathbf{n}_0, E, E_0) = \frac{\delta(S(E, E_0) - r)}{c\bar{\epsilon}(E)\pi^2\Delta} \exp\left(-\frac{A - \mathbf{B}\mathbf{n}_0}{\Delta}\right). \quad (2.79)$$

Here

$$\begin{aligned} A &= 2(A_1 r^2 - 2A_2 r + A_3) - 2A_2 r(1 - \mathbf{n}_r \mathbf{n}), \\ \mathbf{B} &= 2((A_1 r^2 - A_2 r)\mathbf{n}_r + (A_3 - A_2 r)\mathbf{n}), \end{aligned} \quad (2.80)$$

where $\mathbf{n}_r = \mathbf{r}/r$. Since the directions of \mathbf{n} , \mathbf{n}_0 and \mathbf{n}_r are close to each other,

$$\mathbf{B}\mathbf{n}_0 = |\mathbf{B}| \cos \theta_0 \approx |\mathbf{B}| \left(1 - \frac{\theta_0^2}{2}\right). \quad (2.81)$$

Performing integration by saddle point method we obtain:

$$\int \exp\left(-\frac{A - \mathbf{B}\mathbf{n}_0}{\Delta}\right) d\Omega_{\mathbf{n}_0} \approx \frac{2\pi\Delta}{|\mathbf{B}|} \exp\left(-\frac{A - |\mathbf{B}|}{\Delta}\right). \quad (2.82)$$

Taking into account

$$\mathbf{n}_r\mathbf{n} \approx 1 - \frac{\theta^2}{2}, \quad (2.83)$$

the expressions for A and $|\mathbf{B}|$ can be written:

$$\begin{aligned} A &= 2Dr^2 + \theta^2 A_2 r, \\ |\mathbf{B}| &= 2\sqrt{(Dr^2)^2 - \theta^2(A_1 r^2 - A_2 r)(A_3 - A_2 r)} \end{aligned} \quad (2.84)$$

where

$$D = A_1 - 2\frac{A_2}{r} + \frac{A_3}{r^2}. \quad (2.85)$$

Expanding $|\mathbf{B}|$ into series in terms of θ to the second-order term in exponent and retaining the first term in denominator we find

$$G_{sph}(r, \theta, E, E_0) = \frac{\delta(S(E, E_0) - r)}{c\bar{\epsilon}(E)r^2\pi D} \exp\left(-\frac{\theta^2}{D}\right). \quad (2.86)$$

Appendix B: Distribution function of electrons

After changing the order of integration in

$$f_e(\mathbf{r}, \mathbf{n}, E_e) = \int \hat{Q}_e(f_p(\mathbf{r}_0, \mathbf{n}_0, E_p)) G(\mathbf{r} - \mathbf{r}_0, \mathbf{n}, \mathbf{n}_0, E_e, E_{e0}) d\mathbf{r}_0 \Omega_{\mathbf{n}_0} dE_{e0} \quad (2.87)$$

we arrive at the following integral over directions of the emission of electrons \mathbf{n}_0 at the point \mathbf{r}_0 and directions of \mathbf{r}_0 :

$$\begin{aligned} I &= \int d\Omega_{\mathbf{n}_s} d\Omega_{\mathbf{n}_0} \exp\left(-\frac{(\mathbf{n}_0 - \mathbf{n}_s)^2}{D}\right) \exp\left(-\frac{A_1(\mathbf{r} - \mathbf{r}_0 - |\mathbf{r} - \mathbf{r}_0| \mathbf{n}_0)^2}{\Delta}\right) \\ &\quad \times \exp\left(\frac{2A_2(\mathbf{r} - \mathbf{r}_0 - |\mathbf{r} - \mathbf{r}_0| \mathbf{n}_0)(\mathbf{n} - \mathbf{n}_0) - A_3(\mathbf{n} - \mathbf{n}_0)^2}{\Delta}\right), \end{aligned} \quad (2.88)$$

where

$$\mathbf{r} = r\mathbf{n}_r, \quad \mathbf{r}_0 = r_0\mathbf{n}_s, \quad \mathbf{r} - \mathbf{r}_0 = r'\mathbf{n}_0, \quad (2.89)$$

Δ and D are defined in Eq. (2.4) and Eq. (2.14), respectively. Taking into account that all directions are close, the integral can be presented in the following form:

$$I = \int e^{-(A-\mathbf{B}\mathbf{n}_s)} d\Omega_{\mathbf{n}_s} d\Omega_{\mathbf{n}_0}, \quad (2.90)$$

where

$$\begin{aligned} A &= X_0 + X_1(1 - \mathbf{n}_r\mathbf{n}_0) + X_2(1 - \mathbf{n}_r\mathbf{n}) + X_3(1 - \mathbf{n}_0\mathbf{n}), \\ \mathbf{B} &= Y_1\mathbf{n}_0 + Y_2\mathbf{n} + Y_3\mathbf{n}_r. \end{aligned} \quad (2.91)$$

Here we introduce the following notations:

$$\begin{aligned} X_0 &= \frac{2}{D} + \frac{A_1}{\Delta}((r - r')^2 + r_0^2), \quad X_1 = \frac{2}{\Delta}(A_1r' - A_2)r, \quad X_2 = \frac{2}{\Delta}A_2r, \quad X_3 = \frac{2}{\Delta}(A_3 - A_2r'), \\ Y_1 &= \frac{2}{D} + \frac{2}{\Delta}(A_2 - A_1r')r_0, \quad Y_2 = -\frac{2}{\Delta}A_2r_0, \quad Y_3 = \frac{2}{\Delta}A_1rr_0. \end{aligned} \quad (2.92)$$

Since directions of \mathbf{n} , \mathbf{n}_0 and \mathbf{n}_r are close, we can expand $|\mathbf{B}|$ into series to the first order terms:

$$|\mathbf{B}| \approx \nu - \frac{Y_1Y_2}{\nu}(1 - \mathbf{n}_0\mathbf{n}) - \frac{Y_1Y_3}{\nu}(1 - \mathbf{n}_0\mathbf{n}_r) - \frac{Y_2Y_3}{\nu}(1 - \mathbf{n}\mathbf{n}_r), \quad (2.93)$$

where

$$\nu = Y_1 + Y_2 + Y_3. \quad (2.94)$$

The integration of I over $d\Omega_{\mathbf{n}_s}$ by saddle point method gives

$$I \approx \frac{2\pi}{\nu} \int e^{-(A-|\mathbf{B}|)} d\Omega_{\mathbf{n}_0} \quad (2.95)$$

To perform the integration over $d\Omega_{\mathbf{n}_0}$ by the same method, we present the expression in the exponent in the following form:

$$\begin{aligned}
 A - |\mathbf{B}| &= \underbrace{X_0 - \nu}_{Z_0} + \underbrace{\left(X_1 + \frac{Y_1 Y_3}{\nu}\right)}_{Z_1} (1 - \mathbf{n}_0 \mathbf{n}_r) \\
 &+ \underbrace{\left(X_2 + \frac{Y_2 Y_3}{\nu}\right)}_{Z_2} (1 - \mathbf{n} \mathbf{n}_r) + \underbrace{\left(X_3 + \frac{Y_1 Y_2}{\nu}\right)}_{Z_3} (1 - \mathbf{n}_0 \mathbf{n}) \\
 &= \underbrace{Z_0 + Z_1 + Z_3 + Z_2(1 - \mathbf{n} \mathbf{n}_r)}_{\tilde{A}} - \underbrace{(Z_1 \mathbf{n}_r + Z_3 \mathbf{n})}_{\tilde{\mathbf{B}}} \mathbf{n}_0 = \tilde{A} - \tilde{\mathbf{B}} \mathbf{n}_0.
 \end{aligned} \tag{2.96}$$

Expanding $|\tilde{\mathbf{B}}|$ into series

$$|\tilde{\mathbf{B}}| \approx \mu - \frac{Z_1 Z_3}{\mu} (1 - \mathbf{n} \mathbf{n}_r), \tag{2.97}$$

where

$$\mu = Z_1 + Z_3 \tag{2.98}$$

we find

$$I \approx \frac{4\pi^2}{\nu\mu} e^{-(\tilde{A} - |\tilde{\mathbf{B}}|)}. \tag{2.99}$$

Making replacements of all notations by their actual values and taking into account that

$$r' \approx r - r_0, \tag{2.100}$$

we finally obtain

$$I = \frac{\pi^2 \Delta D}{D_e r^2 + D r_0^2} \exp\left(-\frac{\theta^2 r^2}{D_e r^2 + D r_0^2}\right), \tag{2.101}$$

where

$$D_e = A_1 - 2\frac{A_2}{r} + \frac{A_3}{r^2} \tag{2.102}$$

and θ is the angle between \mathbf{n}_r and \mathbf{n} . The Integration over r_0 in the expression for $f_e(\mathbf{r}, \mathbf{n}, E_e)$ can be readily performed because of δ -function.

Appendix C: Distribution of arrival times in the case of "impulsive" source

In the case of spherical symmetry the proton distribution function $f = f(t, r, \mu)$ depends on time t , distance to the source r , and the variable $\mu = \cos \theta = (\mathbf{n} \mathbf{r})/r$. Here \mathbf{n} is

a unit vector towards the direction of the proton speed. Let's normalize f using the condition

$$\int_0^\infty dr \int_{-1}^1 d\mu r^2 f(t, r, \mu) = 1. \quad (2.103)$$

Then $r^2 f(t, r, \mu) dr d\mu$ is the probability that at the moment t the proton is located in the layer $(r, r + dr)$ and is moving in the direction within $(\mu, \mu + d\mu)$. Let assume that propagation of a single particle is fixed, i.e. the radius vector $\mathbf{r}_0(t)$ and the direction $\mathbf{n}_0(t)$ are certain functions of time. For this particle, the distributions over r and μ are described by δ -functions:

$$f_0(t, r, \mu) = \frac{1}{r^2} \delta(r - r_0(t)) \delta(\mu - \mu_0(t)), \quad (2.104)$$

where $\mu_0(t) = (\mathbf{n}_0(t) \mathbf{r}_0(t)) / r_0(t)$.

By averaging Eq. (2.104) over the ensemble of particles gives the distribution function f :

$$f(t, r, \mu) = \langle f_0(t, r, \mu) \rangle. \quad (2.105)$$

Let assume that for each particle $r_0(t)$ is a monotonically increasing function of time, i.e. there are no particles in the ensemble with $\mu \leq 0$. Then the equation $r = r_0(t)$ has a unique solution with $t = t_0(r)$, and thus one can write

$$\begin{aligned} \delta(r - r_0(t)) &= \frac{1}{dr_0/dt} \delta(t - t_0(r)) \\ &= \frac{1}{c\mu_0(t)} \delta(t - t_0(r)). \end{aligned} \quad (2.106)$$

Since in Eq. (2.104) this expression is multiplied to $\delta(\mu - \mu_0(t))$, in the denominator one can replace $\mu_0(t)$ by μ and take the factor $1/c\mu$ out of the integral. This yields

$$\begin{aligned} &\langle \delta(r - r_0(t)) \delta(\mu - \mu_0(t)) \rangle \\ &= \frac{1}{c\mu} \langle \delta(t - t_0(r)) \delta(\mu - \tilde{\mu}_0(r)) \rangle, \end{aligned} \quad (2.107)$$

where $\tilde{\mu}_0(r) = \mu_0(t_0(r))$.

Function $\langle \delta(t - t_0(r)) \delta(\mu - \tilde{\mu}_0(r)) \rangle$ has the meaning of the probability distribution for t and μ . Writing $t = \tau + r/c$, we obtain the probability distribution for τ and μ at the point r :

$$P(\tau, \mu, r) = \langle \delta(\tau + r/c - t_0(r)) \delta(\mu - \tilde{\mu}_0(r)) \rangle. \quad (2.108)$$

From this equation follows that P satisfies the condition of normalization

$$\int_0^\infty d\tau \int_{-1}^1 d\mu P(\tau, r, \mu) = 1. \quad (2.109)$$

Thus we arrive at the conclusion that the functions P and f are related as

$$P(\tau, \mu, r) = c\mu r^2 f(\tau + r/c, r, \mu) \equiv c\mu r^2 f'(\tau, r, \mu). \quad (2.110)$$

The distribution function satisfies the equation

$$\frac{1}{c} \frac{\partial f}{\partial t} + (\mathbf{n} \nabla) f = I, \quad (2.111)$$

where I is the collision integral. In the case of spherical symmetry

$$(\mathbf{n} \nabla) f = \mu \frac{\partial f}{\partial r} + \frac{1 - \mu^2}{r} \frac{\partial f}{\partial \mu}. \quad (2.112)$$

Replacing the variables in Eq. (2.111) from (t, r) to $(\tau = t - r/c, r)$ and presenting the collision integral in the Fokker-Planck approximation, we obtain

$$\begin{aligned} & \frac{1 - \mu}{c} \frac{\partial f'}{\partial \tau} + \mu \frac{\partial f'}{\partial r} + \frac{1 - \mu^2}{r} \frac{\partial f'}{\partial \mu} \\ &= \frac{\langle \theta_s^2 \rangle}{4} \frac{\partial}{\partial \mu} \left((1 - \mu^2) \frac{\partial f'}{\partial \mu} \right). \end{aligned} \quad (2.113)$$

In the case of an impulsive source and no scattering (i.e. $\langle \theta_s^2 \rangle = 0$) the distribution function normalized according to Eq. (2.103) is

$$f(t, r, \mu) = 2\pi \delta(\mathbf{r} - c\mathbf{n}t). \quad (2.114)$$

It is convenient to rewrite Eq. (2.114) in the form

$$f(t, r, \mu) = \frac{1}{cr^2} \delta(t - r/c) \delta(\mu - 1). \quad (2.115)$$

In order to demonstrate that the generalized functions in the forms given by Eqs. (2.114) and (2.115) are identical, one should multiply the right parts of these equations to an arbitrary function $h(\mathbf{r}, \mathbf{n})$ and integrate over the space coordinates and the direction

of the vector \mathbf{n} . This implies that at $\langle \theta_s^2 \rangle = 0$

$$f'(\tau, r, \mu) = \frac{1}{cr^2} \delta(\tau) \delta(\mu - 1). \quad (2.116)$$

It is clear, from general physical considerations, that in the limit $r \rightarrow 0$ Eq. (2.116) is valid also at $\langle \theta_s^2 \rangle \neq 0$. Therefore Eq. (2.116) can be treated as a boundary condition to Eq. (2.113) at the point $r = 0$.

An analytical solution of Eq. (2.113) is possible to derive in the small-angle approximation. In the case of multiple scattering, the average angle of deviation of at the distance r is of order of $(r\langle \theta_s^2 \rangle)^{1/2}$. Therefore for $r \ll 1/\langle \theta_s^2 \rangle$ one can use the small angle approximation. Let $\mu = 1 - \zeta/2$, and let us denote function $f'(\tau, r, 1 - \zeta/2)$ by $f'(\tau, r, \zeta)$. Assuming $\zeta \ll 1$, from Eq. (2.113) we obtain

$$\frac{\partial f'}{\partial r} + \frac{\zeta}{2c} \frac{\partial f'}{\partial \tau} - \frac{2\zeta}{r} \frac{\partial f'}{\partial \zeta} - \langle \theta_s^2 \rangle \frac{\partial}{\partial \zeta} \left(\zeta \frac{\partial f'}{\partial \zeta} \right) = 0. \quad (2.117)$$

To solve Eq. (2.117) we apply the Fourier transformation:

$$\tilde{f}'(\omega, r, \zeta) = \int_{-\infty}^{\infty} f'(\tau, r, \zeta) e^{-i\omega\tau} d\tau. \quad (2.118)$$

Function \tilde{f}' satisfies the equation

$$\frac{\partial \tilde{f}'}{\partial r} + \frac{i\omega\zeta}{2c} \tilde{f}' - \frac{2\zeta}{r} \frac{\partial \tilde{f}'}{\partial \zeta} - \langle \theta_s^2 \rangle \frac{\partial}{\partial \zeta} \left(\zeta \frac{\partial \tilde{f}'}{\partial \zeta} \right) = 0, \quad (2.119)$$

and the boundary condition given by Eq. (2.116) becomes

$$\tilde{f}'(\omega, r, \mu) = \frac{2}{cr^2} \delta(\zeta), \quad r \rightarrow 0. \quad (2.120)$$

Let's search the solution in the form

$$\tilde{f}' = e^{-\zeta a(r) + b(r)}, \quad (2.121)$$

where the functions $a(r)$, $b(r)$ do not depend on ζ . Substituting Eq. (2.121) in Eq. (2.119), we obtain the following ordinary differential equations:

$$\frac{da}{dr} = \frac{i\omega}{2c} + \frac{2}{r} a - \langle \theta_s^2 \rangle a^2, \quad (2.122)$$

$$\frac{db}{dr} = -\langle \theta_s^2 \rangle a. \quad (2.123)$$

The solution to Eq. (2.122) is

$$a(r) = \frac{1}{r\langle\theta_s^2\rangle} \frac{zj_0(z)}{j_1(z)}, \quad (2.124)$$

where $z = r\sqrt{\omega\langle\theta_s^2\rangle/(2ic)}$. The arbitrary constant which appears in the solution is chosen requiring singularity at the point $r = 0$. At $r \rightarrow 0$ the function $a = 3/r\langle\theta_s^2\rangle$. The solution to Eq. (2.123) is

$$b(r) = \ln\left(\frac{1}{r^3} \frac{z}{j_1(z)}\right) + \text{const}, \quad (2.125)$$

therefore the function \tilde{f}' is defined as

$$\tilde{f}' = C \frac{1}{r^3} \frac{z}{j_1(z)} \exp\left(-\frac{\zeta}{r\langle\theta_s^2\rangle} \frac{zj_0(z)}{j_1(z)}\right). \quad (2.126)$$

For determination of the constant C one should use the boundary condition given by Eq. (2.120). In the limit of small r , and using the relation

$$\lim_{r \rightarrow 0} \left(\frac{\beta}{r} e^{-\zeta\beta/r} \right) = \delta(\zeta), \quad (2.127)$$

we find

$$\tilde{f}' = C \frac{3}{r^3} \exp\left(-\frac{3\zeta}{r\langle\theta_s^2\rangle}\right) = C \frac{\langle\theta_s^2\rangle}{r^2} \delta(\zeta). \quad (2.128)$$

Comparing Eqs. (3.3) and (2.120), we obtain $C = 2/c\langle\theta_s^2\rangle$ and then using Eq. (2.110) we find P . In the small-angle approximation we can replace the factor μ in Eq. (2.110) by unity. In order to compare our results with the solution obtained in Ref. [67], we adopt $C = 1/c\langle\theta_s^2\rangle$, which is equivalent to the change of the condition of normalization, namely instead of Eq. (2.109) we use

$$\int_0^\infty d\tau \int_0^\infty d\zeta P(\tau, r, \zeta) = 1, \quad (2.129)$$

where, because of rapid convergence, the upper limit of integration over $d\zeta$ is set infinity. In order to present the result in the form given by Eqs. (2.58) – (2.60), one should introduce, instead of the variable ω , a new variable of integration $s = \omega r^2 \langle\theta_s^2\rangle / c$.

Appendix D: Emissivity function of synchrotron radiation in random magnetic fields

For the case of chaotic magnetic fields one should average out the standard formula for energy distribution of synchrotron radiation

$$\frac{dN_\gamma}{dE_\gamma dt} = \frac{\sqrt{3}}{2\pi} \frac{e^3 B}{m_e c^2 \hbar E_\gamma} F\left(\frac{E_\gamma}{E_c}\right), \quad (2.130)$$

where

$$F(x) = x \int_x^\infty K_{5/3}(\tau) d\tau, \quad E_c = \frac{3e\hbar B \gamma^2}{2m_e c}, \quad (2.131)$$

over directions of magnetic field. After taking the perpendicular to velocity component of magnetic field $B_\perp = B \sin \theta$, where θ is angle between \mathbf{B} and \mathbf{v} we come to the following double integral:

$$G(x) = \int \sin \theta F\left(\frac{x}{\sin \theta}\right) \frac{d\Omega}{4\pi} = \frac{1}{2} \int_0^\pi F\left(\frac{x}{\sin \theta}\right) \sin^2 \theta d\theta. \quad (2.132)$$

After changing the order of the integration it can be written as a single integral

$$G(x) = x \int_x^\infty K_{5/3}(\xi) \sqrt{1 - \frac{x^2}{\xi^2}} d\xi, \quad (2.133)$$

that can be expressed in terms of modified Bessel functions:

$$G(x) = \frac{x}{20} [(8 + 3x^2)(\kappa_{1/3})^2 + x\kappa_{2/3}(2\kappa_{1/3} - 3x\kappa_{2/3})], \quad (2.134)$$

where $\kappa_{1/3} = K_{1/3}(x/2)$, $\kappa_{2/3} = K_{2/3}(x/2)$. Note that while the function $F(x)$ has a maximum at $x = 0.2858$ ($\max F(x) = 0.9180$), the maximum of the function $G(x)$ is shifted towards smaller values: $x = 0.2292$ ($\max G(x) = 0.7126$). An alternative presentation for $G(x)$ in terms of Whittaker's function has been derived in Ref. [68]. The functions $F(x)$ and $G(x)$, as well as the ratio $G(x)/F(x)$ are shown in Fig. 2.13.

Although the function $G(x)$ in Eq. (D5) is presented in a quite compact and elegant form, for practical purposes it is convenient to have approximation which does not contain special functions. Here we propose such approximations for $F(x)$ and $G(x)$

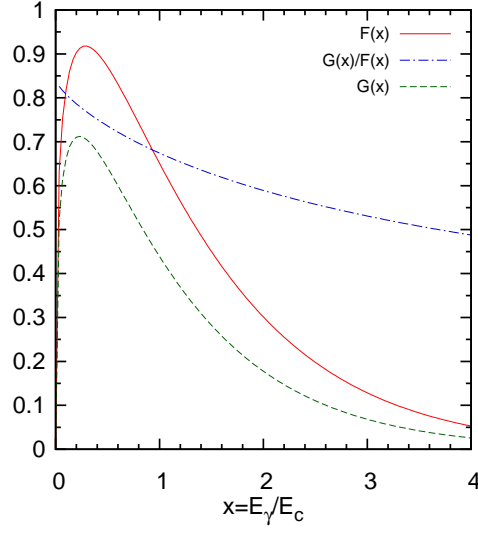


Figure 2.13: The emissivity functions for synchrotron radiation $F(x)$ and $G(x)$. The dashed-dotted line shows the ratio $G(x)/F(x)$.

which provide an accuracy better than 0.2 % over the entire range of variable x :

$$\tilde{F}(x) \approx 2.15x^{1/3}(1 + 3.06x)^{1/6} \frac{1 + 0.884x^{2/3} + 0.471x^{4/3}}{1 + 1.64x^{2/3} + 0.974x^{4/3}} e^{-x}, \quad (2.135)$$

$$\tilde{G}(x) \approx \frac{1.808x^{1/3}}{\sqrt{1 + 3.4x^{2/3}}} \frac{1 + 2.21x^{2/3} + 0.347x^{4/3}}{1 + 1.353x^{2/3} + 0.217x^{4/3}} e^{-x}. \quad (2.136)$$

3 Cosmologically distant UHE cosmic-ray accelerators

3.1 Cosmologically distant sources

For cosmologically distant sources embedded in denser ($n_{\text{ph}} \propto (1+z)^3$) and more energetic ($T \propto 1+z$) CMBR, protons lose their energy on distances significantly smaller than 100 Mpc. In the presence of magnetic field of strength $B = 10^{-9} - 10^{-8}$ G the high energy electrons produced in photomeson processes intensively emit synchrotron radiation in GeV range of energies. The electrons radiate most of their energy on almost rectilinear part of the path that gives, along with the small deflection of protons, collimated beam of gamma rays pointing to the acceleration site of UHE protons. Note that the considerable contribution to the high energy electrons is provided by the gamma rays produced in decay of mesons. The interaction of these gamma rays with cosmic radio background radiation occurs in the regime when the most of the energy goes to one of the component of the created electron-positron pair.

The probability of detection of cosmic ray sources via synchrotron radiation of secondary electrons strongly depends on the maximum energy of accelerated protons. In the case of sources with redshift $z \ll 1$, the interaction of protons with CMBR is effective only when the proton spectrum extends to 10^{20} eV and beyond. Since acceleration of protons to such high energies can be realized only at a unique combination of a few principal parameters, in particular the linear size of the source, the strength of the magnetic field, and the Lorentz factor of the bulk motion ([26]), the number of sources of 10^{20} eV cosmic rays can be quite limited compared to sources accelerating particles to $E_{\text{max}} \sim 10^{19}$ eV. Since protons at high redshifts interact with denser and more energetic photons of CMBR, the requirement to E_{max} is significantly relaxed, thus one should expect dramatic increase of the number of UHE cosmic ray sources surrounded by gamma-ray halos. Furthermore, at high redshifts the interaction of protons with CMBR via pair production (Berhe-Heitler) process begins to play an important role and a considerable part of proton energy is converted to less energetic electrons compared to electrons generated in photomesons reactions. Appearance of dense halos of

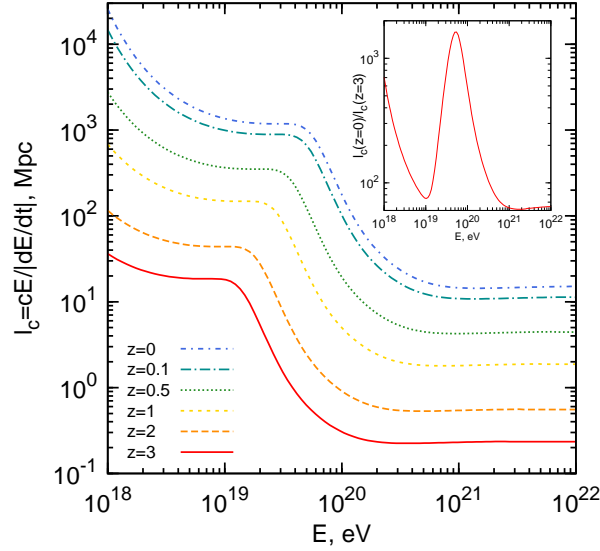


Figure 3.1: The cooling length of protons in the intergalactic medium due to interactions with photons of CMBR at different redshift. The ratio of cooling lengths at $z = 0$ and $z = 3$ are shown in the inset.

Bethe-Heitler electrons around the source at presence of magnetic field of the order of $B \sim 10^{-6}$ G (comparable to the field of clusters of galaxies) results in radiation dominated by synchrotron X-rays.

Below we study the energy and angular distribution of the synchrotron gamma-ray emission from cosmologically distant sources. The calculations are based on the approach developed in the previous sections combined with cosmological effects on propagation of gamma rays and protons. The space in the vicinity of the source, where all relevant processes occur, can be considered as conventional one. Therefore, taking into account denser ambient radiation at high redshifts, we can apply the developed formalism to calculation of the distribution function of gamma rays in the vicinity of the source. Using this function, we can easily obtain the distribution function of the observed radiation which has propagated cosmological distance (see Appendix).

3.2 Energy budget

An accelerator of UHE protons located at high redshift has appreciably different conditions of ambient media as compared to the ones in the nearby Universe. The photon field of CMB is denser and more energetic due to cosmological expansion. The increase of density by factor of $(1+z)^3$ leads to more frequent interactions of UHE protons with CMB that intensifies the energy loss rate. The average energy of photons is also

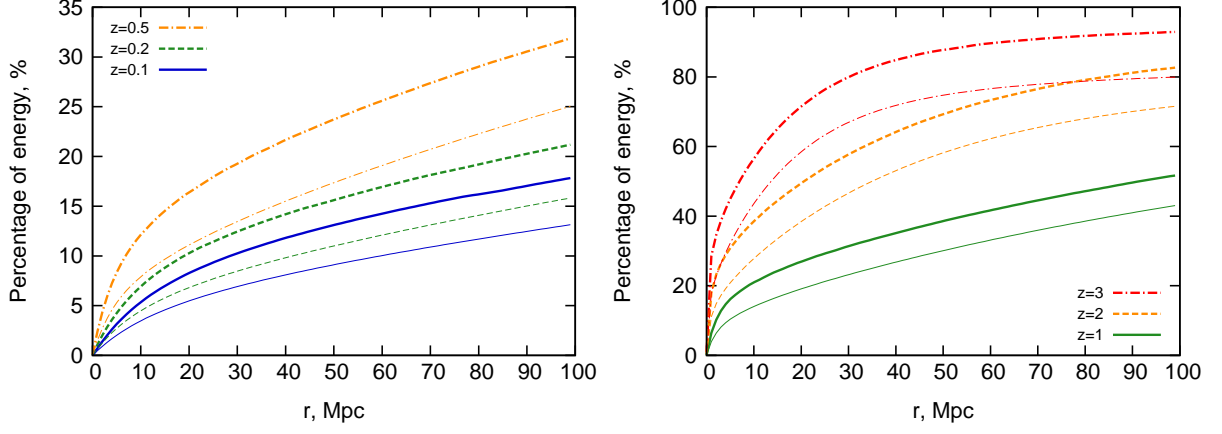


Figure 3.2: The fraction of the initial energy of protons with $E > 10^{18}$ eV lost (thick lines) and converted to the energy of electrons (thin lines) at the distance r from the source. The injected proton spectrum is assumed power-law with an exponential cutoff $J_p(E) = J_0 E^{-2} \exp(-E/E_0)$, with $E_0 = 3 \cdot 10^{20}$ eV.

increased by factor of $(1+z)$ that decreases the threshold energy of the interactions for protons. The energy loss rate of protons due to interaction with CMB at the epoch of redshift z is expressed in terms of the present loss rate $\beta(E) = -\frac{1}{E} \frac{dE}{dt}$ as

$$\beta(E, z) = (1+z)^3 \beta_0((1+z)E). \quad (3.1)$$

It is convenient to present this relation in terms of the cooling length which is shown in Fig. 3.1. The cubic dependence on redshift leads to considerable decrease of the cooling length. In particular, for the constant losses at highest energies, $E \geq 10^{21}$ eV, it is reduced from ≈ 15 Mpc at the present epoch to ≈ 0.2 Mpc at $z = 3$. The plateau of constant losses itself extends to lower energies due to the energy shift. At lower energies, the combination of the effects related to the energy shift and the increase of density jointly results in reduction of cooling length by a factor larger than $(1+z)^3$. Indeed, as it is seen from the inset in Fig. 3.1 the reduction of the proton cooling length can be an order of magnitude larger. The peaks show domains where energy loss at $z = 3$ is the most intensive relative to the case of present epoch. If the energy cutoff in the initial proton spectrum falls into this domain, the advantage of energy extraction at cosmological distances becomes more significant. Moreover, at $E = 10^{18}$ eV, the cooling length is reduced from $\geq 10^4$ Mpc at $z = 0$ to tens of Mpc at $z = 3$. It is interesting to note that the energy loss rate of protons of energy $E < 10^{19}$ eV at $z = 3$ is comparable to the loss rate of $E \geq 10^{20}$ eV protons at the present epoch.

Fig. 3.2 describes the evolution of proton energy losses and the efficiency of their

conversion to the electron component of secondaries with the distance to the source at different redshifts. The electron component includes the electrons produced through all channels under consideration: pair production by protons, decay of charged mesons produced in photomeson processes and pair production by gamma rays produced from decay of neutral mesons. As mentioned above, in the latter process almost all energy of the photon goes to the energy of one of the electrons. Therefore the gamma rays can be treated as electrons. Then the energy taken away by neutrinos is the difference between the energy lost by protons and the energy converted to electrons. As can be seen from Fig. 3.2, the protons with initial energies $E > 10^{18}$ lose only 18% of their total energy after passing $r = 100$ Mpc at the redshift $z = 0.1$, whereas at redshift $z = 3$ the same protons lose 93% of the available energy already at $r = 70$ Mpc, where the saturation begins. It can be explained by the fact that the cooling length of protons in the range $E > 10^{18}$ eV do not exceed tens of Mpc at $z = 3$, while for redshifts $z \ll 1$, the protons have the cooling length of cosmological scales relative to pair production process. As the contribution of pair production process increases, the share of energy lost by protons that goes to electrons increases from 74% at $z = 0.1$ to 86% at $z = 3$.

The fraction of the initial energy of the protons with $E > 10^{18}$ eV that can be converted to the electrons generated at photomeson processes depends strongly on the position of the cutoff energy. Left panel of Fig. 3.3 shows that the efficiency of extraction of proton energy and its transfer to this component of electrons grows with the redshift, and at $z = 3$ all available for conversion energy is transferred at first 5 Mpc. The fraction of proton energy taken away by neutrinos in photomeson processes is 42% independently of redshift. Due to more energetic photons of CMBR, the threshold of photomeson interactions is shifted to lower energies that leads to the increase of extracted energy from 6% to 17% (see Fig. 3.3). However, as pair production begins to play a significant role at high redshifts the share of the electrons generated in photomeson processes is decreased, from 49 % to 22 % at the distance $r = 100$ Mpc.

The importance of the shift of the reaction threshold on production of electrons becomes more obvious if the protons with energies close to threshold and higher are taken into account. The percentage of initial energy of protons with energies $E > 10^{19}$ eV which is converted to the energy of electrons is presented in the right panel of Fig. 3.3. While at $z = 0.1$ the production of electrons due to photomeson processes dominate at all distances smaller than 100 Mpc, at high redshifts the pair production prevails.

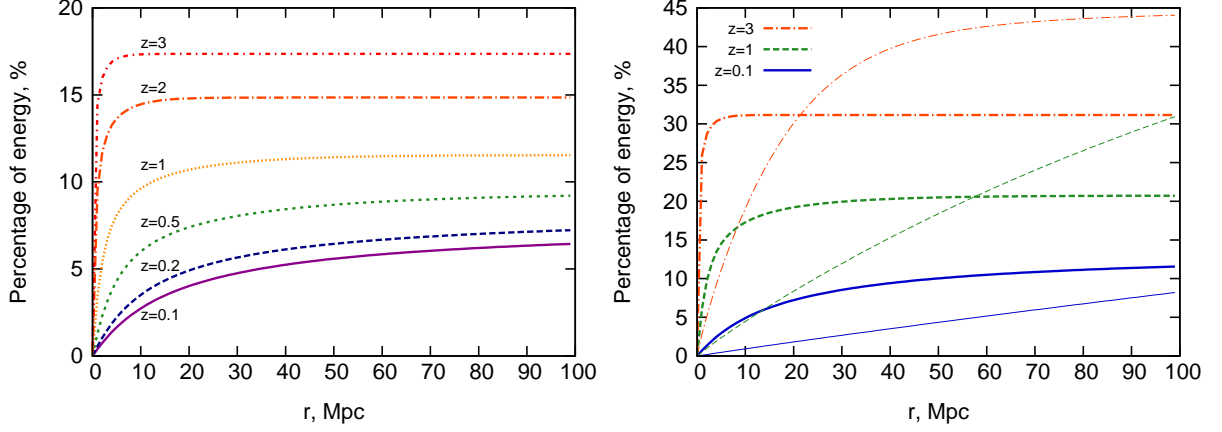


Figure 3.3: Left panel: the fraction of the initial energy of protons with energy $E > 10^{18}$ eV converted to the energy of electrons from *photomeson production* at distance r from the source. Right panel: the percentage of the initial energy of protons with energy $E > 10^{19}$ eV converted to the energy of electrons from photomeson production (thick lines) and electrons from pair production (thin lines) at the distance r from the source.

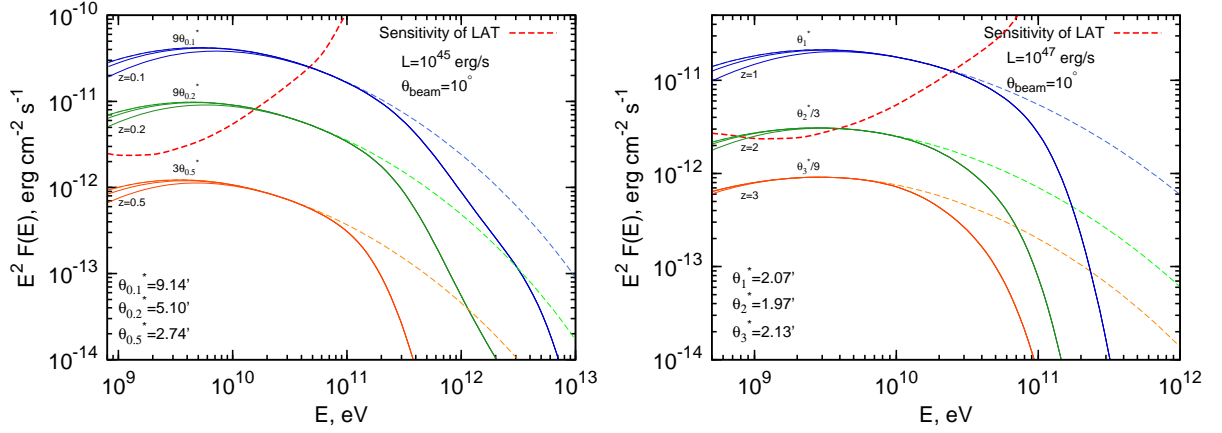


Figure 3.4: Spectral energy distribution of gamma rays observed within different angles in the direction to the source with EBL absorption (thick lines) and without one (dashed lines) indicated for maximum angles. θ_z^* is apparent angular size of the region with radius 0.5 Mpc from the distance with redshift z . The angles are specified in the units of corresponding θ_z^* and differ from each other by factor of 3. The maximum angles for every redshift, the total power of injection of protons L and the beaming angle θ_{beam} are indicated.

3.3 Gamma-ray source

Having the highest energy among secondaries, the electrons generated in photomeson processes emit almost all their energy via synchrotron radiation. Therefore, because of the shift of the threshold of photomeson interactions, the intensity of synchrotron gamma rays is increased with the redshift of the source. On the other hand, the reduction of cooling length of protons results in reduction of the apparent angular size of the region emitting synchrotron radiation, in addition to the diminution because of geometrical factor.

Fig. 3.4 shows spectral energy distribution of synchrotron gamma rays observed within different polar angle in the direction to the source of protons. The geometry of expanding Universe leads to more sophisticated dependence of apparent angular size on distance compared to the $\sim 1/r$ dependence for the local Universe. It is useful to define a reference angle θ_z^* which is equal to the angular size of the region with the radius $r = 0.5$ Mpc located at the redshift z . Expressing the angles in units of corresponding reference angles, we can compare the regions located at different redshifts eliminating the geometrical factor. As expected, at large redshifts the reference angle increases with z (see Appendix 3.6, Fig. 3.8). In Fig. 3.4 for each redshift the fluxes are presented within three polar angles which differ from each other by factor of 3 and are expressed in the units of corresponding reference angle. The maximal angle indicated in plots is the polar angle within which the total flux is observed. Comparison of the maximal angles in units of reference angles shows a tendency of decreasing the angular size of the region of secondary synchrotron radiation with redshift, from $9\theta_{0.1}^*$ to $\theta_3^*/9$.

The interaction of synchrotron gamma rays with extragalactic background light (EBL) leads to considerable attenuation of the flux. As it is seen from Fig. 3.4 the intergalactic absorption becomes substantial, depending on the distance to the source, from TeV energies down to tens of GeV energy range. For calculation of the absorption of gamma rays, the model of EBL developed in [69] have been applied.

At high redshifts, the electrons from photomeson reactions are produced close to the acceleration sites of protons. In this case a considerable part of emitting electrons might be found in much stronger magnetic field compared to the average intergalactic field. The energy spectrum of synchrotron radiation of secondary electrons is shifted linearly with change of the strength of magnetic field to keep the ratio E_γ/B constant (see [17]). Therefore the increase of the strength of magnetic field leads to the shift of radiation spectrum towards higher energies; if the radiation extends to TeV energies, the intergalactic absorption becomes quite violent; this results in the dissipation of almost the entire radiation. The absorbed gamma rays initiate cascades which contribute to

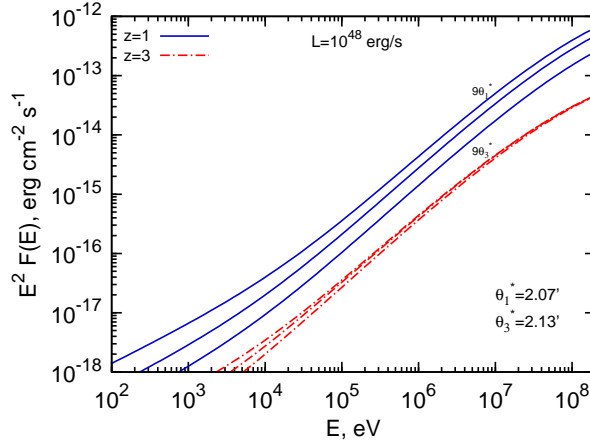


Figure 3.5: Energy flux distribution of gamma- and X-rays observed within different angles in the direction of the source for the case of homogeneous magnetic field $B = 1$ nG. Other parameters are the same as in previous figures.

the diffuse extragalactic background radiation.

Keeping in mind the sensitivity of instruments such as *Fermi*, the detection of the collimated synchrotron radiation from sources located at high redshifts is possible only in case of very powerful AGN. The anisotropic injection of UHE cosmic rays allows to reduce the required power of source. Until deflection of protons is smaller than the angle of a jet, there is no difference between the spherically symmetric and anisotropic case. In both cases the observer will see identical pictures. For the given power of injection the existence of anisotropy with the opening angle θ_{beam} of jet means the increase of the flux of gamma rays by the factor $4/\theta_{beam}^2$ compared to the spherically symmetric case. The fluxes of synchrotron gamma rays in Fig. 3.4 are calculated for the case of $\theta_{beam} = 10^\circ$. The deflection of protons is smaller than this value of the opening angle while protons produce secondary particles. It is seen from Fig. 3.4 that at the power of proton injection $L = 10^{45} - 10^{47}$ erg/s, the fluxes of gamma rays can exceed the sensitivity (minimum detectable fluxes) of *Fermi LAT* [70]. The resolution of the *Fermi LAT* varies in dependence of photon energy from $42'$ at $E = 10^9$ eV to $4.2'$ at $E = 10^{11}$ eV [70]. Already for the source located at $z = 0.2$ the angular size is $46'$, thus the source of gamma rays would be seen as extended one only if $z < 0.2$.

3.4 X-ray emission

Protons lose part of their energy via pair production. The pair-produced electrons have lower energies compared to the electrons produced in photomeson processes and

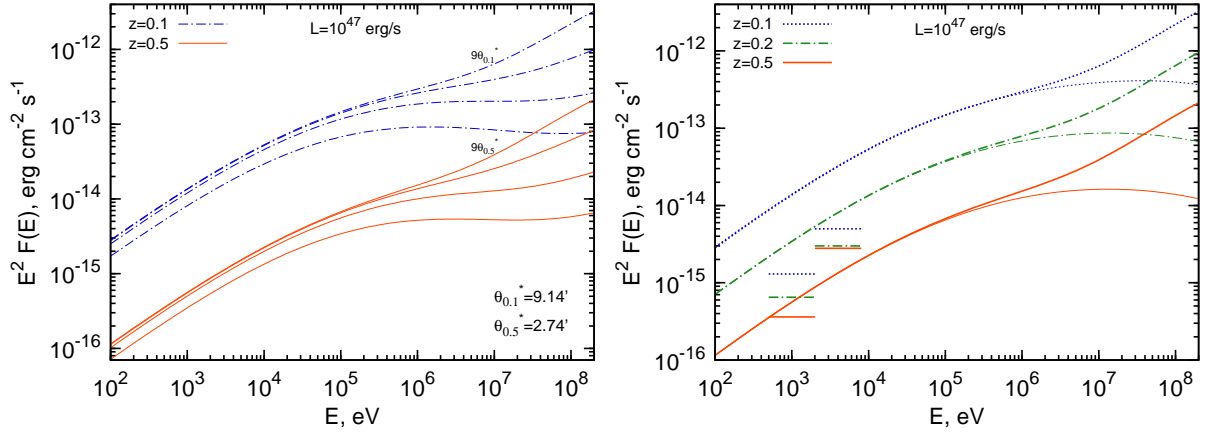


Figure 3.6: Energy flux distribution of gamma- and X-rays observed within different angles in the direction of the source (left panel) and within maximum angle (right panel) for the case of two-band magnetic field. For the right panel, the total radiation from photomeson and pair production electrons (upper lines) and the radiation from pair production electrons (lower lines) are indicated. Horizontal segments present the *Chandra* sensitivity for the corresponding maximum angles of observation. The other parameters are the same as in previous figures.

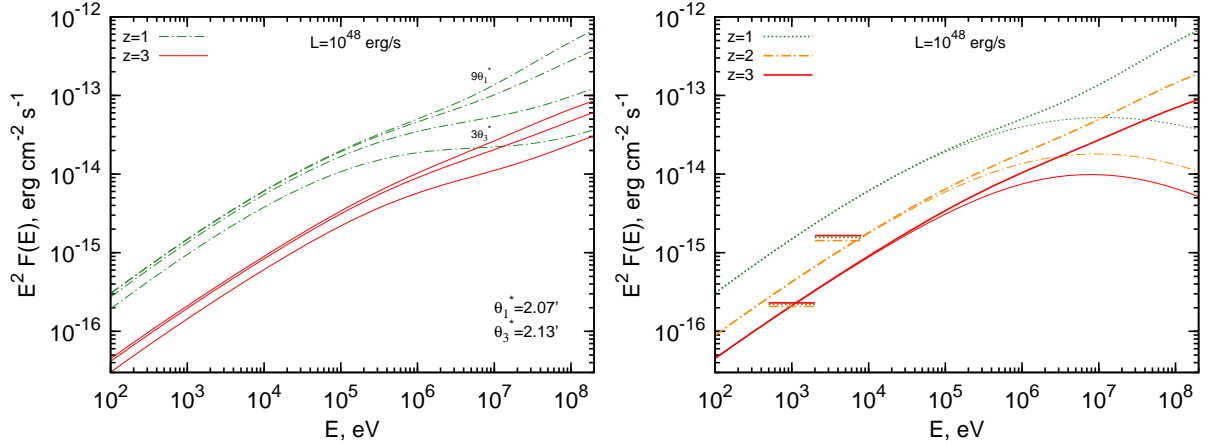


Figure 3.7: The same as Fig. 3.6 but for $z = 1, 2, 3$ and the total power of injection of protons $L = 10^{48}$ erg/s .

emit synchrotron radiation in the lower band of spectrum. At high redshifts the mean free path of protons relative to pair production process is decreased and generated electrons are located in more compact region. Moreover, the fraction of energy of protons converted to the secondary electron component is increased and reaches to 68% at $z = 3$ (see Fig. 3.2, 3.3).

Synchrotron radiation for the strength of IGMF of $B = 10^{-9}$ G and inverse Compton (IC) scattering give equal contribution to electron losses at energy $E \approx 3 \cdot 10^{18}$ eV. At lower energies electrons lose their energy predominantly through IC scattering. Scattering is carried out at Klein-Nishina regime and almost all energy is transferred to photon. In turn the high energy photon produce electron-positron pair due to interaction with CMBR and most of the energy goes to one component of the pair which again suffer IC scattering. This process can be considered as alternation of the particle state with gradual reduction of energy. The electromagnetic cascade produces a huge halo of gamma rays with energy in GeV region. Region of synchrotron radiation is more compact, and electrons radiate it at the place of their generation. In spite of this the region is still quite extended as can be seen from angular distribution on Fig. 3.5. The flux of synchrotron radiation drops at low energies and becomes very small in X-ray region. The calculation of fluxes presented on Fig. 3.5 takes into account only homogeneous IGMF with strength $B = 10^{-9}$ G. However, the strength of magnetic fields close to the accelerator can be much higher. To take this into account, we consider the following spatial distribution for IGMF magnetic field:

$$B = B_{cl} \left(\frac{r_0}{r + r_0} \right)^3 + B_0, \quad (3.2)$$

where $B_{cl} = 10^{-6}$ G is magnetic field in the cluster of galaxies with characteristic size of $r_0 = 1$ Mpc, $B_0 = 10^{-9}$ G is IGMF. Such a dependence of the magnetic field has been chosen to have a dipole behavior at large distances. For this case the energy and angular distributions of gamma- and X-rays are presented on left panels of Fig. 3.6 and 3.7. This magnetic field gives considerable increase of the fluxes of synchrotron radiation at low energies which is generated at small region close to the source and, therefore, has narrow angular distribution. Right panels shows that the contribution of electrons produced in pair production process (lower lines) is dominant in X-ray region, whereas gamma rays are generated predominantly by electrons produced in photomeson processes. Horizontal segments indicate sensitivity of *Chandra* [71, 72] for corresponding maximum angles of observation. As can be seen the low energy part of X-rays (0.5 – 2 keV) is detectable for specified power of injection of protons, whereas the radiation at higher energies can be missing for sources located at high redshifts since *Chandra* is less sensitive in the range

of energies $2 - 8$ keV.

As follows from Fig. 3.6 and 3.7, the electrons produced in photomeson processes provide the main contribution to synchrotron gamma rays, although the most of energy lost by protons is contained in the low energy component of secondary electrons from the pair production process. The radiation of this component can be detected only in the case of a quite large, $B_{cl} \simeq 10^{-6}$ G magnetic field around the source. This can happen if the source is located inside a cluster of galaxies with a typical size of 1 Mpc. Nevertheless, even in the case of intensive pair production that takes place in cosmologically distant objects, only a small fraction of pairs is produced in the relatively compact region with a linear size of ~ 1 Mpc (see Fig. 3.2); the most of energy of protons is converted to the energy of extended gamma ray halo.

3.5 Discussion

High energy gamma rays are unavoidably formed around the sources of UHE cosmic rays because of synchrotron radiation of secondary electrons produced at interactions of highest energy protons with the cosmic microwave background radiation. In the previous chapter we have shown that even for relatively large intergalactic magnetic fields in the neighborhood of UHE cosmic ray accelerators, $B \sim 10^{-7} - 10^{-9}$ G, these process lead to formation of high-energy point-like gamma-ray sources. Because of relatively weak gamma ray signals, the chances of detection of such sources are higher for objects located in the nearby Universe, namely at distances less than 100 Mpc. Since the efficiency of conversion of the proton energy to secondary gamma rays is dramatically reduced at protons energies $E \leq 10^{20}$ eV, one may hope to detect gamma rays only from extreme objects accelerating protons to energies 10^{20} eV and beyond. Given the fact that this requirement can be satisfied only in the case of unique combination of parameters, as well as the limited volume of the ≤ 100 Mpc region, realistically one can expect not a very large number of such sources. One can gain a lot if extends the study to cosmological distances. First of all, this allows to probe the most powerful objects in the Universe (e.g. quasars and AGNs) in which more favorable conditions can be formed for acceleration of protons to energies 10^{20} eV. Secondly, because of higher temperature of the CMBR at cosmological epochs, i.e. because of denser and hotter relic photons, less energetic protons (with energy down to 10^{19} eV) can lead to effective production of gamma rays. Given that the conditions of acceleration of protons to 10^{19} eV in suspected cosmic accelerators are much relaxed as compared to the 10^{20} eV extreme accelerators (see [26]), we should expect dramatic increase of such gamma-ray sources. Another factor of enhancement of number of sources comes from the increase of the volume of

the explored region to redshifts $z \geq 3$. An obvious caveat in this case is the decrease of gamma ray flux. However, this factor can be at least partly compensated by the huge power of objects in the remote Universe. Moreover, due to dramatic reduction of mean free paths of UHE protons at cosmological epochs $z \geq 1$, the conversion efficiency of proton energy to gamma rays is increased almost an order of magnitude, which makes these objects an extremely effective gamma-ray emitters. Finally, since the secondary gamma-ray emission generally follows the direction of parent protons, the beamed cosmic accelerators like GRBs and blazars seem to be quite attractive targets for search of point-like but steady GeV gamma-ray emission from cosmologically distant objects.

3.6 Summary

In this chapter the scenario of synchrotron gamma-ray signatures of cosmologically distant UHE cosmic-ray accelerators has been considered. The probability of detection of cosmic ray sources via synchrotron radiation of secondary electrons strongly depends on the maximum energy of accelerated protons. In the case of sources with redshift $z \ll 1$, the interaction of protons with CMB radiation is effective only when the proton spectrum extends to $E_{\text{max}} = 10^{20}\text{eV}$ and beyond. Since protons at high redshifts interact with denser ($n_{\text{ph}} \propto (1+z)^3$) and more energetic ($T \propto 1+z$) photons of CMB radiation, the requirement to E_{max} is significantly relaxed, thus one should expect dramatic increase of the number of UHE cosmic ray sources surrounded by gamma-ray halos. Protons lose their energy on distances significantly smaller than 100 Mpc and produce the compact gamma-ray source.

The energy conversion from UHE protons to the synchrotron radiation of the secondary electron has been calculated for different redshifts. The significant increase of the efficiency is shown for cosmologically distant sources. Using the formalism of the previous chapter combined with effects in the expanding Universe the angular and spectral distributions of radiation in the gamma- and X-ray bands has been calculated and discussed in the context of their detectability by the Fermi LAT and Chandra observatories.

Appendix: Angular size of sources at large redshifts

If the radiation is generated on scales smaller than cosmological ones, the relevant processes can be considered as they take place in the conventional stationary Euclidean space. However, when radiation propagates over cosmological distances, the expansion of space should be taken into account. Based on the law of free motion of massless

particles in expanding space, one can find the distribution function of photons at the observation point. Then we need to convert the distribution function calculated in the reference frame with origin at the source to the reference frame of the observer ([73]). In the present chapter the free propagation of photons is considered in the flat expanding Universe with parameters $\Omega_\Lambda = 0.73$, $\Omega_m = 0.27$ and $H_0 = 71$ km/s Mpc.

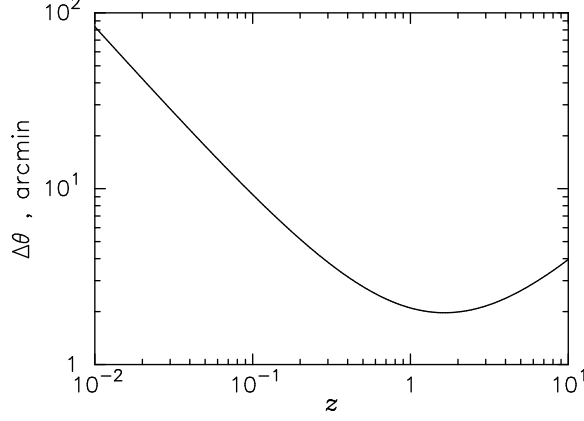


Figure 3.8: Angular size of the source with diameter $D = 1$ Mpc located at different redshifts z .

We consider an isotropic gamma-ray source of radius R_* located at redshift z . Let us assume that photons escape this region with spherically symmetric distribution $f_z(E, \theta)$, where E is the energy of photon and θ is the angle between photon momentum and radial direction at the escape point. Finally we assume that after the escape gamma rays propagate freely. In the case of small angles the distribution function $f_0(z, E, \Omega(\theta))$ of gamma rays at the observation point integrated over the solid angle Ω (with polar angle θ) can be expressed in the following form:

$$f_0(z, E, \Omega(\theta)) = 2\pi \left(\frac{\Theta_*}{1+z} \right)^2 \int_0^{\theta/\Theta_*} f_z(E(1+z), x) x dx, \quad (3.3)$$

where

$$\Theta_* = \left(\frac{c}{H_0 R_* (1+z)} \int_0^z \frac{dz'}{\sqrt{\Omega_m (1+z')^3 + \Omega_\Lambda}} \right)^{-1}. \quad (3.4)$$

The final result (3.3) differs from analogous one corresponding to the stationary space by the dependence on the redshift as well as by the nonlinear dependence of angular size on distance. The latter is determined by the parameter Θ_* given by Eq. (3.4). The parameter $\Delta\theta = 2\Theta_*$ has the meaning the angular size of the isotropically emitting source. In the case of anisotropic source, the angular size of radiation cannot be arbitrary

large and is limited by $\Delta\theta$. In Fig. 3.8 we show the angular size of the emission region with diameter $D = 2R_* = 1$ Mpc. The parameter $\Delta\theta$ has a minimum 1.95 arcmin at redshift $z = 1.64$ when recession velocity equals to the speed of light c ([73]).

4 The case of weak intergalactic magnetic fields

4.1 Time structure of gamma-ray signals

Active Galactic Nuclei (AGN) are expected to be sources of both cosmic rays and gamma rays. While gamma rays have been observed from a number of blazars, the identification of cosmic rays with their sources is impossible (except at the highest energies), because the Galactic magnetic fields change their directions considerably. However, as long as the intergalactic magnetic fields are relatively small, cosmic rays produced in blazars can travel close to the line of sight and produce secondary gamma rays which would significantly contribute to the radiation observed from the direction of the point sources. For nearby blazars such contributions are expected to be small in comparison with direct gamma-ray signals reaching Earth. However, for more distant blazars, the line-of-sight produced gamma rays can dominate over the direct gamma rays from the source [53]. The transition occurs because the primary gamma rays are filtered out in their interactions with extragalactic background light (EBL), while the fraction of secondary gamma rays produced by cosmic rays in intergalactic space grows with distance traveled. Based on the spectra of individual blazars [53, 51, 52] and on the trend in spectral softening [74], one expects the secondary contribution to be important for redshifts $z > 0.15$ and energies $E > 1$ TeV.

The intrinsic gamma-ray spectra of some blazars, after correction for absorption in EBL, appear extremely hard, challenging the standard, e.g. the synchrotron-self-Compton (SSC) or External Compton models of blazars. Several solutions to this problem have been proposed. Intergalactic cascading of gamma rays from blazars in the case of very weak intergalactic magnetic fields (IGMFs) can increase the effective mean free path of gamma-rays [65, 75], however, for distant blazars this effect alone appears to be insufficient to explain the gamma-ray spectra above 1 TeV. The very hard spectra of primary gamma rays [76, 77, 78], or special features in the sources [79] can help reconcile the data with theoretical predictions, at the cost of introducing some *ad hoc* assumptions. Hypothetical new particles [80, 81] and Lorentz invariance violation [82]

have been invoked to explain the data.

The inclusion of cosmic-ray contribution offers an alternative solution to the problem. Indeed, since a significant fraction of gamma rays in this model is produced relatively close to the observer, this model reduces dramatically the impact of gamma-ray absorption in EBL. This is illustrated in Fig. 4.1. Protons with energy $E \geq 10^{16}$ eV propagating through weak IGMFs without strong deviations from the line of sight can carry energy from the source close to the observer and can generate a substantial gamma-ray flux at multi-TeV energies. Remarkably, the predicted spectra of secondary gamma rays depend only on the source redshift (determined from independent observations). For each source, the power emitted in cosmic rays is the only fitting parameter which can be used to fit the data. As long as the source redshifts are known, the predictions of this model are solid and robust. The spectra calculated for the redshifts of all observed distant blazars provide a very good fit to observational data [53, 51, 52, 83], with a reasonable required luminosities in cosmic rays assuming that the escape of protons from the source is strongly beamed toward the observer [52, 84].

Confirmation of this model by future observations will have several important consequences. It will imply that (i) cosmic rays are, indeed, accelerated in AGN, as has long been suspected, but never before confirmed by observations; (ii) intergalactic magnetic fields are fairly small, of the order of several femtogauss (10^{-15} G) or lower [85]; and (iii) the problem of intergalactic gamma-rays can be somewhat relaxed, and consequently the upper limits on EBL derived while neglecting the cosmic-ray contributions may need be revised. Within this model, the expected temporal structure of signals from distant blazars at the highest energies should reflect the time delays cosmic rays undergo in the intergalactic magnetic fields. We note that while time variability has been observed for *nearby* TeV blazars at TeV energies and for distant TeV blazars at energies above a few hundred GeV, no variability has been reported so far for *distant* TeV blazars at *TeV energies*. Here we call *distant* those blazars that have large enough redshifts for the primary TeV gamma-rays to die out. Based on the spectral fits [53, 51, 52, 83], and the spectral softening of blazars [74], one concludes that most blazars with redshift $z \geq 0.15$ should fall in this category. Since the ratio of gamma-ray luminosity to cosmic-ray luminosity can vary from source to source, one expects a mixed population to exist at some intermediate redshifts $0.1 < z < 0.15$, where stronger cosmic ray emitters should be observed in secondary gamma rays, while stronger gamma ray emitters should be observed in primary gamma rays. Furthermore, if stronger IGMFs exist in the directions of specific sources, the secondary contribution can be suppressed. For example, PKS 2155-304 at $z = 0.12$ is an example of a source at an intermediate redshift from which primary signals are observed, as indicated by its TeV variability [86]. Whether

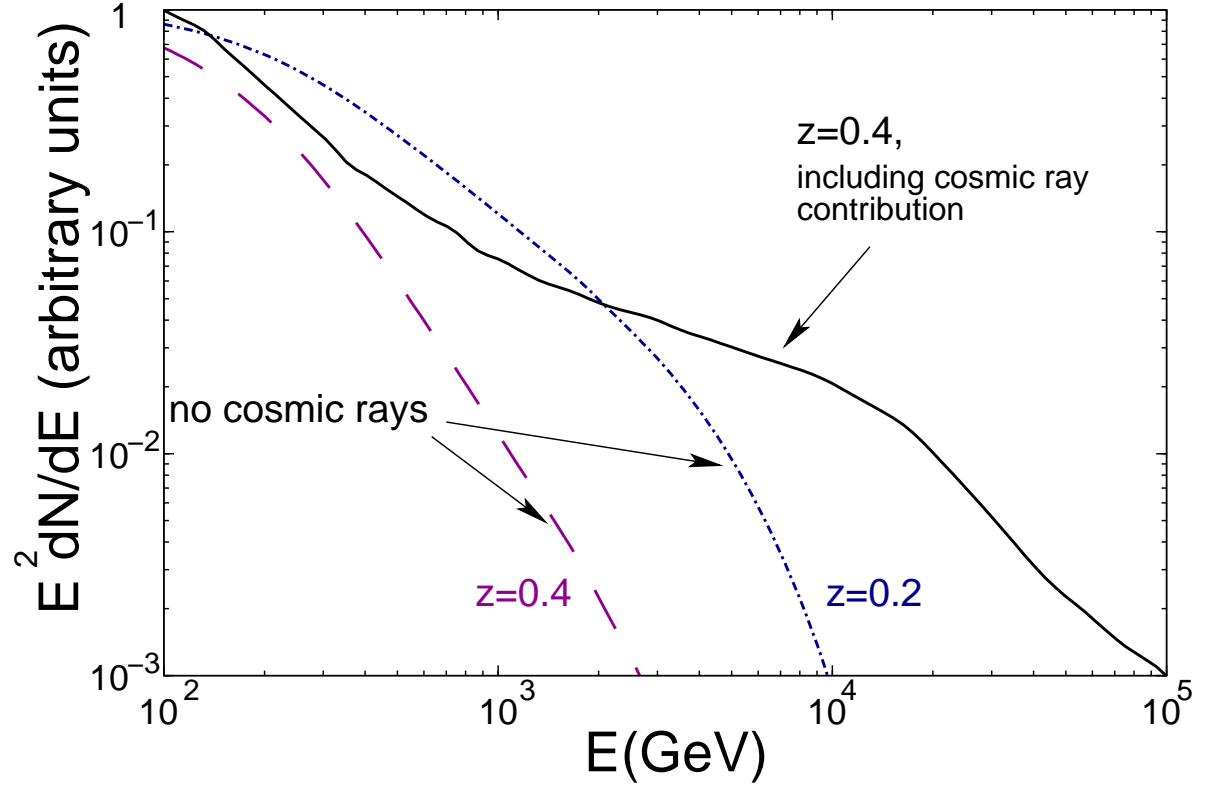


Figure 4.1: Secondary gamma rays produced in line-of-sight interactions of cosmic rays result in harder spectra for distant sources. Since most of the observed photons are produced relatively close to the observer, there is less attenuation due to the interactions with EBL.

the lack of TeV variability is a generic feature of distant blazars, or merely an artifact of low statistics in multi-TeV photons, should be clarified in future observations. An important issue in this context is the knowledge of the spectral and temporal features of the radiation predicted by the model. The spectral features of the radiation have been studied in detail by [52].

In this chapter we consider the extent to which the time variability at high energies should be erased by the cosmic ray propagation delays. We will focus on calculating the Green's function, which corresponds to a time delay from an infinitely narrow pulse of protons at the source. Realistic time profiles can be obtained by convolving the time-dependent source luminosity with this Green's function. However, since a fair fraction of the blazar flaring activity occurs on the time scales much shorter than those we discuss below, in many cases the Green's function can be interpreted as a distribution of photon arrival times from a flaring source. In applications of our method to data analysis, one can employ time-dependent templates inferred from lower energies.

4.2 Basic estimates and scaling laws

There is no doubt that, for nearby blazars, the primary gamma rays produced at the source are responsible for most of the observed radiation. While these objects can also produce cosmic rays, the contribution of secondary gamma rays is not expected to dominate. However, for larger distances, the primary gamma-ray component is filtered out above a TeV, while the secondary contribution is enhanced. Indeed, the scaling of the primary gamma rays with distance is determined by the losses due to pair production in gamma-ray interactions with extragalactic background light (EBL):

$$F_{\text{primary},\gamma}(d) \propto \frac{1}{d^2} \exp(-d/\lambda_\gamma). \quad (4.1)$$

In contrast, gamma rays generated in line-of-sight interactions of cosmic rays exhibit a very different scaling with distance [53, 51, 52]:

$$\begin{aligned} F_{\text{secondary},\gamma}(d) &\propto \frac{\lambda_\gamma}{d^2} (1 - e^{-d/\lambda_\gamma}) \\ &\sim \begin{cases} 1/d, & \text{for } d \ll \lambda_\gamma, \\ 1/d^2, & \text{for } d \gg \lambda_\gamma. \end{cases} \end{aligned} \quad (4.2)$$

Here λ_γ is the distance at which EBL opacity to TeV gamma rays is of the order of 1. The lack of suppression is due to the fact that the photon backgrounds (CMB and EBL) act as a target on which gamma rays are produced by the cosmic rays. Hence, a higher

column density of background photons for a more distant source boosts, not hinders the gamma-ray production.

As long as IGMFs are weak enough to cause only small deflections, for a sufficiently distant source, secondary gamma rays dominate because they don't suffer from exponential suppression as in Eq. (4.1), which is absent from Eq. (4.2). The transition from primary to secondary photons occurs when the optical depth to pair production exceeds 1. The corresponding redshift can also be inferred from the spectral softening of the spectra [74]. Based on these estimates, one can expect the secondary gamma rays to dominate for sources at redshifts $z \gtrsim 0.15$.

The success of the spectral fits to the data for secondary gamma rays [53, 51, 52] can be interpreted as possible evidence of cosmic ray acceleration in blazars. Within this interpretation, the beamed energy output in $E > 10^{17}$ eV cosmic rays required to fit the observed spectra of distant blazars is of the order of 10^{43} erg, or 10^{45} erg isotropic equivalent [53, 51, 52], which is consistent with many models [32]. The luminosity required to explain ultrahigh-energy cosmic rays (UHECR) depends on the assumed spectrum, which is often parameterized by a broken power law with a break at some value E_c (unknown a priori). According to [32], the AGN luminosities in cosmic-ray protons needed to account for the UHECR data are 5.6×10^{43} erg/s, 2.5×10^{44} erg/s, and 1.1×10^{45} erg/s, for $E_c = 10^{18}$ eV, $E_c = 10^{17}$ eV, and $E_c = 10^{16}$ eV, respectively. These estimates are in general agreement with our results. We also note that, because of the selection effects, the sources observed from large distances are by no means average: they are the brightest AGNs, which generate exceptional power in cosmic rays.

The spectra of observed gamma rays generated in this fashion depend on the intervening intergalactic magnetic fields. It is easy to understand some qualitative features of this dependence in terms of a simplified random-walk description of the proton propagation. Let us consider a short pulse of protons emitted from a source at distance d . At later times, the proton pulse broadens and takes the shape $f(t, r)$. The explicit form of $f(t, r)$ was computed by [17] and will be discussed below. (See also [67]; [87].)

At every point in its trajectory, the proton interactions with the cosmic background generate a flux of gamma rays, which quickly (on a kpc length scale) cascade down to energies below the threshold. From that point on, gamma rays travel without further time delays. However, during the cascade development, the IGMFs cause some delays (which are longer than the delays of the protons in the IGMFs for E_γ below 10 TeV).

Let us consider the proton propagation in IGMFs. We assume that IGMFs form a lattice with correlation length l_c , in which a proton with energy $E_p = 10^{17}$ eV random-walks over a distance $d \sim 1000 \text{ Mpc} = n \times l_c$, where $n \sim 10^3$.

The angle between the proton momentum and the line of sight performs a two-

dimensional random walk in small steps of $\sim 10^{-6}$. When the proton interacts with a background photon, it emits a narrow shower in the direction of the proton's momentum. The prompt gamma rays are emitted into a narrow angle $(\sim E_p/\text{MeV})^{-1}$ for Bethe–Heitler pair production, or $(\sim E_p/0.2\text{ GeV})^{-1}$ for pion photoproduction. The cascade develops and broadens this angle, with larger angles at lower energies. To shower in the direction of observer after n steps of random walk, the proton angle should return to 0. For a 2D random walk, the probability of *not* returning to zero after n steps is $\gamma_2(n) = \frac{\pi}{\ln n} + O\left(\frac{1}{(\ln n)^2}\right)$. This probability drops below 1/2 for $n > \exp(2\pi) \sim 5 \times 10^2$. For $d \sim 1000\text{ Mpc}$, $n \sim 10^3$, and so each proton angle returns to the origin about ~ 1 time per distance traveled. Therefore, the diffusion approximation is justified, and a “typical” delay can be computed using the distance traveled, assuming the random walk.

Deflection of a proton in a single cell is θ_0 . This deflection and the time delay are determined by the Larmor radius

$$R_B = \frac{E}{eB} = 10^5 \text{Mpc } E_{p,17}/B_{-15},$$

where $E_{p,17}$ is the proton energy in units of 10^{17} eV , and B_{-15} is the value of the magnetic field in femtogauss.

Therefore,

$$\theta_0 = \frac{l_c}{R_B} = 10^{-5} \left(\frac{l_c}{\text{Mpc}} \right) B_{-15}/E_{p,17}.$$

Time delay in crossing a single cell is

$$\Delta t_0 = \frac{l_c}{c} \theta_0^2 = 10^4 \text{s} \left(\frac{B_{-15}}{E_{p,17}} \right)^2.$$

After $n \sim 10^3$ steps of random walk, the time delay is

$$\tau_p = n \Delta t_0 \sim 10^7 \text{s} \left(\frac{B_{-15}}{E_{p,17}} \right)^2. \quad (4.3)$$

Significant time delays are also incurred in the EM showering process. Each observed gamma ray was at some point an electron in the cascade. The time delay of each gamma ray with an observed energy E_γ is dominated by the delay during the lowest-energy “electron” phase of this gamma ray. The electron energy is related to the energy of observed IC γ ray by $E_\gamma \propto E_e^2$. IGMFs act on the electron over a distance of the order of its cooling distance $D_e \propto 1/E_e$. The time delay incurred in this process is proportionate to the sum [88, 89] of D_e and the mean free path to pair production λ_{pp} ,

which has the same energy dependence (with a much larger prefactor), $\lambda_{\text{PP}} \propto 1/E_e$. The resulting delay is

$$\tau_e = (\lambda_{\text{PP}} + D_e)\theta_e^2/c, \text{ where } \theta = D_e \frac{eB}{E_e}.$$

Therefore,

$$\tau_\gamma \approx \tau_e = D_e^2(\lambda_{\text{PP}} + D_e) \frac{e^2 B^2}{c E_e^2} \propto \frac{B^2}{E_e^5} \propto \frac{B^2}{E_\gamma^{5/2}} \quad (4.4)$$

where we have assumed $D_e \sim \text{kpc} \ll l_c$.

The proton delay (4.3) is

$$\tau_p \propto \frac{B^2}{E_p^2}. \quad (4.5)$$

The total time delay of an observed photon is the sum of τ_p and τ_γ :

$$\tau_{\text{tot}} = \tau_p + \tau_\gamma = C_1 \frac{B^2}{E_p^2} + C_2 \frac{B^2}{E_\gamma^{5/2}}, \quad (4.6)$$

where C_1 and C_2 are some constants.

One can, therefore, expect the following structure of time delays. The shortest delay time is determined by the delay in the arrival of the highest-energy proton; this time delay is given by Eq. (4.5). High-energy protons travel faster than the gamma-ray cascades, and they are followed by a tail of trailing gamma rays. There are two contributions to the total delay time, which have a different dependence on energy (4.6). As the second term in Eq. (4.6) diminishes with energy, the time delay approaches a plateau independent of the photon energy. The height of this plateau is determined by the energy of the proton. This agrees with the results of numerical calculations presented in Figure 4.2.

4.3 Semi-analytical description

Let us consider the time delays due to the propagation of protons. Protons interactions with extragalactic background radiation (both CMB and EBL) occur with a very low probability for energies below the pion production threshold. In the pair production process, a proton loses only $\sim 10^{-3}$ of its energy in each collision. Thus, one can neglect the energy losses for protons in making some basic estimates. (However, in our numerical calculations, we take into account all the energy losses, including adiabatic losses.) Also, the deflection angles can be assumed small for the relevant range of parameters. Calculation of the electromagnetic cascade initiated by the secondary gamma

rays produced in proton-photon interactions is much more difficult, and there is no simple analytical approach that could allow one to calculate the distribution function of gamma rays. Therefore we will employ a hybrid approach by combining an analytical treatment of protons with a Monte Carlo simulation for the electromagnetic cascade.

To calculate the distribution function of protons, let us consider a mono-energetic beam of protons emitted with energy E at some point in time. Random deflections in weak IGMFs result in arrival time distribution which is convenient to consider as a function of time delay parameter $\tau = t - r/c$, where r is the distance to the source and c is the speed of light. In a small-angle approximation, one can express the distribution function as follows [17]:

$$f_A(E, \tau, r) = \frac{1}{\tau} \left(\frac{c\tau}{r^2 \langle \theta_s^2 \rangle} \tilde{f}_A \left(\frac{c\tau}{r^2 \langle \theta_s^2 \rangle} \right) \right), \quad (4.7)$$

where

$$\tilde{f}_A(y) = 4\pi^2 \sum_{n=1}^{\infty} (-1)^{n-1} n^2 e^{-2\pi^2 n^2 y} \quad (4.8)$$

$$\langle \theta_s^2 \rangle = \frac{l_c}{5} \left(\frac{e}{E} \right)^2 \langle B^2 \rangle. \quad (4.9)$$

Here $\langle \theta_s^2 \rangle$ is the mean square deflection angle per unit length. The correlation length l_c and the mean square of magnetic field $\langle B^2 \rangle$ enter in Eq. (4.7) as parameters. The normalization of the function f_A is so that $\int_0^{\infty} f_A d\tau = 1$. Then the distribution function of protons injected with energy spectrum $J_p(E)$ at the distance r from the source is

$$f_p(E, \tau, r) = \frac{J_p(E) f_A(E, \tau, r)}{r^2}. \quad (4.10)$$

Let protons interact with low energy photon field $f_{ph}(\epsilon)$. The protons with a monoenergetic distribution (normalized to one particle) produce electron-positron pairs at the rate $\Phi(E_e, E_p)$, where E_p is the energy of protons, E_e is the energy of pairs. Following [31], one can express $\Phi(E_e, E_p)$ as follows:

$$\Phi(E_e, E_p) = c^2 \int d\epsilon \frac{d\Omega}{4\pi} f_{ph}(\epsilon) \frac{k \cdot u_p}{\epsilon \gamma_p} \int \delta(E_e - c(u_{lf} \cdot p_e)) d\sigma, \quad (4.11)$$

where k , u_p , and u_{lf} are four-velocities of photon, proton, and the laboratory frame, respectively; and p_e is four-momentum of electron (or positron). γ_e and ϵ are the proton Lorentz factor and the energy of photon in the laboratory frame. $d\sigma$ is the Bethe-Heitler cross section. The photon field used in this calculations includes the CMB and EBL, and one can neglect the redshift evolution.

Then distribution function of electrons produced at the distance r with inherited time delay τ is

$$f_e(E_e, \tau, r) = \int dE_p \frac{J_p(E_p) f_A(E_p, \tau, r)}{r^2} \Phi(E_e, E_p). \quad (4.12)$$

These electrons initiate an electromagnetic cascade. Let $f_{cas}(E_e, E_\gamma, s)$ be the number of photons with energy E_γ produced in the cascade initiated by an electron with energy E_e at the distance s from the observer and detected at the point of observation. The mean time delay of the photons is $\tau_{cas}(E_e, E_\gamma, s)$. The extragalactic magnetic field is a parameter. Then for the UHE proton source at the distance d the number of photons produced in the cascade with time delay $\tau = \tau_{cas} + \tau_{prot}$ is

$$f_\gamma(E_\gamma, \tau, d) = \int_0^d dr \int dE_e f_e(E_e, \tau - \tau_{cas}(E_e, E_\gamma, r), d - r) f_{cas}(E_e, E_\gamma, r) \quad (4.13)$$

The Eqs. (4.7), (4.12) and (4.13) constitute the integral which is calculated numerically. The functions f_{cas} and τ_{cas} actually depend on redshift but not on distance, therefore we use the relation

$$dr = \frac{c}{H_0} \frac{1}{(1+z)\sqrt{(1+z)^3\Omega_m + \Omega_\Lambda}} dz, \quad (4.14)$$

to express distance via redshift and perform integration over z .

We assume that the source produces a power-law spectrum of protons with a spectral index α and the energy range from $0.1E_0$ to E_0 . The results for the mean time delay of gamma rays are presented in Figs. 4.2 and 4.3 as a function of the varying cut-off energy, distance to the source and spectral index. In these calculations we assumed that the intergalactic magnetic field has the strength $B = 10^{-15}$ G and the coherence length $l_c = 1$ Mpc. Unless specified otherwise, we use $E_0 = 10^{17}$ eV, $\alpha = 2$.

The advantage of the analytical description presented above is the possibility to study the time delay distribution of gamma rays for a variety of initial proton spectrum parameters. The numerical Monte Carlo approach described below has computational limitations on the number of initial particles, which can complicate the study of how a proton spectrum with a wide energy range can affect the time delays of gamma rays. The protons injected with slightly different energies would have the time distribution which is similar to the time distribution for a monoenergetic proton beam. In contrast, the time distribution of protons with a broad energy spectrum is a sum of time distributions of protons with different energies, which is stretched out in time. This would spread the arrival times of gamma rays along a large time span. The illustration of this effect can be seen from the comparison of the second panel of Fig. 4.4 and Fig. 4.5.

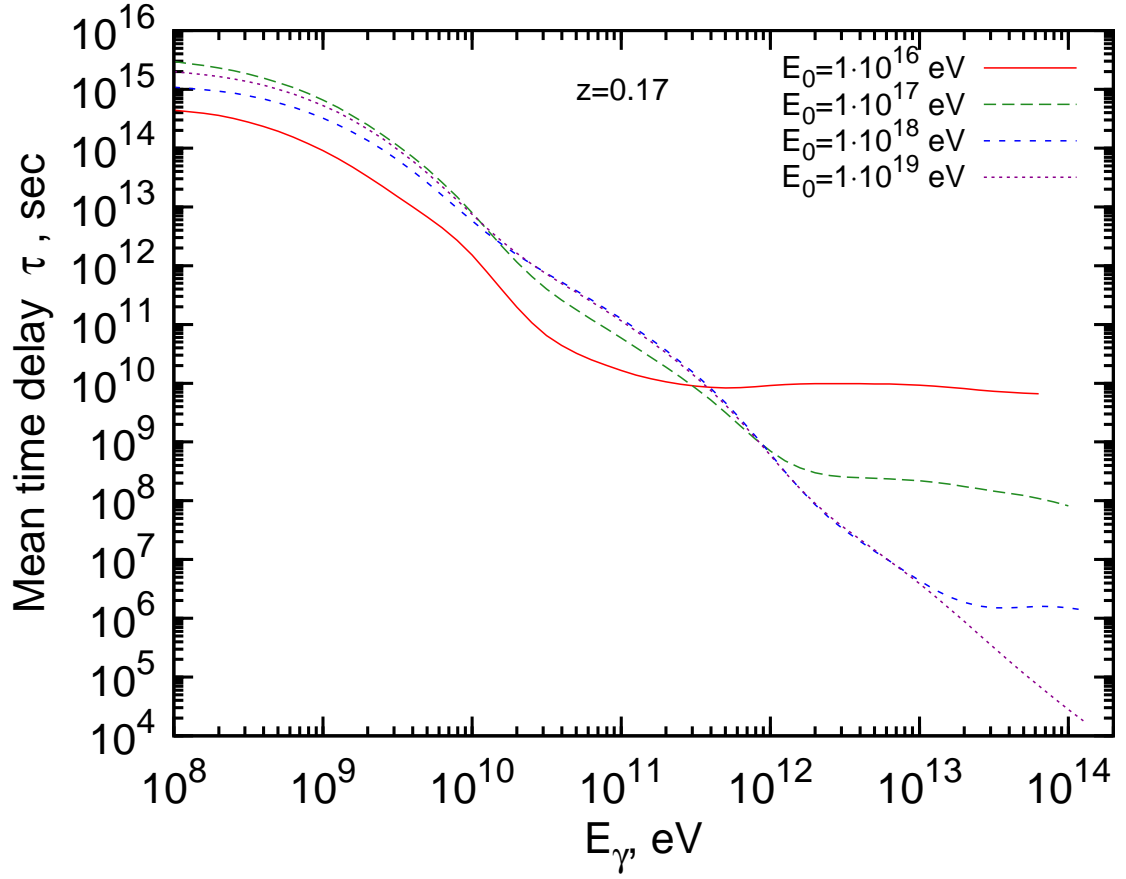


Figure 4.2: Mean time delay of gamma rays at redshift $z = 0.17$ for different cutoff energies E_0 of proton spectrum.

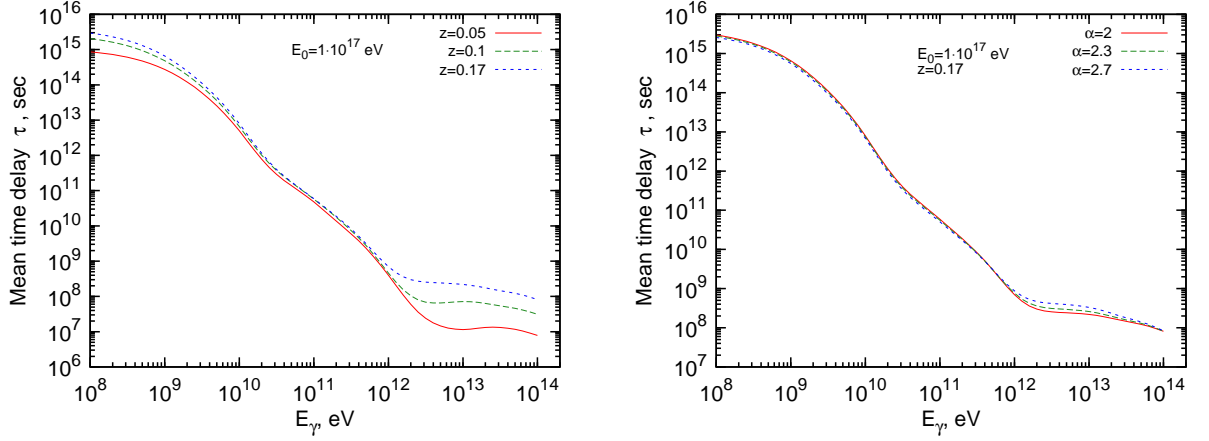


Figure 4.3: Left panel: mean time delay of gamma rays for the sources at different redshifts and the proton spectrum with cutoff energy $E_0 = 10^{17}$ eV. Right panel: mean time delay of gamma rays for the source at $z = 0.17$ and the proton spectrum with cutoff energy $E_0 = 10^{17}$ eV and different spectral indices α .

The range of the proton energies has a strong effect on the lower energy gamma rays, whereas the time distribution for $E_\gamma = 1 \cdot 10^{14}$ eV does not change significantly. This is because, in the case of a broad spectrum, protons with different energies can contribute gamma rays of a given energy. On the other hand, only the protons of highest energies are responsible for the production of gamma rays of $E_\gamma = 1 \cdot 10^{14}$ eV. Therefore, the corresponding time distribution is similar to the one for the monoenergetic protons (*cf.* Fig. 4.6).

The flux of gamma rays arriving at any given time comprises contributions from protons at different points along the line of sight. We obtain this flux by integrating over the proton distributions shifted by a time delay incurred in the electromagnetic cascade. The latter delays were obtained from numerical calculations using a single Monte Carlo numerical run. The results are shown in Figs. 4.4 and Fig. 4.5. The multiple-peak structure apparent in these curves is the result of adding contributions from different distances with the delay profile obtained from a single numerical run. If we adopted a different approach and used an averaged delay profile, as in Fig. 4.7, the “many-peak” structure would be erased.

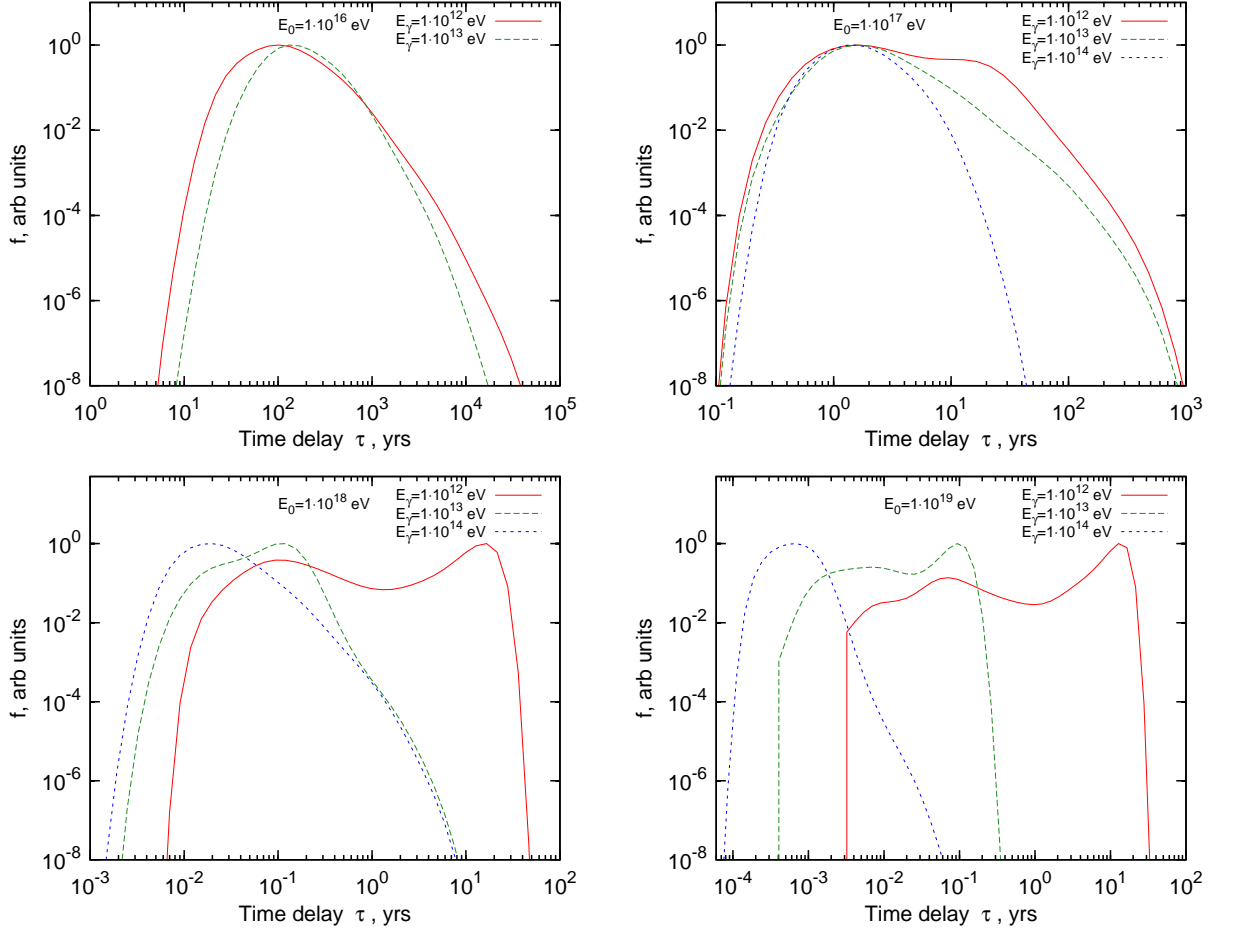


Figure 4.4: Time delay distribution of gamma rays in arbitrary units (the maximum of distribution is normalized to unity) at different energies from the source at $z = 0.17$. Each plot corresponds to the proton spectrum with different cutoff energy E_0 and spectral index $\alpha = 2$. The injected spectra of protons are taken in the range from $0.1E_0$ to E_0 .

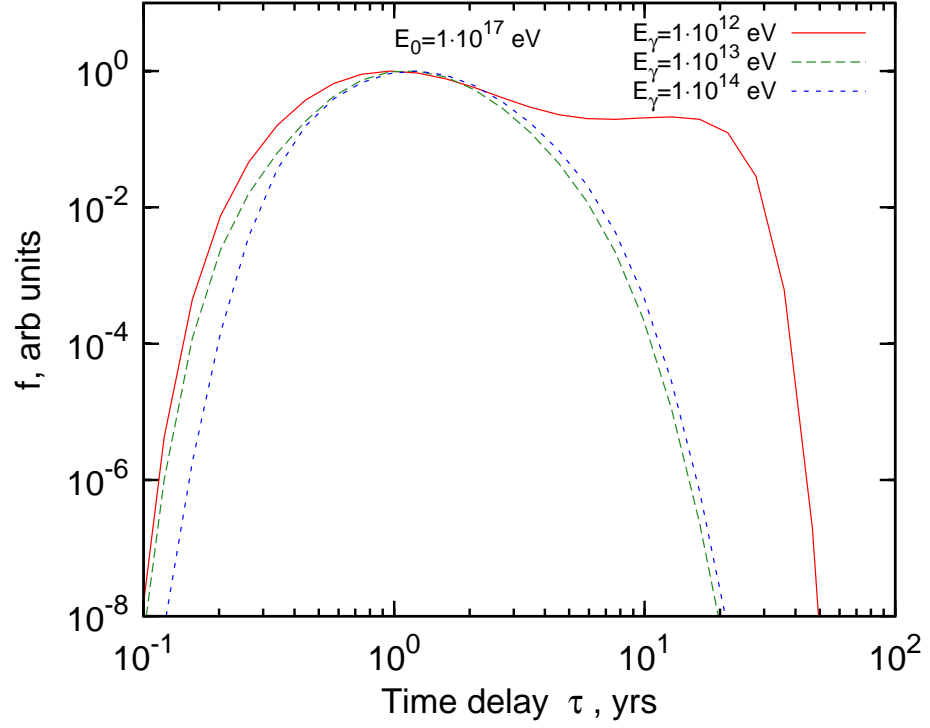


Figure 4.5: Time delay distribution of gamma-ray in arbitrary units (the maximum of distribution is normalized to unity) from the source at $z = 0.17$. The injected spectrum of protons is almost monoenergetic with energy $E = 10^{17}$ eV.

4.4 Numerical Monte-Carlo calculations

In addition to the semi-analytical results we also performed a full scale Monte Carlo simulation to track the arrival times of individual particles. The source was modeled by an instantaneous pulse of protons to represent the Green's function needed to calculate the distribution of arrival times. Particles are advanced in time steps of roughly 0.1 – 1 kpc, updating momentum, position and time delay with all relevant interactions taken into account. Gamma rays arriving at the $z = 0$ surface are binned and the mean arrival time and standard deviation are calculated.

The proton energy loss processes are well studied [90] and can be described by a standard approach. We calculate all the relevant energy losses, including adiabatic losses and the losses due to the interactions with photon backgrounds. The most important contributions to secondary photon production are photopion production and proton pair production (PPP).

The photopion production processes involve the following reactions:



where γ_b is either a CMB or EBL photon. PPP occurs in the reaction



The pair production on the CMB is the dominant reaction, but pion photoproduction on EBL also contributes. Pion photoproduction on CMB has a threshold above 10^{19} eV, but pion production on EBL is possible for all energies we consider. The efficiency of energy transfer to the electromagnetic shower depends on the proton energy and on the distance to the source. A more detailed discussion is presented elsewhere [54].

The mean interaction length, λ , for a proton of energy E traveling through a photon field is given by

$$[\lambda[E]]^{-1} = \frac{1}{8\beta E^2} \int_{\epsilon_{\min}}^{\infty} \frac{n(\epsilon)}{\epsilon^2} \int_{s_{\min}}^{s_{\max}(\epsilon, E)} \sigma(s)(s - m_p^2) ds d\epsilon, \quad (4.17)$$

where $n(\epsilon)$ is the differential photon number density of photons of energy ϵ , and $\sigma(s)$ is the appropriate total cross section for the given process for the center of momentum (CM) frame energy squared, s , given by

$$s = m_p^2 + 2\epsilon E(1 - \beta \cos \theta), \quad (4.18)$$

where θ is the angle between the proton and photon, and β is the proton's velocity.

For pion photoproduction,

$$s_{\min} = (m_p^2 + m_\pi^2)^2 \quad (4.19)$$

and

$$\epsilon_{\min} = \frac{m_\pi(m_\pi + 2m_p)}{2E(1 + \beta)}. \quad (4.20)$$

For proton pair production

$$s_{\min} = (m_p^2 + 2m_e^2)^2 \quad (4.21)$$

and

$$\epsilon_{\min} \approx \frac{m_e(m_e + m_p)}{E}. \quad (4.22)$$

For both processes,

$$s_{\max}(\epsilon, E) = m_p^2 + 2\epsilon E(1 + \beta). \quad (4.23)$$

Both pions and neutrons quickly decay via the processes

$$\begin{aligned} n &\rightarrow p + e^- + \bar{\nu}_e, \\ \pi^+ &\rightarrow \mu^+ + \nu_\mu \rightarrow e^+ + \nu_e + \bar{\nu}_\mu + \nu_\mu, \\ \pi^0 &\rightarrow 2\gamma. \end{aligned} \quad (4.24)$$

The outgoing distribution functions for pion photoproduction were generated using the SOPHIA package [33].

Primary gamma rays and gamma rays produced from the above equations can interact and pair-produce on background photons. The resulting electron positron pairs will IC scatter CMB photons. The upscattered photons can once again pair produce, this chain reaction is known as electromagnetic (EM) showering.

The interaction length for photons for pair production off the EBL is

$$[\lambda]^{-1} = \left(\frac{m_e^2}{E}\right)^2 \int_{\frac{m_e^2}{E}}^{\infty} \epsilon^{-2} n(\epsilon) \int_1^{\frac{\epsilon E}{m_e^2}} 2s\sigma(s) ds d\epsilon, \quad (4.25)$$

where

$$\sigma = \frac{1}{2}\pi \left(\frac{e^2}{m_e^2}\right)^2 (1 - \beta^2) \left[(3 - \beta^4) \ln \frac{1 + \beta}{1 - \beta} - 2\beta(2 - \beta^2) \right] \quad (4.26)$$

and

$$\beta = (1 - 1/s)^{1/2}, \quad (4.27)$$

and $n(\epsilon)$ is the differential photon number density of photons of energy ϵ .

To simulate magnetic field effects, the IGMF is modeled by cubic cells of a given

magnetic field strength with sides equal to the chosen correlation length, l_c , and a random direction. Particles are moved forward in fine time steps and the deflection of the particle is calculated using the Larmor radius and IGMF direction. Time delays for charged particles are calculated in comparison to a photon traveling in a straight line to the observer.

For the analysis of time delays, we have performed multiple runs and averaged the results, as shown in Fig. 4.7.

The results of the simulation are shown in Fig. 4.8, where delays from deflections in the IGMF are shown for a source at $z = 0.2$. It is evident that secondary photons produced at large distances conform to the power-law behavior as in Eq. (4.4). This approximate power law is illustrated in Fig. 4.8 by a dashed line. The flattening at low energies can be understood by the way the code handles deflections. Particles are moved forward in time steps of roughly $0.1 - 1$ kpc and deflections are assumed to be less than π within a single time step. For the lowest energies this is not always true and the code will underestimate the deflection, thus producing time delays below the power law.

4.5 Discussion

The main qualitative features of the Green's function computed numerically and shown in Fig. 4.2 and Fig. 4.8 can be easily understood. For lower energies (below TeV), time delays $\tau \propto B^2 E^{-5/2} d$, where d is distance to the source. The nearby showers arrive before distant showers, so that the late arriving gamma rays have lower energies and longer delays. The plateau that develops at $E > 1$ TeV is due to the prompt showers emitted by the protons nearby, for which the time delays are determined by the proton deflections in IGMFs. In the absence of cosmic rays, the spectrum would drop above 1 TeV, and the multi-TeV gamma rays would not be observed.

For sub-TeV secondary gamma rays the electromagnetic cascade delays are always longer than the proton delays, and the arrival photons peak at the time given by Eq. (4.4). At energies above TeV, the proton delays come to dominate, in accordance with the broken power law in Eq. (4.6). The numerical results differ somewhat from the scaling in Eq. (4.6). In particular, at low energies, the delays appear to scale as E^{-2} rather than $E^{-2.5}$. The difference can be explained by a combination of several effects. For electron energies below 30 GeV, the cooling distance exceeds the magnetic field correlation length, which we assumed to be $l_c \sim 1$ Mpc. This changes the energy dependence in Eq. (4.4) because the energy-dependent cooling distance must be replaced by the constant correlation length. Furthermore, integration over energies in the cascade affects the power-law behavior. For these reasons, our basic estimates in section 2 were

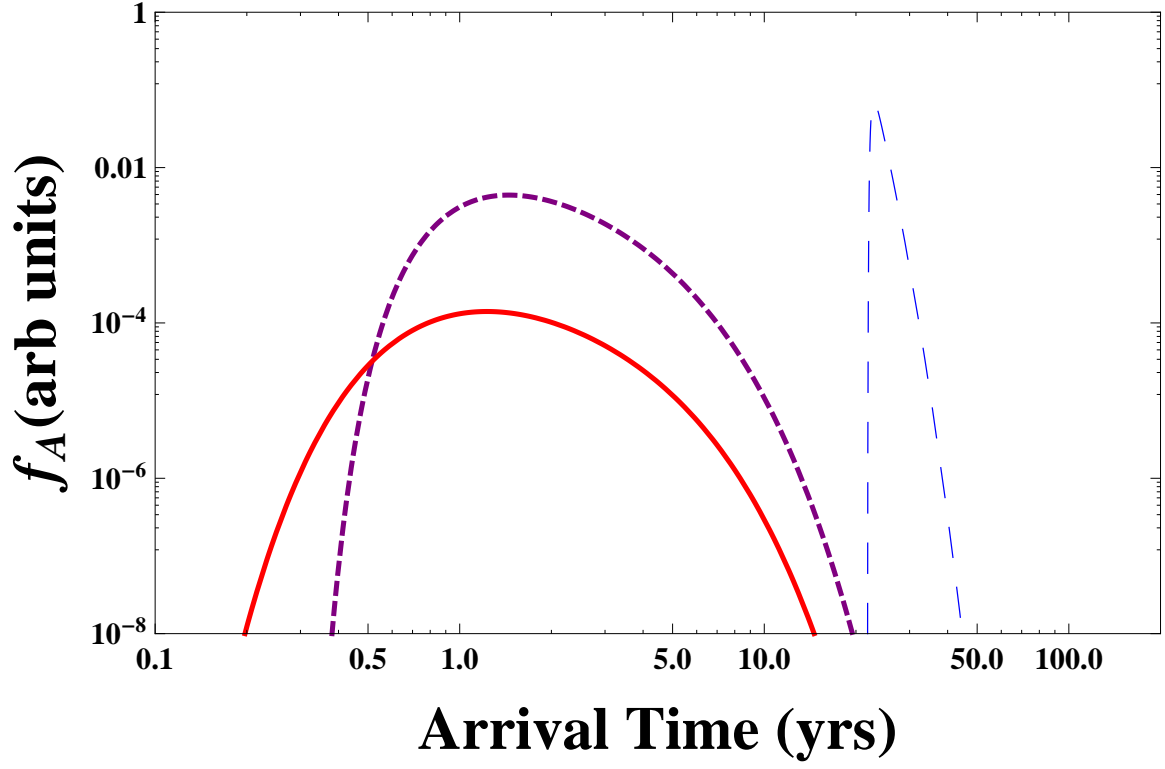


Figure 4.6: Arrival time probability distribution in arbitrary units for secondary gamma rays with energies 1 TeV (blue, long-dashed line), 10 TeV (purple, short-dashed line) and 100 TeV (red, solid line). Results are shown for a cosmic ray source at $z = 0.2$ with a high energy cutoff of 10^8 GeV and an IGMF of 10^{-15} G.

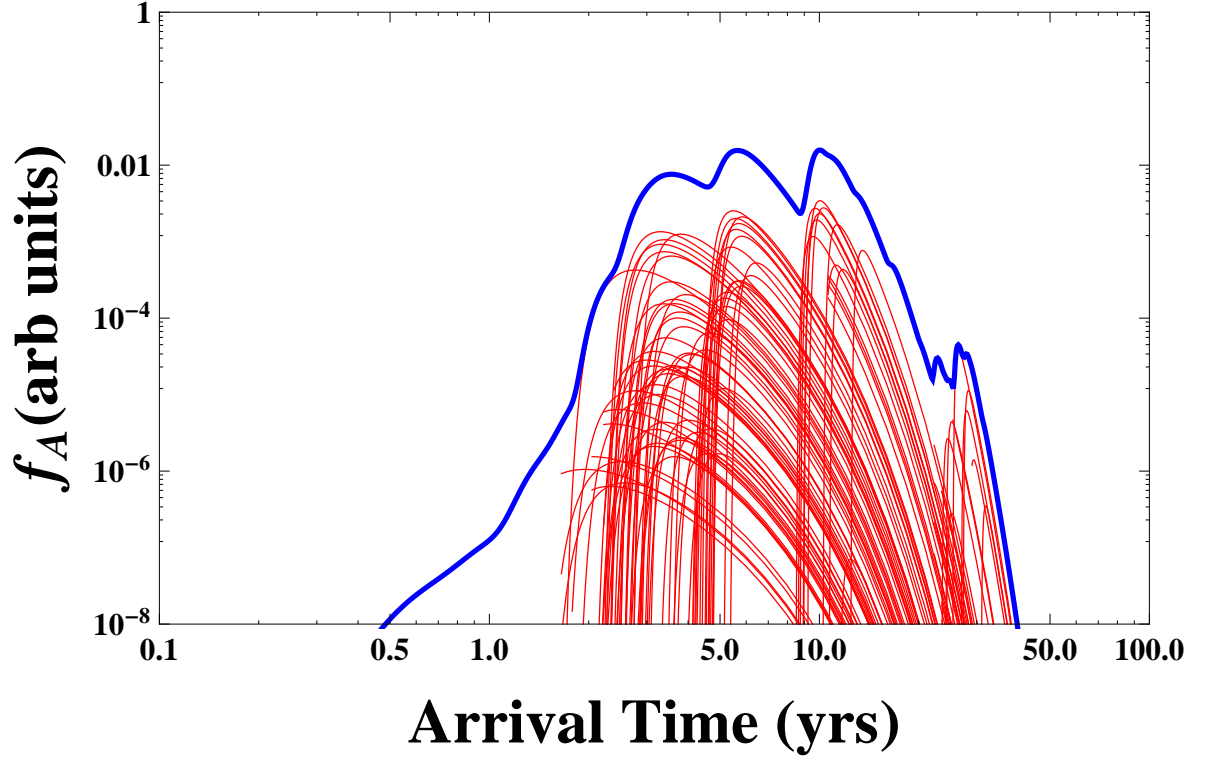


Figure 4.7: Arrival time probability distribution in arbitrary units for 1 TeV secondary photons for multiple numerical runs. The results shown are for roughly 300,000 secondary photons with an IGMF of 10^{-15} G and UHECR cutoff of 10^{10} GeV. The blue thick line represents the sum of all distributions and the thin red lines are a representative set of distributions.

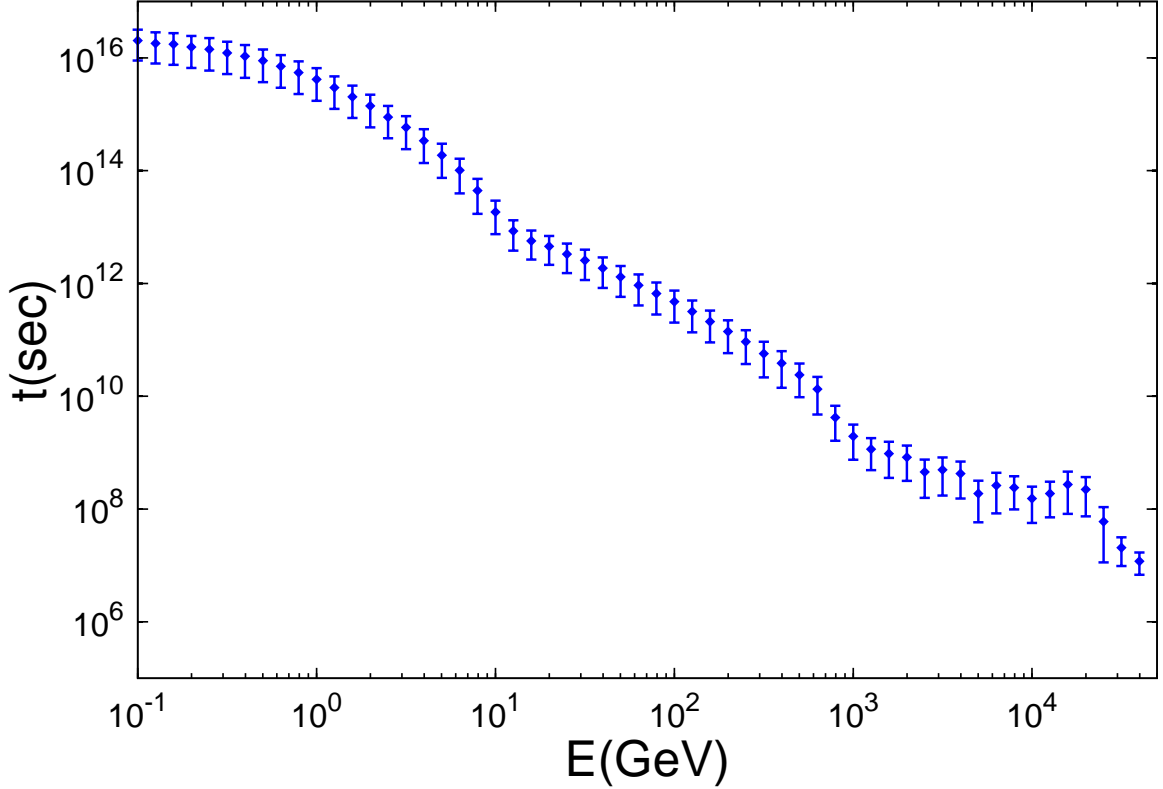


Figure 4.8: Arrival time delays from an instantaneous pulse emitted by a source at $z = 0.2$, assuming $B = 10^{-15}$ G with $l_c = 1$ Mpc correlation length.

not expected to capture all the features evident in the numerical results.

The proton delay is strongly dependent on the high energy cutoff of the cosmic ray source, which affects the energy at which the proton delays begin to dominate. This can be seen in Fig. 4.9. This behavior is further illustrated in Fig. 4.4 and Fig. 4.6, where one can see that the proton delays begin to dominate at $E \sim 10$ TeV for a proton high energy cutoff of 10^8 GeV and an IGMF $= 10^{-15}$ G.

The distribution of gamma-ray arrival times depends on the injection spectrum of protons, as one can see from a comparison of Fig. 4.4 and Fig. 4.5. This is in contrast with the *spectra* of gamma rays, which are *not* sensitive to the proton injection spectrum [51, 52]. Hence, one can, at least in principle, learn about the proton injection spectrum from timing observations, but not from the spectra alone. (Neutrino spectra also depend on the proton injection spectrum [51].) Furthermore, stochastic broadening illustrated in Fig. 4.7 also affects the predictions.

Based on our results, the observed time variability should be washed out on time

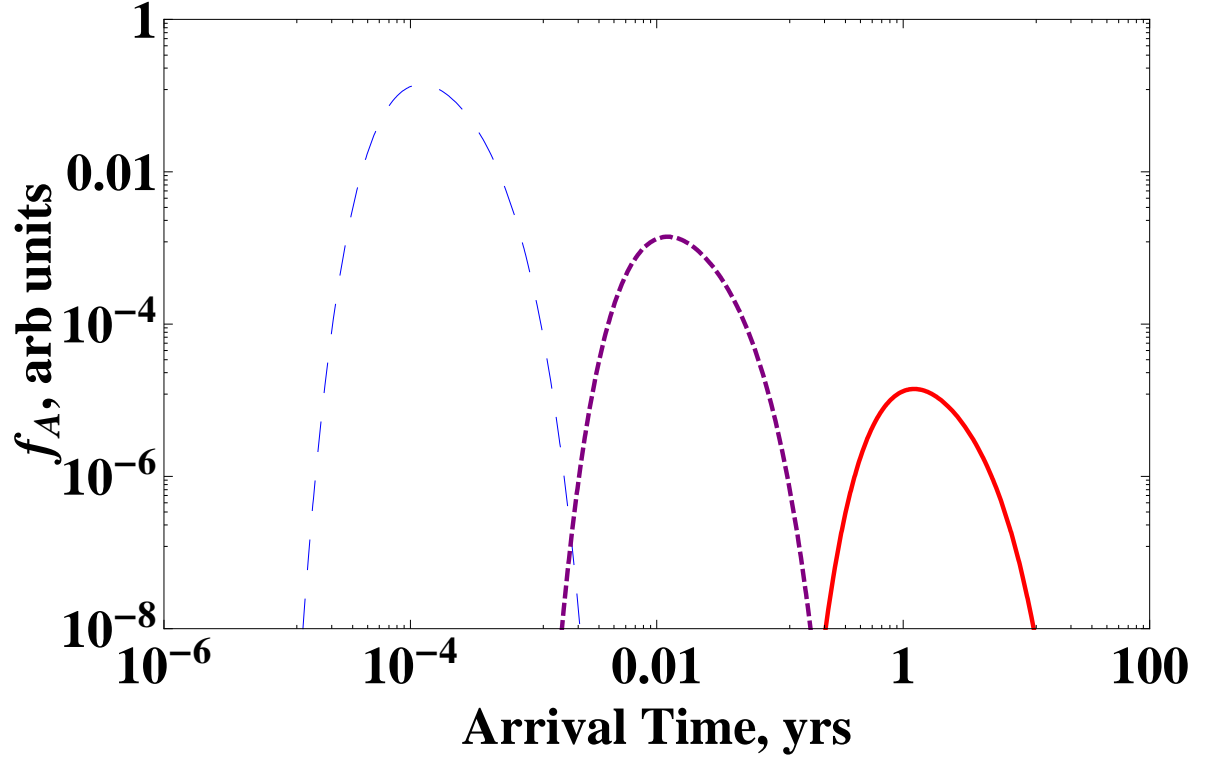


Figure 4.9: Arrival time probability distribution in arbitrary units for primary cosmic rays. Results are shown for a cosmic ray source at $z = 0.2$ with a high energy cutoff of 10^{10} GeV (blue, long dashed), 10^9 GeV (purple, short dashed) and 10^8 GeV (red, solid) and an IGMF of 10^{-15} G.

scales shorter than ~ 0.1 yr, for distant blazars ($z > 0.2$), at TeV and higher energies. Time variability can be present for $z > 0.2$, $E > 1$ TeV on the time scales of $0.1 - 1$ yr. If gamma rays with $E \sim 10^2$ TeV are observed, they can exhibit variability on shorter time scales.

Of course, one must also consider the delays the cosmic rays undergo at the source. Blazars are known to be highly variable, and this variability could affect the shape of the observed spectrum. The magnetic fields within galaxies are on the order of $1 \mu G$ which can lead to significant delays in the source. On the other hand, the structure of magnetic fields in front of the blazar jets is not known. Furthermore, the effect of the source variability would be to suppress the observed power of the source by a factor

$$f_{\text{damp}} \sim N_{\text{active}} \left(\frac{t_{\text{active}}}{t_{\text{delay}}} \right), \quad (4.28)$$

where t_{delay} is the typical proton delay at the source, t_{active} is the typical time the source is active or flaring and N_{active} is the number of times the source is active in the time period t_{delay} . This damping should not be a significant effect [91], especially since the typical deflections at the source are not big enough to affect the beaming factors assumed in popular models.

An alternative situation is that the magnetic fields within the blazar jet are not randomly distributed, but are, instead, strongly correlated with the direction of the jet. Blazar jets emit an extremely large amount of charged matter and the wind in the direction of the jet can eliminate any random-field configuration that one usually expects in a galaxy. Thus, it is possible that cosmic rays escape the source along the jet with very small time delays, preserving the intrinsic variability of the source. In this case, delays in the intergalactic medium can broaden the intrinsic variability to the energy dependent timescales of these delays.

At energies where the optical depth of the observed gamma rays is below one, we expect the signal to be primary gamma rays, and any variability in this signal is indicative of the source variability. This variability should not depend strongly on the energies of the gamma rays, but rather on the scale of the structure at the source producing the gamma rays.

However, we expect a very different behavior for energies at which primary gamma rays are significantly attenuated by pair production off EBL. In the case of strongly correlated magnetic fields in the jet, we expect that the variability should show different structure in the low energy component, where it should depend on the energy. The spectrum should show variability on shorter timescales for higher energies until some critical energy $E_c \sim \text{TeV}$, where the timescales cease to decrease further, thanks to the

domination of the cosmic ray contribution. In the case of large delays within the source, we expect all variability to be washed out at these higher energies (typically around a TeV for most observed sources).

Some exceptionally bright flares can come through around E_c and rise above the *pedestal* created by the stochastic arrival times of protons. Such flares should have distinctly softer spectra than the hard pedestal, which can be a means of distinguishing these flares from the stochastic pedestal.

For most of discussion, we have assumed that IGMFs have strengths are of the order of a femtogauss. This range is suggested by the spectral fits to the data [85]. However, field strengths well below a femtogauss can be consistent with the data as well. In the case of very weak IGMFs, the time delays become smaller, since $\tau \propto B^2$. For $B \sim 10^{-18}$ G, the time delays can be as short as minutes.

We have also assumed that the strength of IGMF is constant on average, which is a good assumption for propagation in the voids. However, if the line of sight intersects a filament of stronger, *e.g.*, nanogauss magnetic field, the reduction of the secondary photon signal depends on the size of the filament and on its location. Thin filaments can only intercept as small fraction of protons within the 0.1 degree associated with a given source. However, a thick filament or a sheet of strong field can deflect protons, reducing the secondary signal.

Temporal structure of gamma-ray signals can be used to measure the IGMF structure and EBL intensity in different directions, on a source-by-source basis. In addition, it may provide a way to probe the high energy cutoff of cosmic ray sources, as well as the spectrum of EBL. A statistical analysis on multiple bins of data is needed to determine the variability at different energies. This presents challenges at the highest energies because of the low statistics, but longer observation times and the advent of next generation experiments should make this analysis increasingly powerful.

4.6 TeV gamma rays from distant blazars

Recent observations of active galactic nuclei with ground-based gamma-ray detectors show growing evidence of very high energy (VHE) gamma-ray emission from blazars with redshifts well beyond $z = 0.1$. In this chapter we examine the question of whether TeV blazars can be observed from even larger redshifts, $z \geq 1$. Although primary TeV gamma rays produced at the source are absorbed by extragalactic background light (EBL), we will show that it is possible to observe such distant blazars as point sources due to secondary photons generated along the line of sight by cosmic rays accelerated in the source.

To a large extent, the observations of blazars with $z > 0.1$ came as a surprise, in view of the severe absorption of such energetic gamma rays in the EBL. One of the obvious implications of these observations is the unusually hard (for gamma-ray sources) intrinsic gamma-ray spectra. Remarkably, the *observed* energy spectra of these objects in the very high energy band are, in fact, very steep, with photon indices $\Gamma \geq 3.5$. However, after the correction for the expected intergalactic absorption (i.e. multiplying the *observed* spectra to the factor of $\exp[\tau(z, E)]$, where $\tau(z, E)$ is the optical depth of gamma rays of energy E emitted by a source of redshift z), the intrinsic (source) spectra appear to be very hard with a photon index $\Gamma_s \leq 1.5$. Postulating that in standard scenarios the gamma-ray production spectra cannot be harder than $E^{-1.5}$, it was claimed that the EBL must be quite low, based on the observations of blazars H 2356–309 ($z = 0.165$) and 1ES 1101–232 ($z = 0.186$) by the HESS collaboration [92]. The derived upper limits appeared to be rather close to the lower limits on EBL set by the integrated light of resolved galaxies. Recent phenomenological and theoretical studies (e.g., Refs. [69, 93]) also favour the models of EBL which are close to the limit derived from the galaxy counts (for a recent review see Ref. [94]). This implies that further decrease in the level EBL is practically impossible, thus a detection of TeV gamma rays from more distant objects would call for new approaches to explain or avoid the extremely hard intrinsic gamma-ray spectra.

The proposed nonstandard astrophysical scenarios include models with very hard gamma-ray production spectra due to some specific shapes of energy distributions of the parent relativistic electrons – either a power law with a high low-energy cutoff or a narrow, e.g., Maxwellian-type distribution. While the synchrotron-self-Compton (SSC) models allow the hardest possible gamma-ray spectrum with the photon index $\Gamma = 2/3$ [95, 78], the external Compton (EC) models can provide gamma-ray spectrum with $\Gamma = 1$ [78]. Within these models one can explain the gamma-ray emission of the blazar 1ES 229+200 at $z = 0.139$ with the spectrum extending up to several TeV [96] and sub-TeV gamma-ray emission from 3C 279 at $z = 0.536$ [97] ($\Gamma_s \sim 1$). Formally, much harder spectra can be expected in the case of Comptonization of an ultrarelativistic outflow [65], in analogy with the cold electron-positron winds in pulsars [98]. Although it is not clear how the ultrarelativistic MHD outflows could form in active galactic nuclei (AGN) with a bulk motion Lorentz factor $\gamma \sim 10^6$, such a scenario, leading to the Klein-Nishina gamma-ray line-type emission [99], cannot be excluded *ab initio*. Further hardening of the initial (production) gamma-ray spectra can be realized due to the internal $\gamma - \gamma$ absorption inside the source [79, 100]. Under certain conditions, this process may lead to an arbitrary hardening of the original production spectrum of gamma rays.

Thus, the failure of “standard” models to reproduce the extremely hard intrinsic

gamma-ray spectra is likely to be due to the lack of proper treatment of the complexity of nonthermal processes in blazars, rather than a need for new physics. However, the situation is dramatically different in the case of blazars with redshift $z \geq 1$. In this case the drastic increase in the optical depth for gamma rays with energy above several hundred GeV implies severe absorption (optical depth $\tau \gg 1$), which translates into unrealistic energy budget requirements (even after reduction of the intrinsic gamma-ray luminosity by many orders of magnitude due to the Doppler boosting). In this case, more dramatic proposals including violation of Lorentz invariance [101, 102, 103] or "exotic" interactions involving hypothetical axion-like particles [80, 104] are justified. Despite the very different nature of these approaches, their main objective is the same – to avoid severe intergalactic absorption of gamma rays due to photon-photon pair production at interactions with EBL. This feat was accomplished either by means of big modifications in the cross-sections, or by assuming gamma-ray oscillations into some weakly interacting particles during their propagation through the intergalactic magnetic fields (IGMFs), e.g., via the photon mixing with an axion-like particle. Alternatively, the apparent transparency of the intergalactic medium to VHE gamma rays can be increased if the observed TeV radiation from blazars is secondary, i.e., if it is formed in the development of electron-photon cascades in the intergalactic medium initiated by primary gamma rays [65]. This assumption can, indeed, help us to increase the *effective* mean free path of VHE gamma rays, and thus weaken the absorption of gamma rays from nearby blazars, such as Mkn 501 [65, 43]. However, for cosmologically distant objects the effect is almost negligible because the "enhanced" mean free path of gamma rays is still much smaller than the distance to the source.

A modification of this scenario can explain TeV signals from objects beyond $z = 1$ if one assumes that the primary particles initiating the intergalactic cascades are not gamma rays, but protons with energies $10^{17} - 10^{19}$ eV [53, 51, 52, 83, 84, 85, 74, 105]. AGN are a likely source of very high energy cosmic rays [106, 60]. High-energy protons can travel cosmological distances and can effectively generate secondary gamma rays along their trajectories. Secondary gamma rays are produced in interactions of protons with 2.7 K cosmic microwave background radiation (CMBR) and with EBL.

4.7 Rectilinear propagation and deflections

Secondary photons from proton induced cascades point back to the source if the proton deflections are small [60]. Rectilinear propagation of protons is possible along a line of sight which does not cross any galaxies, clusters of galaxies, because their magnetic fields would cause a significant deflection. In addition, IGMFs can cause deflections in

the voids, where the fields can be as low as 10^{-30} G [107, 108, 109, 110], but the analysis of blazar spectra including cosmic rays and secondary photons points to a range from 0.01 to 30 femtogauss [85]. As long as IGMFs are smaller than a femtogauss, they do not affect the point images of blazars. It remains to show that a typical line of sight does not cross a galaxy, cluster, etc. The mean rectilinear propagation length for protons reaching us from a distant source was discussed in Ref. [110]. Given homogeneity of the large-scale structure at large redshifts, this distance can be estimated as the mean free path of a proton in a volume filled with density n of uniformly distributed scatterers, each of which has a size R [110]. A typical distance the proton passes without encountering a scatterer is $L \sim 1/(\pi R^2 n)$. One can estimate this distance for galaxies, clusters, etc., and adopt a constraint based on the minimal distance L_{\min} . Sources at distances much larger than L_{\min} should not be seen as point sources of secondary photons. It turns out that the strongest limit comes from galaxy clusters [110]:

$$L_{\min} \sim 1/(\pi R^2 n) \sim (1 - 5) \times 10^3 \text{Mpc}. \quad (4.29)$$

This distance is large enough for a random source at $z \geq 1$ to be seen with no obstruction by a cluster, or a galaxy [110]. Thus, the protons of relevant energies propagate rectilinearly, assuming the IGMFs are small.

If IGMFs on cosmological distance scales are smaller than 10^{-15} G, the protons propagate almost rectilinearly, and they carry some significant energy into the last, most important for us segment of their trajectory determined by the condition $l \leq \lambda_{\gamma, \text{eff}}$, where $\lambda_{\gamma, \text{eff}}$ is the *effective* mean free path of gamma rays. The secondary electron-positron pairs produced with an average energy of $(m_e/m_p)E_p \sim 10^{15}$ eV initiate electromagnetic electron-photon cascades supported by the inverse Compton (IC) scattering of electrons on CMBR and photon-photon pair production of gamma rays interacting with EBL and CMBR. As long as the magnetic field is as small as is required to avoid the smearing of point sources, the cascade develops with an extremely high efficiency. Therefore, the gamma-ray zone is determined by the condition that $\lambda_{\gamma, \text{eff}}$ be larger (typically, by a factor of 2 or 3) than the gamma-ray absorption mean free path $\lambda_{\gamma\gamma}$ shown in Fig. 4.10.

Our analysis so far (and that of Berezhinsky *et al.* [110]) left out the filaments between the clusters. Their size, volume filling factor, and geometry are uncertain, and observations provide only the upper limits. Models can accommodate a variety of field strengths in these filaments [23, 22, 21]. If nanogauss fields exist in large, numerous filaments, and if the line of sight passes through one or more filaments, the signal strength is reduced, as discussed in Ref. [83].

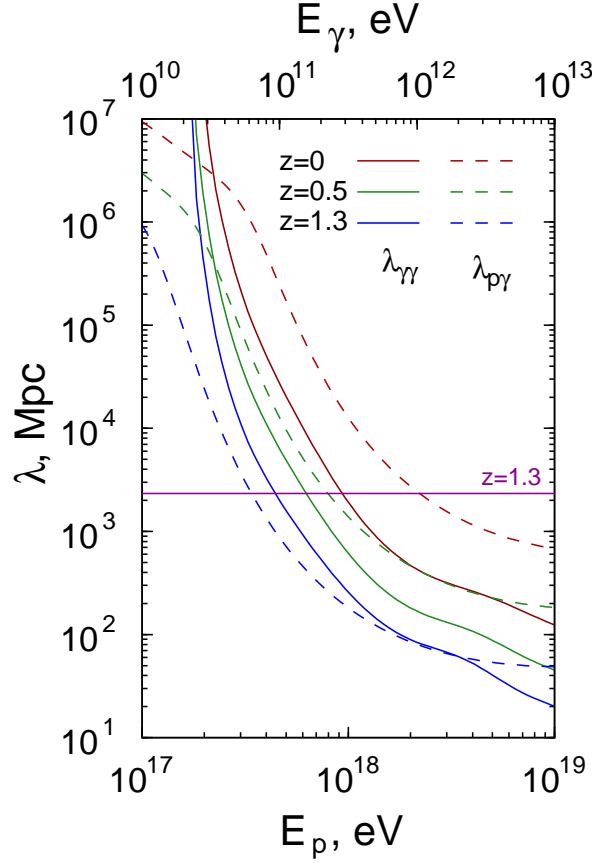


Figure 4.10: The mean free paths of photons and protons as a function of energy and the source redshift. The calculations are based on the formalism developed in Ref. [62]. The gamma-ray absorption mean free path $\lambda_{\gamma\gamma}$ is shown for the EBL model of Ref. [69].

4.8 Energy requirements

The efficiency of this scenario depends on the energy of primary protons and the size of the *gamma-ray transparency zone*. It is approximately determined by the fraction of the proton energy released in e^+e^- pairs inside the gamma-ray transparency zone, at distances less than $\lambda_{\gamma,\text{eff}}$ from the observer. Obviously, in the case of a broad energy distribution of protons, the main contribution to the gamma-ray flux comes from some energy range in which the proton mean free path is comparable to the distance to the source: $d = \lambda_{p\gamma}(E, z = 0)$. In the case of nearby objects with $z \ll 1$, the corresponding energy E^* can be found from Fig. 4.10 as the point where the distance to the source is equal the mean free path of protons at the present epoch, $d = \lambda_{p\gamma}(E^*, z = 0)$. The contributions of protons with lower or higher energies would be significantly smaller. For lower energies, the interaction probability is too small, while, for higher energies, the

energy losses outside the gamma-ray transparency zone are too large. However, in the case of cosmologically distant objects, such a simple argument does not work because of very strong dependency of the proton's mean free path on both the energy and the redshift. It appears that, independent of the initial energy, only the low-energy protons with $E \sim 10^{17}$ eV enter the *gamma-ray transparency zone*. This dramatically reduces the efficiency of production and transport of VHE gamma rays to the observer. At the same time, the efficiencies for gamma rays, the mean free paths of which are comparable to the distance to the source, remain high. This is the case for GeV gamma rays from cosmologically distant, $z \geq 1$, objects and for VHE gamma rays from small- z objects. This can be seen from Fig.4.11, where we show the spectral energy distribution (SED) of gamma rays normalized to the initial energy of the proton. The curves are calculated for two redshifts, $z = 0.2$ and $z = 1.3$, and for several different proton energies.

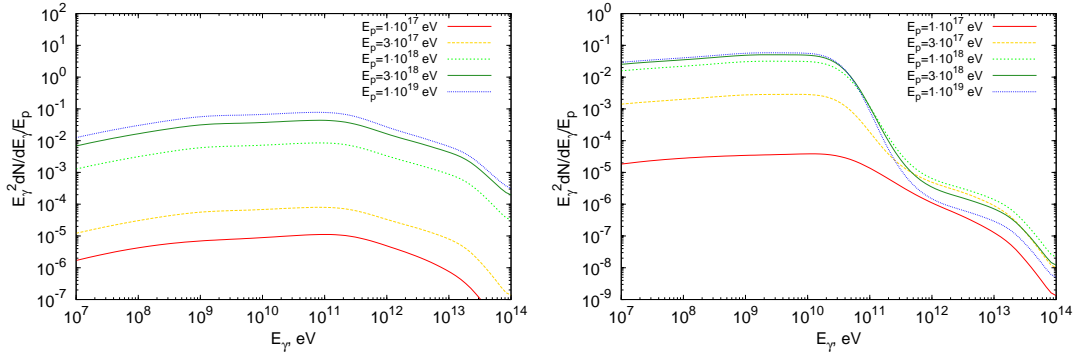


Figure 4.11: The energy spectra of secondary gamma rays produced by protons of different energies emitted from a source at $z = 0.2$ (left panel) and $z = 1.3$ (right panel). The curves are normalized to the proton energy, hence, they show the differential efficiency of the energy transfer from protons to gamma rays. It is assumed that the intergalactic magnetic field $B = 0$.

In Fig. 4.12 we show the dependence of the efficiency of energy transfer on the redshift of the source. It is determined by the character of evolution of radiation fields with z . While the energy density of CMBR monotonically decreases with z , namely $w_{\text{CMBR}} \propto (1+z)^4$, the dependence of the density of EBL on z is more complex and uncertain. For small redshifts, the density of EBL increases with z , but at redshifts corresponding to the epochs before the maximum of the galaxy formation rate ($z \sim 2$), the density of EBL is contributed only by the first stars, therefore it drops at large redshifts. Correspondingly, the probability of gamma rays to reach the observer has a nonlinear dependence on the energy of protons and the source redshift. Depending on the energy of gamma rays, the efficiency reaches its maximum at intermediate redshifts, $z \sim 0.1 - 0.3$. We note

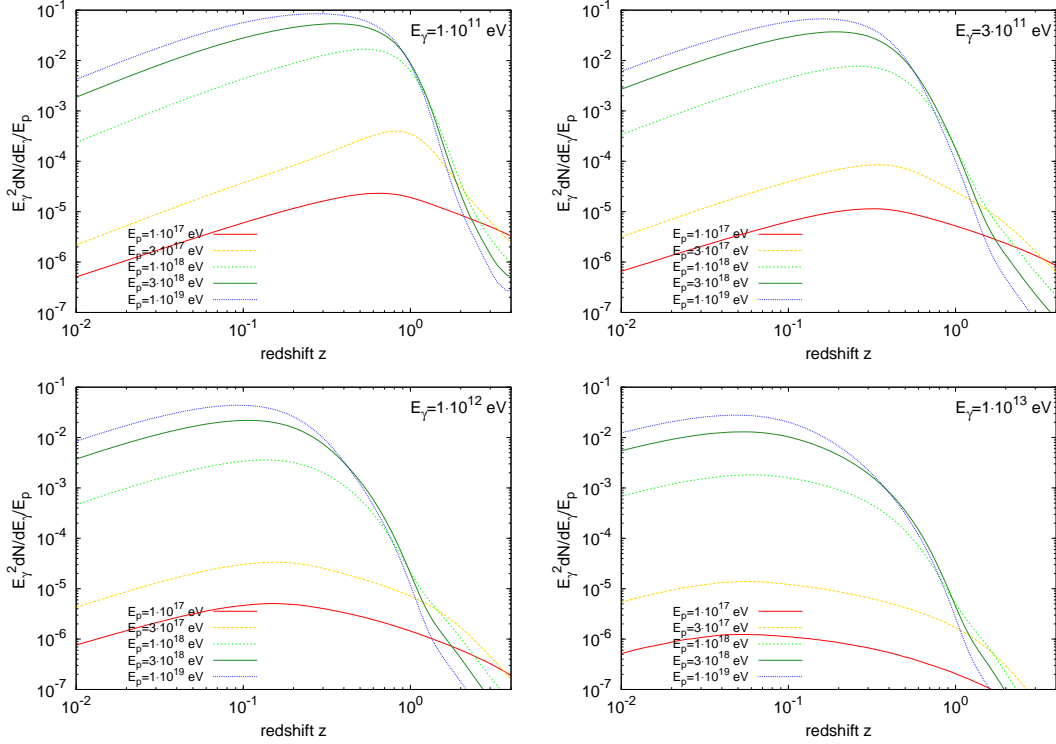


Figure 4.12: The differential efficiency of the energy transfer from protons to gamma rays as a function of the redshift of the cosmic-rays source for different initial energies E_p of the monoenergetic proton beam.

that at $z \sim 0.1$, the efficiency could be rather high (greater than 1%) even at 10 TeV. Therefore, the contribution of this channel to the quiescent component of VHE radiation from nearby blazars can be quite significant. At large redshifts, $z \geq 1$, the efficiency at TeV energies drops dramatically, and it does not exceed 10^{-5} at $z = 1$. Yet, even with such a small efficiency, one can expect TeV gamma rays from sources with $z \sim 1$, provided that the parent protons leave the blazar in a narrow beam. In contrast, TeV gamma rays emitted directly by the source at $z \geq 1$ suffer severe absorption, thus only a negligible fraction can survive and reach the observer.

Indeed, for gamma rays with energy in excess of several hundred GeV arriving from a source at $z = 1$, the optical depth is very large, $\tau_{\gamma\gamma} \sim 10$, for any realistic model of EBL. VHE gamma rays cannot survive the severe intergalactic absorption (see Fig. 4.13). This could be relevant for TeV gamma-ray emission from the blazar PKS 0447-439 [113], given the large redshift of the source $z \geq 1.126$, as claimed in Ref. [114]. However, recently two independent groups [115, 116] challenged the interpretation of the redshift measurements of Ref. [114]. Thus, the redshift of PKS 0447-439 remains uncertain.

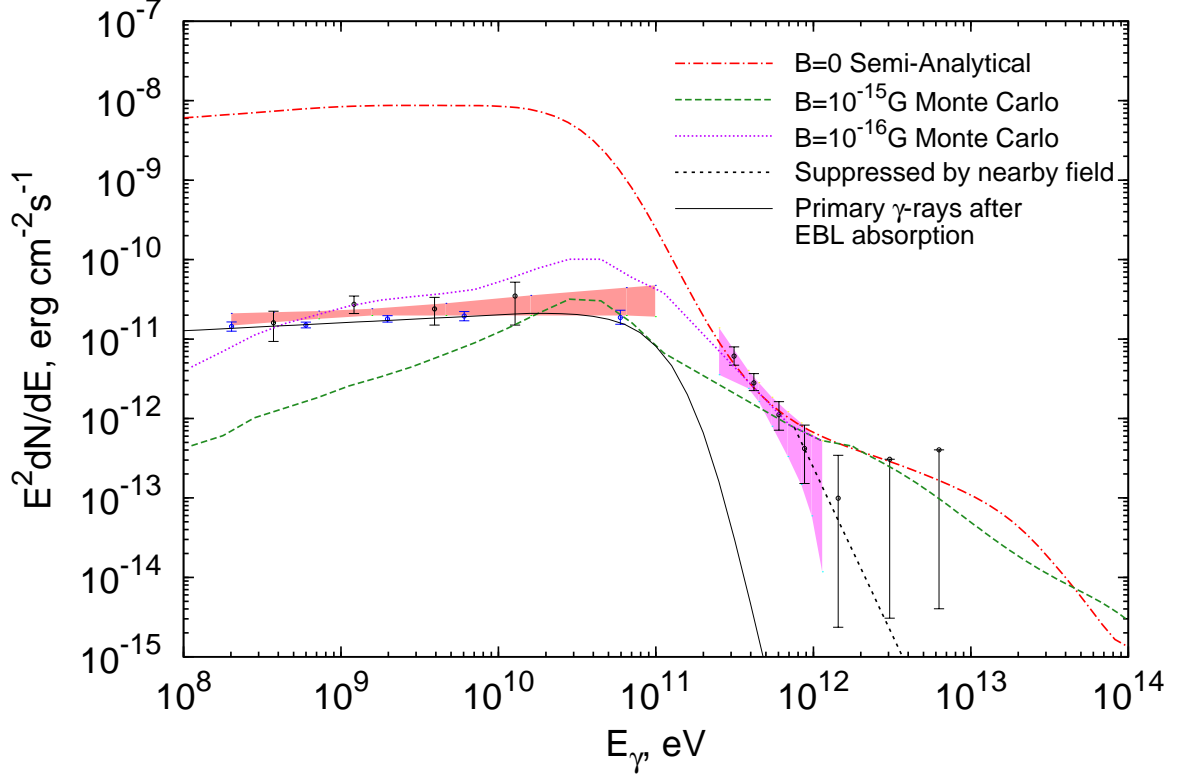


Figure 4.13: Spectra of secondary gamma rays produced by protons from a source at $z = 1.3$, calculated using semianalytical and Monte Carlo techniques. All theoretical curves are normalized to the observed flux around 1 TeV. The Fermi LAT data are shown according to 1LAC catalog [111] (smaller error bars), and according to Ref. [112] (large error bars). The data above 0.1 TeV are from HESS [113]. The semianalytical calculations correspond to the magnetic field $B = 0$ and protons injected with E_p^{-2} type energy spectrum in the energy interval $E_p = 10^{17} - 10^{18}$ eV. Monte Carlo results for the secondary spectrum from protons with a high energy cutoff of 10^{19} eV are shown for IGMF $B = 10^{-16}$ G and $B = 10^{-15}$ G. The effect of significantly enhanced magnetic field within $D \lesssim 100$ Mpc of the observer is shown for illustration of a possible suppression of the spectrum above 1 TeV. Also shown is the spectrum from a pure-gamma (no cosmic rays) source with injection spectrum E_γ^{-2} , after intergalactic absorption for the EBL model of Ref. [69].

4.9 Case study: a blazar at $z = 1.3$

Regardless of the observational status of PKS 0447-439 redshift, it is important to understand whether secondary gamma rays can be detected from a source at a large redshift. Therefore, we use PKS 0447-439 as a case study for this more general question,

assuming it has a redshift $z \approx 1.3$, as claimed in Ref. [114]. The analysis presented below should be viewed as a methodological study whose goal is to demonstrate that the model does allow TeV blazars at redshifts $z \geq 1$ to be observed, and that neither a dramatic revision of high-energy processes in blazars, nor new nonstandard interactions of gamma rays are necessary.

Cosmic-ray protons with energies $E \leq 10^{18}$ eV do not lose a significant part of their energy to interactions with the background photons, and, as long as the IGMFs are very weak, the protons can provide an effective transport of the energy over a large (cosmological) distance toward the observer. Cosmic ray interactions with CMBR and EBL, via the Bethe-Heitler pair production $p\gamma \rightarrow pe^+e^-$ and the photomeson reactions $p + \gamma_b \rightarrow p + \pi^0$, initiate electromagnetic cascades. The resulting secondary VHE gamma rays are observed as arriving from a point source, provided that the broadening of both the proton beam and the cascade electrons due to the deflections in IGMFs does not exceed the point spread function of the detector. In the case of detection of VHE gamma rays from PKS 0447-439 by the HESS telescope array [113], $\theta_p, \theta_{\text{cas}} \leq 3$ arcmin. While the broadening of the proton beam takes place over the entire path of protons from the source to the observer (zone 1), the diffusion of electrons in the *transparency zone* (zone 2) is the most important factor for the broadening of the cascade emission. Therefore, strictly speaking, one should distinguish between the magnetic fields in these two zones, B_1 and B_2 , respectively. The corresponding deflection angles are [17]

$$\theta_p \approx 0.05 \text{ arcmin} \left(\frac{10^{18} \text{ eV}}{E_p} \right) \left(\frac{B_1}{10^{-15} \text{ G}} \right) \left(\frac{L}{\text{Mpc}} \frac{d}{\text{Gpc}} \right)^{1/2} \quad (4.30)$$

and

$$\theta_{\text{cas}} \approx 3.8 \text{ arcmin} \left(\frac{10^{12} \text{ eV}}{E_\gamma} \right) \left(\frac{B_2}{10^{-15} \text{ G}} \right), \quad (4.31)$$

where L is the coherence length, and d is luminosity distance. One can see that, for comparable strengths of magnetic fields in two zones, the angular broadening is mainly due to the electron deflections in the *transparency zone*. Remarkably, such a deflection depends only on the magnetic field B_2 and the gamma-ray energy E_γ . Thus, a detection of an energy-dependent angular broadening of gamma-ray emission from blazars can provide a direct measurements of IGMF in a given direction [44].

The deflections of protons and cascade electrons result in delays of the arrival times

of the signal. In the two zones defined above,

$$\Delta\tau_p \approx 1.5 \cdot 10^6 \text{ s} \left(\frac{E_p}{10^{18} \text{ eV}} \right)^{-2} \left(\frac{B}{10^{-15} \text{ G}} \right)^2 \times \left(\frac{L}{1 \text{ Mpc}} \right) \left(\frac{d}{1 \text{ Gpc}} \right)^2 \quad (4.32)$$

and

$$\Delta\tau_\gamma \approx 1.3 \cdot 10^6 \text{ s} \left(\frac{E_\gamma}{10^{12} \text{ eV}} \right)^{-5/2} \left(\frac{B}{10^{-15} \text{ G}} \right)^2. \quad (4.33)$$

One can see that, for $B_1 \sim B_2 \sim 10^{-15} \text{ G}$, any time structure in the initial signal of 10^{18} eV protons on time scales of the order of a month or shorter are smeared out. Conversely, the interpretation of a variable VHE gamma-ray signal on time scales less than 1 month, in the framework of this model, would require magnetic field in both zones to be significantly weaker than 10^{-15} G . On the other hand, even for such small magnetic fields, the gamma-ray signals at GeV energies should be stable on time scales of tens of years.

Finally, a distinct feature of the proposed model is the spectral shape of gamma radiation. For relatively nearby sources, $z \ll 1$, the gamma-ray spectrum is flat, with a modest maximum around 10^{11} eV . For cosmologically distant sources with $z \geq 1$, the spectrum is steep in the sub-TeV part of the spectrum (down to 10 GeV), with a tendency of noticeable hardening above 1 TeV (see Fig. 4.11). Remarkably, the spectrum effectively extends to 10 TeV and higher energies even for cosmologically distant objects. However, a cutoff in the spectrum below a TeV energy cannot be excluded if the magnetic field in the $\approx 100 \text{ Mpc}$ vicinity of the observer significantly exceeds 10^{-15} G .

For a nearby source, the spectral shape of secondary photons is remarkably independent of the details of the proton energy spectrum [51, 52], although the efficiency decreases dramatically for the proton energy below 10^{18} eV . For cosmologically distant sources, the shape of the gamma-ray spectrum does depend on the proton energy, especially at $E \leq 10^{18} \text{ eV}$. For a source at $z \geq 1$, the proton energy is transferred to gamma rays with a maximal efficiency if $E \approx 10^{18} \text{ eV}$. Therefore, for an arbitrary spectrum of cosmic rays, the main contribution to secondary gamma rays comes from a relatively narrow energy interval of protons around 10^{18} eV . On the other hand, the gamma-ray spectrum produced by these protons in extremely low IGMF ($B \leq 10^{-17} \text{ G}$) disagrees with the broadband SED of gamma rays detected by Fermi LAT and HESS as shown in Fig. 4.13. This suggests the presence of magnetic fields stronger than 10^{-17} G . In a stronger magnetic field, deflections of the cascade electrons make the gamma-ray beam at low energies broader. The deflected flux does not contribute to a point source, but

rather to the diffuse extragalactic background radiation. Meanwhile, VHE gamma rays may be confined in the initial narrow beam. This effect is demonstrated in Fig. 4.13 which is produced using the method described in Ref. [52]. For the IGMF $B \geq 10^{-17}$ G, the GeV gamma-ray flux within an angle corresponding to the PSF of HESS, drops by two orders of magnitude to the level detected by Fermi LAT. The impact on the spectrum of VHE gamma rays is less pronounced, unless the magnetic field exceeds 10^{-14} G.

The results presented in Fig. 4.13 show that secondary gamma rays can describe correctly the spectrum of PKS 0447-439, as long as IGMFs are in the range $10^{-17}\text{G} < B < 10^{-14}\text{G}$, assuming random fields with a correlation length of 1 Mpc. This range of IGMF can be narrowed significantly in the future angular and temporal studies, leading to a more precise measurement of the magnetic field strengths along the line of sight. For example, detection of variability of VHE emission on timescales less than a few days would imply the values of magnetic fields close to 10^{-17} G. It is also important to search for an unavoidable (in the framework of this model) broadening of the angular extent of gamma-ray signals from cosmologically distant blazars. The choice of the gamma-ray energy for such studies depends on the magnetic field. The detection of such an effect would be another strong argument in favor of the proposed scenario, and it would allow an accurate measurements of IGMFs in different directions.

4.10 Discussion

One can see from Fig. 4.13 that the energy spectrum of gamma rays is quite stable from several hundred GeV to 10 TeV and beyond. Although the current statistics of the results reported by HESS does not allow robust conclusions regarding the energy spectrum above 1 TeV, the detection of multi-TeV gamma rays from PKS 0447-439 as well as from other cosmologically distant blazars would not be a surprise, but rather a natural consequence of the proposed scenario. However, we note that, if the magnetic field is enhanced in the *transparency zone*, i.e. in the vicinity of the observer, it could cause a strong suppression of the gamma-ray flux above some energy which can be found from the condition $\lambda_{\gamma\gamma}(E) = D$. The impact of this effect on the gamma-ray spectrum detected by an observer strongly depends on the linear scale of the enhanced magnetic field, D , but not much on the magnetic field itself (as long as the latter is significantly larger than 10^{-15}G). For example, for $D \sim 300$ Mpc, the steepening of the gamma-ray spectrum starts effectively around 1 TeV. This effect is illustrated qualitatively in Fig. 4.13.

The isotropic luminosity of the source in protons required to explain the data [113],

is in the range $(1 - 3) \times 10^{50}$ erg/s, depending on the spectrum of protons. This is an enormous, but not an unreasonable power, given that the actual (intrinsic) luminosity can be smaller by several orders of magnitude if the protons are emitted in a small angle. In particular, for $\Theta = 3^\circ$, the intrinsic luminosity is comparable to the Eddington luminosity of a black hole with a mass $M \sim 10^9 M_\odot$. Assuming that only a fraction of the blazar jet energy is transferred to high-energy particles, the jet must operate at a super-Eddington luminosity. While it may seem extreme, this suggestion does not contradict the basic principles of accretion, provided that most of the accretion energy is converted to the kinetic energy of an outflow/jet, rather than to thermal radiation of the accretion flow. Moreover, there is growing evidence of super-Eddington luminosities characterizing relativistic outflows in GRBs and in very powerful blazars [117].

Finally, we note that the protons emitted by cosmologically distant objects are potential contributors to the diffuse gamma-ray background. The total energy deposited into the cascades through secondary Bethe-Heitler pair production does not depend on the orientation of the jet or the beaming angle, but only on the injection power of $\geq 10^{18}$ eV protons and on the number of such objects in the universe. Generally, the total energy flux of gamma rays is fairly independent of the strength of the intergalactic magnetic fields, except for the highest energy part of the gamma-ray spectrum. If the contribution of these sources to the diffuse gamma-ray background is dominated by cosmologically distant objects, then the development of the proton-induced electron-photon cascades is saturated at large redshifts. One should, therefore, expect a rather steep (strongly attenuated) spectrum of diffuse gamma rays above 100 GeV. However, in the case of very small intergalactic magnetic fields, the 10^{18} eV protons can bring significant amount of nonthermal energy to the nearby universe, and thus enhance the diffuse background by TeV photons. Perhaps, this can explain the unexpected excess of VHE photons in the spectrum of the diffuse gamma-ray background as revealed recently by the Fermi LAT data [118].

4.11 Summary

Blazars are expected to produce both gamma rays and cosmic rays. Therefore, observed high-energy gamma rays from distant blazars may contain a significant contribution from secondary gamma rays produced along the line of sight by the interactions of cosmic-ray protons with background photons. Secondary photons contribute to signals of point sources only if the intergalactic magnetic fields are very small, $B \lesssim 10^{-14}$ G, and their detection can be used to set upper bounds on magnetic fields along the line of sight. Secondary gamma rays have distinct spectral and temporal features. The tempo-

ral properties of such signals using a semi-analytical formalism and detailed numerical simulations, which account for all the relevant processes, including magnetic deflections have been explored. In particular, the interplay of time delays coming from the proton deflections and from the electromagnetic cascade is clarified, and it is found that, at multi-TeV energies, secondary gamma rays can show variability on timescales of years for $B \sim 10^{-15}$ G.

Moreover, it has been shown that TeV gamma rays can be observed even from a source at $z \geq 1$, if the observed gamma rays are secondary photons produced in interactions of high-energy protons originating from the blazar jet and propagating over cosmological distances almost rectilinearly. For TeV gamma-ray radiation detected from a blazar with $z \geq 1$, this model would provide the only viable interpretation consistent with conventional physics. It would also have far-reaching astronomical and cosmological ramifications. In particular, this interpretation would imply that extragalactic magnetic fields along the line of sight are very weak, in the range $10^{-17}\text{G} < B < 10^{-14}\text{G}$, assuming random fields with a correlation length of 1 Mpc, and that acceleration of $E \geq 10^{17}$ eV protons in the jets of active galactic nuclei can be very effective.

Appendix: Distribution function in the expanding space

In this section the evolution of the distribution function of the ultrarelativistic particles propagating in the expanding Universe is described. The formalism is used for calculation of the distribution functions of the protons propagating cosmological distances and suffering from the energy losses.

Let us consider the collisionless Boltzmann equation

$$\left(\frac{\partial}{\partial t} + \frac{\partial \mathcal{H}}{\partial \mathbf{p}} \frac{\partial}{\partial \mathbf{r}} - \frac{\partial \mathcal{H}}{\partial \mathbf{r}} \frac{\partial}{\partial \mathbf{p}} \right) f(t, \mathbf{r}, \mathbf{p}) = 0. \quad (4.34)$$

For further usage it is convenient to rewrite this equation in terms of the distribution function over energy E and direction $\mathbf{n} = \mathbf{p}/p$

$$dN = F(t, \mathbf{r}, \mathbf{n}, E) \frac{d\Omega}{4\pi} dE d^3r \quad (4.35)$$

instead of the distribution function $f(t, \mathbf{r}, \mathbf{p})$ over the the generalized momentum \mathbf{p}

$$dN = f(t, \mathbf{r}, \mathbf{p}) d^3p d^3r. \quad (4.36)$$

Taking into account that

$$d^3p d^3r = d^3P dV, \quad (4.37)$$

where dV is the element of physical volume, and P is the usual momentum registered by observer, the relation between both distribution functions is

$$f(t, \mathbf{r}, \mathbf{p}) = \frac{F(t, \mathbf{r}, \mathbf{n}, E)}{4\pi P E}. \quad (4.38)$$

We consider ultrarelativistic particles freely propagating in the flat space. In this case the Hamiltonian \mathcal{H} (or the energy) is expressed in terms of generalized momentum as

$$\mathcal{H} = \frac{p}{a}. \quad (4.39)$$

The expression $p = a(t)E$ results in the following change of variables in the Boltzmann equation:

$$\left(\frac{\partial f}{\partial t} \right)_p = \left(\frac{\partial f}{\partial t} \right)_E - \frac{\dot{a}}{a} E \left(\frac{\partial f}{\partial E} \right)_t. \quad (4.40)$$

Taking this expression into consideration, and substituting Eqs. (4.38) and (4.39) into the Boltzmann equation (4.34) we obtain

$$\frac{\partial F}{\partial t} - \frac{\partial}{\partial E} [(HE)F] + 3HF + \frac{1}{a} \mathbf{n} \frac{\partial F}{\partial \mathbf{r}} = 0, \quad (4.41)$$

where $H = \dot{a}/a$ is the Hubble constant. The second term in the left side of the equation describes adiabatic losses due to expansion of the space. We can generalise the equation for the case of the arbitrary energy losses $b(t, E)$ which includes the adiabatic losses, and the arbitrary source function $S(t, \mathbf{r}, \mathbf{n}, E)$

$$\frac{\partial F}{\partial t} - \frac{\partial}{\partial E} [b(t, E)F] + 3HF + \frac{1}{a} \mathbf{n} \frac{\partial F}{\partial \mathbf{r}} = S(t, \mathbf{r}, \mathbf{n}, E). \quad (4.42)$$

To solve this equation we use the method of Green function. Then the source is presented by the instant injection of the particles at the point \mathbf{r}_0 in the moment t_0 with the energy E_0 in the direction \mathbf{n}_0

$$S_\delta(t, \mathbf{r}, \mathbf{n}, E) = \delta(t - t_0) \delta(\mathbf{r} - \mathbf{r}_0) \delta(E - E_0) \delta(\mathbf{n} - \mathbf{n}_0), \quad (4.43)$$

where δ is the Dirac delta function. From the physical consideration the particles propagating without deflection with the speed of light and losing energy in the expanding universe should pass the comoving distance $d\mathbf{r} = \mathbf{n}_0 dt/a(t)$ and have the energy $E = \mathcal{E}(t, E_0, t_0)$. Also taking into account the change of density due to expansion we

seek the Green function G in the form

$$G(t, \mathbf{r}, \mathbf{n}, E, t_0, \mathbf{r}_0, \mathbf{n}_0, E_0) = \exp \left(-3 \int_{t_0}^t H(t') dt' \right) \delta(E - \mathcal{E}(t, E_0, t_0)) \quad (4.44)$$

$$\times \delta \left(\mathbf{r} - \mathbf{r}_0 - \mathbf{n}_0 \int_{t_0}^t \frac{dt'}{a(t')} \right) \delta(\mathbf{n} - \mathbf{n}_0) \theta(t - t_0).$$

Substituting this expression into the Boltzmann equation for the Green function

$$\frac{\partial G}{\partial t} - \frac{\partial}{\partial E} [b(t, E)G] + 3HG + \frac{1}{a} \mathbf{n} \frac{\partial G}{\partial \mathbf{r}} = S_\delta(t, \mathbf{r}, \mathbf{n}, E) \quad (4.45)$$

we obtain the differential equation for the function \mathcal{E}

$$\frac{d\mathcal{E}}{dt} + b(t, \mathcal{E}) = 0 \quad (4.46)$$

with the initial condition

$$E_0 = \mathcal{E}(t_0, E_0, t_0). \quad (4.47)$$

The first term in the right side of Eq. (4.44) can be rewritten as

$$\exp \left(-3 \int_{t_0}^t H(t') dt' \right) = \left(\frac{a(t_0)}{a(t)} \right)^3. \quad (4.48)$$

Then the solution of Boltzmann equation (4.42) is

$$F(t, \mathbf{r}, \mathbf{n}, E) = \int_0^t dt_0 \left(\frac{a(t_0)}{a(t)} \right)^3 \int dE_0 \delta(E - \mathcal{E}(t, E_0, t_0)) \quad (4.49)$$

$$\times S \left(t_0, \mathbf{r} - \mathbf{n} \int_{t_0}^t \frac{dt'}{a(t')}, \mathbf{n}, E_0 \right). \quad (4.50)$$

Eq. (4.49) with Eqs. (4.46) and (4.47) gives the distribution function of the particles propagating in the expanding space with the energy losses $b(t, E)$ which include adiabatic losses due to expansion and the arbitrary source function $S(t, \mathbf{r}, \mathbf{n}, E)$.

Let us consider the case of the continuous in time point-like source which starts its activity at the moment t_s and radiates isotropically ultrarelativistic particles with the

energetic spectrum $J(E)$

$$S(t, \mathbf{r}, \mathbf{n}, E) = \frac{J(E)}{4\pi a^3(t)} \delta(\mathbf{r}) \theta(t - t_s) \quad (4.51)$$

The term $a^3(t)$ appears because the delta function depends on comoving coordinate whereas the source function is determined over usual (not comoving) volume. Substituting the source function (4.51) into the solution (4.49) and using the properties of delta function we come to the expression of the distribution function

$$F(t, \mathbf{r}, \mathbf{n}, E) = \frac{a(t_*)}{a(t)} \frac{J(E_*)}{4\pi R^2} \left(\left| \frac{d\mathcal{E}(t, E_0, t_*)}{dE_0} \right|_{E_0=E_*} \right)^{-1} \delta(\mathbf{n} - \mathbf{n}_r), \quad (4.52)$$

where $R = a(t)r$, t_* is determined from the equation

$$r = \int_{t_*}^t \frac{dt'}{a(t')} \quad (4.53)$$

and E_* is determined from the equation

$$E = \mathcal{E}(t, E_*, t_*). \quad (4.54)$$

To find E_* it is convenient to solve Eq.(4.46) inversely over time from t to t_* . In the function $\mathcal{E}(t', E, t)$ only the first argument t' changes, the second and the third one are initial conditions. Then we should solve the equation

$$\frac{d\mathcal{E}(t', E, t)}{dt'} + b(t', \mathcal{E}(t', E, t)) = 0 \quad (4.55)$$

with the initial condition

$$\mathcal{E}(t, E, t) = E. \quad (4.56)$$

Notice that $E'(E_0) = \mathcal{E}(t, E_0, t_*)$ and $E_0(E') = \mathcal{E}(t_*, E', t)$. Therefore

$$\left(\frac{d\mathcal{E}(t, E_0, t_*)}{dE_0} \right)^{-1} = \frac{d\mathcal{E}(t_*, E', t)}{dE'}. \quad (4.57)$$

We can determine the derivative of \mathcal{E} over energy as a new function

$$\Psi(t', E', t) = \frac{\partial \mathcal{E}(t', E', t)}{\partial E'}. \quad (4.58)$$

This function obeys the equation obtained from the differentiation of the Eq. (4.55) over

variable E

$$\frac{d\Psi(t', E, t)}{dt'} + b'(t', \mathcal{E}(t', E, t))\Psi(t', E, t) = 0 \quad (4.59)$$

with the initial condition

$$\Psi(t, E, t) = 1. \quad (4.60)$$

Here we introduce the notation $b'(t, E) = db(t, E)/dE$. Finally the distribution function can be written in the form

$$F(t, r, E) = \frac{a(t_*)}{a(t)} \frac{J(E_*)}{4\pi R^2} \Psi(t_*, E, t), \quad (4.61)$$

where $E_* = \mathcal{E}(t_*, E, t)$ and $\Psi(t_*, E, t)$ are found from differential Eqs. (4.55), (4.59) with initial conditions Eqs. (4.56), (4.60), respectively.

It is useful for calculations to write the solution (4.61) in the terms of redshift. The standard model gives the following relation between time and redshift

$$\frac{dt}{dz} = -\frac{1}{H_0(1+z)\sqrt{\Omega_m(1+z)^3 + \Omega_\Lambda}}, \quad (4.62)$$

where z is the redshift, $\Omega_m = 0.27$ is the matter density, $\Omega_\Lambda = 0.73$ is the dark energy density, $H_0 = 71$ km/s/Mpc is the Hubble constant. With the introduction of the function

$$H(z) = H_0\sqrt{\Omega_m(1+z)^3 + \Omega_\Lambda} \quad (4.63)$$

we can rewrite Eqs. (4.55), (4.59) in the following system of the differential equations:

$$\frac{d\mathcal{E}(z, E, z_o)}{dz} = \frac{1}{1+z} \left(\mathcal{E}(z, E, z_o) + \frac{b(z, \mathcal{E}(z, E, z_o))}{H(z)} \right), \quad (4.64)$$

$$\frac{d\Psi(z, E, z_o)}{dz} = \frac{\Psi(z, E, z_o)}{1+z} \left(1 + \frac{b'(z, \mathcal{E}(z, E, z_o))}{H(z)} \right) \quad (4.65)$$

with the initial conditions

$$\mathcal{E}(z_o, E, z_o) = E, \quad (4.66)$$

$$\Psi(z_o, E, z_o) = 1. \quad (4.67)$$

Here, unlike the previous notations, the adiabatic energy losses due to the expansion of the Universe are written separately and described by the first term on the right side. The function $b(z, E)$ describes the energy losses due to other processes. This system is integrated from the redshift of the observer z_o to the redshift of the emission z_e . Having

found the solution of the system at the emission point z_e we can write the distribution function in the form:

$$F(z_o, z_e, E) = \frac{(1 + z_o)^3}{1 + z_e} \frac{J(\mathcal{E}(z_e, E, z_o))}{4\pi r^2} \Psi(z_e, E, z_o), \quad (4.68)$$

where the comoving distance r is

$$r = c \int_{z_o}^{z_e} \frac{dz}{H(z)}, \quad (4.69)$$

and c is the speed of light.

For the case of the free propagation of the photons the solution is found analytically:

$$F(z_o, z_e, E) = (1 + z_o)^2 \frac{J\left(E \frac{1+z_e}{1+z_o}\right)}{4\pi r^2}. \quad (4.70)$$

If the observer is located at $z_o = 0$ and $z_e = z$ we obtain

$$F(z, E) = \frac{J(E(1+z))}{4\pi r^2}. \quad (4.71)$$

5 Synchrocurvature radiation in a strong magnetic field

5.1 Introduction

The efficiency of synchrotron radiation depends on the pitch angle between the magnetic field and the particle velocity. The damping of the perpendicular motion in course of radiation reduces the pitch angle. Typically, in moderate magnetic fields the pitch angle changes slowly. Therefore, for calculations of synchrotron radiation, it is sufficient to specify the initial pitch angle distribution of particles.

The situation is different in strong magnetic fields, namely when the energy losses become so intensive that on fairly short timescales the pitch angle can be reduced by orders of magnitude. In this regard, the adequate theoretical treatment of particle trajectories becomes a key issue for correct calculations of radiation properties. In a curved magnetic field the strong damping of the perpendicular motion causes transition from synchrotron to the curvature radiation regime of radiation. The solutions of equations that describe the particle motion with an inclusion of energy losses, allow us to trace this transition, and thus to calculate the magnetic bremsstrahlung without additional assumptions regarding the radiation regime.

In this chapter, we study the case of motion of a charged particle in the dipole magnetic field, and calculate self-consistently the radiation spectrum taking into account the time-evolution of particle's energy, coordinates, and direction. We demonstrate that even a small deviation of particle's initial direction from the magnetic field line may have a strong impact on the character of radiation. Despite the fast transition to the *final* (curvature) regime, the particle radiates away the major fraction of its energy in the *initial* (synchrotron) or *transitional* (synchro-curvature) regimes. Consequently, the energy spectrum of radiation may differ considerably from the spectrum of curvature radiation.

5.2 General comments

In a strong magnetic field, the motion of a charged particle perpendicular to the field is damped. The amount of energy lost during this process depends on the initial energy and the pitch angle. In the case of relativistic motion along and perpendicular to the magnetic field, $p_{\parallel} \gg mc$ and $p_{\perp} \gg mc$, particles can lose a large fraction of their energy even if the initial pitch angle is small. Indeed, after the complete damping of the perpendicular component of motion in a homogeneous magnetic field, the parallel momentum becomes [119]

$$p'_{\parallel} = p_{\parallel} \frac{mc}{\sqrt{p_{\perp}^2 + m^2 c^2}}. \quad (5.1)$$

Then for small initial pitch angles $\alpha \ll 1$ and for the relativistic motion perpendicular to the magnetic field, we obtain that the final Lorentz factor depends only on the initial pitch angle:

$$\gamma' \approx \frac{1}{\alpha}. \quad (5.2)$$

It is convenient to rewrite this expression in the following form:

$$\gamma' \approx \frac{\gamma}{\gamma_{\perp}}, \quad (5.3)$$

where $\gamma_{\perp} = \gamma \sin \alpha$ is referred hereafter as perpendicular Lorentz factor. We see that at an ultrarelativistic motion of particle, even a tiny deflection $\alpha = \gamma_{\perp}/\gamma$ from the magnetic field line can cause large energy losses $\Delta E = E(1 - 1/\gamma_{\perp}) \approx E$.

The damping rate depends on the strength of the magnetic field. The super-strong magnetic fields surrounding of compact astrophysical objects, such as pulsars and black holes, cause very fast damping of the perpendicular component of motion, and in this way force the particle to move along magnetic field lines. However, since the magnetic field lines are curved, the change of the field direction results in an appearance of the perpendicular velocity. The curvature of magnetic field lines and the presence of the perpendicular velocity lead to the curvature drift (an averaged motion perpendicular to the magnetic field due to non-compensated differences in the trajectory of the periodic motion arising from changes of the magnetic field direction). Thus, after losing most its perpendicular motion in a curved magnetic field, the particle moves along the *drift* trajectory gyrating around it.

The radiation spectrum is determined by the curvature of particle's trajectory which is a superposition of the drift and the gyration around it. As long as the real trajectory is close to the magnetic field lines, for calculations of radiation spectra one can use the curvature of the magnetic field lines instead of the trajectory curvature. The difference

between the magnetic field curvature and the drift trajectory curvature can be neglected until the curvature drift velocity is small. In case of the magnetic field of a long straight wire, the curvature of the drift trajectory is

$$K_D = \frac{1}{r_0(1 + \beta_D^2)} \approx \frac{1 - \beta_D^2}{r_0}, \quad (5.4)$$

where r_0 is the curvature radius of the magnetic field, β_D is the drift velocity in the units of the speed of light expressed as [120]

$$\beta_D = \frac{v_D}{c} = \frac{c}{\Omega r_0} = \frac{mc^2\gamma}{eBr_0}, \quad (5.5)$$

where $\Omega = eB/mc\gamma$ is the gyration frequency, and B is the strength of the magnetic field. The gyration itself introduces a much larger difference if the velocity perpendicular to the drift trajectory β_\perp is of the order of the drift velocity [119]

$$K = \frac{1}{r_0} \sqrt{1 - 2\frac{\beta_\perp}{\beta_D} \cos \tau + \frac{\beta_\perp^2}{\beta_D^2}}. \quad (5.6)$$

Note that the particle in the magnetic field of a long straight wire can move strictly along the drift trajectory without gyration ($\beta_\perp = 0$) and therefore with minimum possible energy losses. Because of the possibility of such motion, and treating the motion with gyration as a perturbation, [119] has called the drift trajectory as a “smooth trajectory”. Having the potential minimum on the drift trajectory, the particle with any initial pitch angle due to energy losses will asymptotically reach the motion strictly along the drift trajectory. In the case of an arbitrary magnetic field, when the curvature is variable, it is not possible to make a definite statement, except that the particle tries to reach the potential minimum according to the local values of the magnetic field. If the curvature changes slowly, the particle motion could become very close to the drift trajectory ($\beta_\perp \approx 0$), but, because of gyration, never strictly approaches it ($\beta_\perp = 0$) as in the case of magnetic field of an infinitely long straight wire.

The energy loss rate and the radiation spectrum behave differently from the case of the curvature radiation when the velocity component perpendicular to the drift trajectory β_\perp is comparable or larger than the drift velocity β_D . Because of gyration, the radiation is expected to be different from the pure curvature radiation, even when initially the particle moves strictly along the magnetic field line ($\beta_\perp = \beta_D$). The nominal curvature radiation is generally treated as the same synchrotron radiation [121] with a spectral maximum at the characteristic frequency ω_* corresponding to the curvature radius of

the magnetic field line instead of the curvature radius of the real trajectory. The substitution of the real trajectory curvature affects the radiation spectrum, namely shifts the maximum to $\approx (1 + \beta_{\perp}/\beta_D)\omega_*$. Thus, the difference from the curvature radiation becomes significant when $\beta_{\perp}/\beta_D \gg 1$. If the pitch angle is much larger than the angle between the magnetic field line and the drift trajectory, one can neglect it and consider β_{\perp} as the velocity perpendicular to magnetic field line (although β_{\perp} is the velocity perpendicular to the drift trajectory). It implies the dominance of the ratio β_{\perp}/β_D in the expression $1 + \beta_{\perp}/\beta_D$, i.e. the radiation deviates significantly from the curvature radiation when the velocity perpendicular to the magnetic field is greater than the drift velocity.

It is interesting to study the possibility of pitch angles greater than β_D . This question is specific and its answer depends on the acceleration mechanism, but here we would like to discuss very general points. The pitch angle of the particle accelerated by the electric field in the presence of magnetic field depends on the relation between strengths of the fields and the angle between them. It is worth to mention the result of acceleration in the crossed homogeneous fields. In this case one can find the reference frame where the fields are parallel. The particle in this reference frame is infinitely accelerated along the parallel fields and lose the perpendicular component of the motion. Taking the motion along the field and transforming the velocity back to the laboratory reference frame, the pitch angle can be expressed as

$$\sin \alpha = \frac{\rho \sin \theta}{\sqrt{\frac{1}{2} \left(\sqrt{(1 + \rho^2)^2 - 4\rho^2 \sin^2 \theta} + (1 + \rho^2) \right)}}, \quad (5.7)$$

where $\rho = E/B$ is the ratio of the electric and magnetic fields, and θ is the angle between them. Assuming that typically the electric field is smaller than magnetic field, we obtain

$$\sin \alpha \approx \rho \sin \theta \quad (5.8)$$

which states that the pitch angle equals the drift velocity due to electric drift (in the units of the speed of light).

In a more general case, a drift due to the electric field should appear as well. Then we arrive at a quite general conclusion that the radiation of the accelerated particle could be considerably different from the curvature radiation if the electrical drift exceeds the curvature drift

$$\rho \sin \theta \gg \beta_D. \quad (5.9)$$

The so-called outer gap model of pulsars gives an example of existence of a perpen-

dicular component of the electric field. In the acceleration gaps, the electric field could not be parallel to the magnetic field everywhere, in particular close to the border of the gap the perpendicular component of the electric field is increased [122]. In these regions the radiation can be different from the curvature radiation.

5.3 Local trajectory

The accurate calculation of the radiation spectrum requires detailed knowledge of the trajectory of charged particle. The latter obtained in the drift approximation is not suitable for this purpose since the fast gyrations are erased in the course of averaging. Fortunately, under the assumption that the gyroradius is small, it is possible to obtain a local solution which takes into account fast gyrations for the motion in an arbitrary curved magnetic field [123]. This approach is equivalent to the consideration of particle motion in the magnetic field which is constant along binormal and has a constant curvature and zero torsion. The magnetic lines of this field present circles with centres lying on a straight line. The magnetic field of this structure is created by the current of an infinitely long straight wire. It allows us to consider the solution obtained in [119] for such field as a local one. This consideration is also possible because a small part of the curved magnetic field line can always be approximated by the arc of a circle with the radius equal to the curvature radius of the line.

We consider the particle motion in the local coordinate system:

$$\mathbf{r} = s\mathbf{h} + x\mathbf{n} + y\mathbf{k}, \quad (5.10)$$

where $\mathbf{h} = \mathbf{B}/B$ is the unit vector in the direction of the magnetic field, $\mathbf{k} = \mathbf{h} \times \mathbf{n}$ is the binormal vector, $\mathbf{n} = r_0(\mathbf{h}\nabla)\mathbf{h}$ is the normal vector with r_0 as the curvature radius. Then, in accordance with [119], the local velocity can be written as

$$\mathbf{v} = v_s\mathbf{h} + v_x\mathbf{n} + v_y\mathbf{k}, \quad (5.11)$$

where

$$\begin{aligned} v_s &= c\beta_{\parallel} \left(1 + \frac{\beta_{\perp}\beta_D}{\beta_{\parallel}^2} \cos \tau \right), \\ v_x &= c\beta_{\perp} \sin \tau, \quad v_y = c\beta_D - c\beta_{\perp} \cos \tau. \end{aligned} \quad (5.12)$$

Here β_{\parallel} is the component of the velocity along magnetic field line, β_{\perp} is the component of the velocity perpendicular to the drift trajectory, β_D is the drift velocity defined in

Eq. (5.5) (all velocities are in units of c), $\tau = \Omega t$ is the time in the units of the gyration period $1/\Omega$.

The expressions in Eq. (5.12) describe the motion along the magnetic field line with gyration around it and the drift in the direction of the binormal to the magnetic field line. The solution formally includes also the case of strict motion along the drift trajectory without gyration ($\beta_{\perp} = 0$). Such a situation can occur only locally. Since the curvature of the magnetic field lines changes, the gyration does not disappear completely although it could be very small compared to the drift. Eq. (5.12) is correct if the radius of gyration is much smaller than the curvature radius. This is equivalent to the conditions $\beta_{\perp} \ll \beta_{\parallel}$ and $\beta_D \ll \beta_{\parallel}$. Moreover, it allows us to neglect the drift gradient which, otherwise, would lead (in the case of the vacuum magnetic field $\nabla \times \mathbf{B} = 0$) to the drift velocity

$$v_D = \frac{v_{\parallel}^2 + \frac{v_{\perp}^2}{2}}{r_0 \Omega}. \quad (5.13)$$

The expression for the acceleration in the magnetic field

$$\mathbf{a} = \frac{e}{mc\gamma}(\mathbf{v} \times \mathbf{B}), \quad (5.14)$$

and Eq. (5.12) allow us to find the absolute value of the acceleration

$$a = a_0 \sqrt{1 - 2\eta \cos \tau + \eta^2}, \quad (5.15)$$

where $a_0 = c^2 \beta_{\parallel}^2 / r_0$ is the acceleration due to curvature of the magnetic field, $\eta = \beta_{\perp} / \beta_D$ is the ratio between the velocity perpendicular to the drift trajectory and the drift velocity. It is convenient to introduce, as suggested in [119], a parameter which shows the difference between the total acceleration and the acceleration induced by the magnetic field curvature

$$q(\eta, \tau) = \frac{a}{a_0} = \sqrt{1 - 2\eta \cos \tau + \eta^2}. \quad (5.16)$$

Because of the simple relation between the acceleration and the curvature radius of the trajectory in the ultrarelativistic case $a = c^2 / R_c$, the q -parameter indicates also the difference between the trajectory curvature and the curvature of the magnetic field lines (compare with Eq. (5.6))

$$R_c = \frac{r_0}{q}. \quad (5.17)$$

As discussed in Sec. 2, we will neglect the difference between the curvature of the drift trajectory and the curvature of the magnetic field line.

The solution given by Eq. (5.12) can be applied locally if the parameters of the motion

such as the energy of the particle, the curvature and the strength of the magnetic field are changed slowly. In this case, the parameters of the solution Ω , β_\perp and β_D change slowly as well. The q -parameter varies in the limits $|1 - \eta| \leq q \leq 1 + \eta$. If $\eta \leq 1$, then q appears within the band of width 2η around $q = 1$. If $\eta > 1$, then q varies in the band of width 2 around $q = \eta$. So over the period of gyration, q could not change greater than 2. Naturally, if the parameters of the motion change considerably over the gyration period, the behaviour of q -parameter would be different.

5.4 Radiation spectrum

The spectral power density of the synchrotron radiation is defined by the instantaneous curvature radius of the particle trajectory [124]. For the curvature radius given by Eq. (5.17) the spectral power density of radiation of the particle moving in the curved magnetic field can be written in the form

$$P(\omega, t) = \frac{\sqrt{3}e^2}{2\pi} \frac{\gamma}{r_0} G\left(\frac{\omega}{\omega_*}\right), \quad (5.18)$$

where

$$G\left(\frac{\omega}{\omega_*}\right) = qF\left(\frac{\omega}{\omega_*q}\right). \quad (5.19)$$

Here $\omega_* = 3c\gamma^3/(2r_0)$ is the characteristic frequency of the curvature radiation and

$$F(x) = x \int_x^\infty K_{5/3}(u) du \quad (5.20)$$

is the emissivity function of synchrotron radiation. The q -parameter defined as the ratio between the total acceleration and the acceleration induced by the curvature of the magnetic field, can be expressed as

$$q = \frac{a}{a_0} = \frac{evB \sin \alpha}{mc\gamma} \frac{v_\parallel^2}{r_0} \approx \frac{\sin \alpha}{\beta_D}, \quad (5.21)$$

where α is the pitch angle, v is the particle velocity, v_\parallel is the velocity along the magnetic field. If the energy and the magnetic field are changed slowly, the local representation given by Eq. (5.16) can be used. Then the spectrum averaged over the period of the gyration is determined by the function

$$\left\langle G\left(\frac{\omega}{\omega_*}\right) \right\rangle = \frac{1}{\pi} \int_0^\pi q(\eta, \tau) F\left(\frac{\omega}{\omega_*q(\eta, \tau)}\right) d\tau. \quad (5.22)$$

In all cases under consideration the form of the spectrum is defined by the same function $F(x)$. The relevant parameters change only the position of the maximum and the intensity. However, the function $F(x)$ should be changed to its quantum analogue (see Eq. 5.39) if the parameter $\chi = B\gamma \sin \alpha / B_{cr}$ is of the order of unity and higher, where $B_{cr} = 2m^2c^3/3e\hbar \approx 2.94 \cdot 10^{13}$ G [125]. Note that at such conditions, the energy of the produced photon is close to the energy of the radiating electron. The electron-positron pair production by a gamma-ray photon in the strong magnetic field occurs when the parameter $\chi \gtrsim 1$, where γ is the photon energy in the units of the electron rest mass, and α is the angle between the photon and magnetic field. In the curved magnetic field the angle between photon and magnetic field could become sufficiently large for production of electron-positron pairs. This could lead, provided that the optical depth is large, to development of electromagnetic cascade and formation of radiation which is considerably different from the initial one.

The substitution of the q -parameter in the general form of Eq. (5.21) to Eq. (5.19) results in the standard spectral power density of the synchrotron radiation. Thus the q -parameter expresses the difference between the conventional curvature radiation (when the curvature of the trajectory is accepted to be equal to the curvature of the magnetic field line) and the actual radiation which is the small pitch angle synchrotron radiation. One can see that there is no well-defined boundary between the curvature and the synchrotron radiation. It seems natural to define the magnetic bremsstrahlung as *curvature radiation* when the main contribution is introduced by the curvature of the magnetic field line. This case corresponds to $\eta \ll 1$; see Eqs. (5.6) and (5.16). Then the *synchrotron radiation* occurs when the curvature of the trajectory induced by the strength of the magnetic field provides the main contribution to the radiation. This corresponds to $q \approx \eta \gg 1$. Finally, at $\eta \sim 1$ both the strength and the curvature of the magnetic field play equal role in production of emission which we will call *synchro-curvature* radiation.

The limits of applicability of Eq. (5.18) defining the energy spectra of the synchrotron and the curvature radiation originate from the approach of its derivation proposed by Swinger ([124]). The radiation of the ultrarelativistic particle is concentrated in a narrow cone with the opening angle $\sim 1/\gamma$ and is therefore collected while the angle between the velocity and the direction of the observation is of the order of the same of $\sim 1/\gamma$. The Swinger method is based on expansion of the trajectory in the small time interval. During this time interval, the entire observable radiation should be collected. It means that the approach works if the particle velocity changes the direction at an angle larger than $1/\gamma$ while the expansion is valid. The analysis of the local trajectory given by

Eq. (5.12) in the curved magnetic field gives the following limits of applicability:

$$\begin{aligned} \beta_{\perp} &\gg \frac{1}{\gamma}, \quad \text{if } \beta_{\perp} \gtrsim \beta_D, \\ \sqrt{\frac{\beta_D^3}{\beta_D^3 + \beta_{\perp}^2}} &\gg \frac{1}{\gamma}, \quad \text{if } \beta_{\perp} \lesssim \beta_D. \end{aligned} \quad (5.23)$$

The first condition corresponds to the case of synchrotron radiation and states that the perpendicular motion should be relativistic as it is expected from the consideration of radiation in the homogeneous magnetic field. The second condition corresponds to the situation for the curvature radiation of a particle with a small perpendicular momentum. Small gyrations almost do not influence on the applicability of Eq. (5.18) and in the limit $\beta_{\perp} = 0$ the condition simply states that the motion should be relativistic.

5.5 Numerical implementation

The analytical approach described above allows us to study the local properties of the particle trajectory and the radiation in the curved magnetic field. To solve the problem in the general case, taking into account the energy losses of particles, we performed numerical integration of the equations of motion. The radiation properties have been studied in the dipole magnetic field which seems to be a quite good approximation for the strong magnetic fields in compact astrophysical objects. The dipole magnetic field has two distinct features to be taken into account. The first one is the fast decrease of the strength with the distance $\sim 1/r^3$ with a strong impact on the radiation intensity. The second one is the significant variation of the curvature with a change of the polar angle θ from the dipole axis $\propto \sin \theta/r$, so the radiation spectra in the vicinity of the pole and the equator should be different.

For numerical calculations we use the equations of motion in the ultrarelativistic limit. In this case the radiation reaction force is opposite to the velocity which changes only its direction. The equation of motion can be written in the form

$$mc \frac{d}{dt}(\gamma \boldsymbol{\beta}) = e(\boldsymbol{\beta} \times \mathbf{B}) - |\mathbf{f}| \boldsymbol{\beta}, \quad (5.24)$$

where $\boldsymbol{\beta}$ is the velocity in units of c with $|\boldsymbol{\beta}| \approx 1$, \mathbf{B} is the magnetic field, and \mathbf{f} is the radiation reaction force [121]. Taking the scalar product of Eq. (5.24) with velocity $\boldsymbol{\beta}$ we obtain the differential equation for the energy losses. This equation allows cancellation of the radiation reaction force with the Lorentz factor time derivative in Eq. (5.24). Finally, the equation of motion has the same form as for the consideration without

energy losses, where the energy enters as a parameter. For the sake of convenience of the numerical treatment and comprehension of the structure of the system of equations, these equations are written in the dimensionless form:

$$\frac{d\mathbf{r}'}{d\tau} = u_1 \boldsymbol{\beta}, \quad (5.25)$$

$$\frac{d\boldsymbol{\beta}}{d\tau} = \xi(\boldsymbol{\beta} \times \mathbf{b}), \quad (5.26)$$

$$\frac{d\xi}{d\tau} = u_2(\boldsymbol{\beta} \times \mathbf{b})^2. \quad (5.27)$$

The system of equations depends on two dimensionless parameters

$$u_1 = \frac{mc^2\gamma_0}{eB_0R_0} \quad \text{and} \quad u_2 = \frac{2e^3B_0}{3m^2c^4}\gamma_0^2, \quad (5.28)$$

where γ_0 is the initial Lorentz factor, R_0 is the characteristic distance to the radiating region from the dipole, $B_0 = B_*(R_*/R_0)^3$ is the characteristic magnetic field with R_* and B_* being the source radius and the magnetic field at the pole of the dipole, m is a particle mass, c is the speed of light. Here we have introduced the following dimensionless variables: \mathbf{r}' is the coordinate in the character units of length R_0 , $\boldsymbol{\beta}$ is the velocity of the particle in the units of c , $\xi = \gamma_0/\gamma$ is the ratio of the initial and current value of the Lorentz factor, $\tau = teB_0/mc\gamma_0$ is the characteristic time in the units of the initial gyration period, \mathbf{b} is the dimensionless dipole magnetic field which is expressed as

$$\mathbf{b} = \frac{3\mathbf{n}(\mathbf{n}\boldsymbol{\mu}) - \boldsymbol{\mu}}{2r'^3}, \quad (5.29)$$

where $\boldsymbol{\mu}$ is the unit vector in the direction of the dipole axes, $\mathbf{n} = \mathbf{r}'/r'$ is the unit vector to the particle position.

It should be noted that depending on the specific conditions characterizing an astrophysical source, the parameters u_1 and u_2 may differ by many orders of magnitude. For instance, for typical parameters of the so-called *polar cap* model of pulsar magnetosphere $B_0 = 10^{12}$ G, $R_0 = 10^6$ cm, and $\gamma_0 = 10^8$, we have $u_1 \approx 1.7 \cdot 10^{-7}$ and $u_2 \approx 1.1 \cdot 10^{12}$. Thus the problem is non-stiff, therefore for integration of this system of differential equations the implicit Rosenbrock method has been used.

The calculations of the trajectory have been carried out for different initial conditions. The initial position determined by the radius R_0 and the polar angle θ_0 relative to the magnetic dipole axis defines the typical environment parameters for the models under consideration. The radiation spectrum has been studied for different initial pitch angles α_0 and initial Lorentz factors γ_0 . The detailed knowledge of the trajectory and the

energy allows us to find q -parameter from Eq.(5.21) and the radiation spectrum given by Eq. (5.18) at any moment of time. The spectra integrated over the time, the so called *cumulative spectrum*, have been obtained for any initial condition under consideration.

Finally, in the case of a very strong magnetic field and/or very large Lorenz factor, the particle may radiate in the quantum regime. More specifically, when the parameter $\chi = B\gamma \sin \alpha / B_{cr}$ becomes of the order of unity or larger, Eq. (5.27) should be replaced by its quantum analogue (see Appendix)

$$\frac{d\xi}{d\tau} = \frac{u_2(\boldsymbol{\beta} \times \mathbf{b})^2}{(1 + u_3((\boldsymbol{\beta} \times \mathbf{b})/\xi)^{2/3})^2}, \quad (5.30)$$

where $u_3 = 1.07 \cdot 10^{-9}(B_0\gamma_0)^{2/3}$ and $B_{cr} = 2m^2c^3/3e\hbar \approx 2.94 \cdot 10^{13}$ G.

5.6 Astrophysical implications

In this section we explore possible realizations of the synchrotron and curvature regimes, as well as transitions between these two modes of radiation (the synchro-curvature regime) in the context of three specific astrophysical scenarios. Namely below we discuss the radiation of electrons and positrons in the pulsar magnetosphere for the outer gap and polar cap models, and the radiation of protons at their acceleration in the vicinity of a supermassive black hole.

5.6.1 Outer Gap

The high energy gamma radiation from pulsars is widely believed to be produced in the outer gap of the pulsar magnetosphere [122, 126, 127]. Here we present the results of our calculations of radiation of electrons (positrons) in the dipole magnetic field at the location of the outer gap. The position of the outer gap was assumed along the last open field line which is determined by the inner boundary located at the null surface where the Goldreich-Julian charge density is zero, and by the outer boundary taken on the surface of the light cylinder. We adopt the parameters of the Crab pulsar: the radius of the star $R_* = 10^6$ cm, the rotation period $P = 33.5$ ms, and the magnetic field at the pole $B_* = 10^{12}$ G. We consider non-aligned pulsar with an angle of $\pi/4$ between the rotational axis and the magnetic dipole axis. The particle initial position is set at the distance $r_{init} = 0.5R_{lc}$ from the null surface along the last open field line, where R_{lc} is the radius of the light cylinder. During the numerical calculations, the particle is followed up to the intersection with the light cylinder. For the Crab parameters these conditions correspond to $\theta_0 = 51.5^\circ$, $R_0 = 1.2 \cdot 10^8$ cm, $B_0 = 5.6 \cdot 10^5$ G, and $R_{lc} = 1.6 \cdot 10^8$ cm,

where θ_0 is the polar angle relative to the magnetic dipole axis.

The spectra and the radiation regimes have been studied for different initial directions and Lorenz factors of electrons. The resulting spectra are shown in Fig. 5.1. The complementary plots in Figs. 5.2, 5.3, and 5.4 demonstrate the time-evolution of the value of q -parameter (blue lines, right scale) and the Lorenz factor normalized the initial Lorenz factor. The local behaviour of the q -parameter agrees well with Eq. (5.16) obtained from the local solution. As discussed above, the oscillations caused by the particle gyration are within the bandwidth of ≤ 2 . The complementary plots allow us to observe simultaneously the energy lose rate and the regime of the radiation presented by the value of the q -parameter. If the energy loss rate is low, the rarefied output of the points produces intermittent curves for the q -parameter.

It is interesting to examine the statement that the particle moving along drift trajectory yields minimum intensity of radiation and produces less energetic photons. To do this, the initial velocity is deflected by the angle β_D from the magnetic field line towards the binormal vector. The corresponding cumulative (integrated along trajectory) energy spectra of radiation are shown in Fig. 5.1. The complementary plots are shown in Fig. 5.2. We can see that indeed for the initial Lorenz factors $\gamma_0 = 10^6$ and $\gamma_0 = 10^7$ the radiation is less energetic compared to other cases and the rates of energy losses are minimal as well (compare with corresponding plots in Figs. 5.3 and 5.4).

The situation however is different for larger initial Lorentz factors; see the curves corresponding to $\gamma_0 = 5 \cdot 10^7$ and $\gamma_0 = 10^8$. It is seen that for the initial direction along the drift trajectory the radiation spectra extend to higher energies than in the case of the initial direction along the magnetic field. This can be explained by the very intensive energy losses occurring even before the particle has made the first gyration (the first oscillation of q -parameter). During this time $q \approx 1$ for the initial direction along the drift trajectory and $q \approx 0$ for the initial direction along the magnetic field. Eqs. (5.18)-(5.19) show that larger values of q give a more energetic radiation. Correspondingly, more energetic radiation is produced in the case of the initial direction along the drift trajectory. However, after many gyrations the energy losses in the case of the initial direction along drift trajectory become, as expected, less intensive compared to the case of the initial direction along magnetic field line.

We call the attention of the reader to the regimes of the radiation demonstrated by curves in Fig. 5.2. For $\gamma_0 = 10^6$ and $\gamma_0 = 10^7$, the q -parameter equals unity indicating that the radiation proceeds in the curvature regime. However $q = 1$ is not exact as it is demonstrated for $\gamma_0 = 10^7$ where the scale for q -parameter slightly oscillates around unity. These small oscillations correspond to the fine gyration around the drift trajectory. As discussed above (see Eq. 5.23) the presence of such fine perpendicular motions

does not influence on the applicability limits.

In the cases $\gamma_0 = 5 \cdot 10^7$ and $\gamma_0 = 10^8$ the q -parameter has more complex behaviour. The increase at the beginning is defined mostly by the fast energy losses. The decrease is defined by the combination of several factors such as the reduction of the magnetic field strength and the change of its curvature. The increase of q -parameter indicates that the radiation occurs in the synchro-curvature or the synchrotron regimes when the radiation due to curvature of the magnetic field line is less important (for $\gamma_0 = 5 \cdot 10^7$) or simply negligible (for $\gamma_0 = 10^8$). According to Eq. (5.19), the energy of the radiation maximum scales as $\sim \gamma^3 q$. The q -parameter reaches the maximum when the considerable amount of energy has been lost. Therefore, in spite of large q , the peak of radiation shifts towards low energies and does not affect the cumulative spectrum. The interesting feature can be seen at first moments when the energy oscillates with q -parameter and the minimums of q -parameter correspond to flatter parts of the Lorenz factor evolution curve.

The radiation spectra of electrons launched along the magnetic field line are slightly more energetic except for $\gamma_0 = 5 \cdot 10^7$ and $\gamma_0 = 10^8$. The reason is the same as discussed above. Initially, the radiation for $\gamma_0 = 10^6$ and $\gamma_0 = 10^7$ is in transition regime, although for $\gamma_0 = 10^6$ the most of the energy is lost in the curvature regime which occurs fast. Therefore the spectrum in this case almost coincides with the spectrum for the initial direction along the drift trajectory. For $\gamma_0 = 10^7$ the most of the energy is lost in the transition regime, thus the spectrum is shifted to higher energies by $q \approx 2$.

For illustration of the effect related to initial pitch angles larger than β_D , we show the case of initial direction deflected at the angle $10\beta_D$ from the magnetic field line towards the direction opposite to the normal vector. The corresponding spectra indicated in Fig. 5.1 by dash-dotted lines are shifted towards higher energies. Although the q -parameter (Fig. 5.4) reaches large values, the most of the energy is lost at initial stages at $q \approx 10$. Thus the spectra are shifted by $q \approx 10$ compared to the curvature radiation spectra.

We should note that the energy spectra of radiation produced in all regimes contain an exponential cut-off at highest energies similar to the spectrum of the small-angle synchrotron radiation. However, since the radiation spectrum is very sensitive to the pitch-angle, a population of electrons with similar energies but different angles can result in a superposition spectrum with a less abrupt cut-off. The condition for realization of such a spectrum is that the distribution of electrons over pitch-angles around zero angle should be wider than β_D .

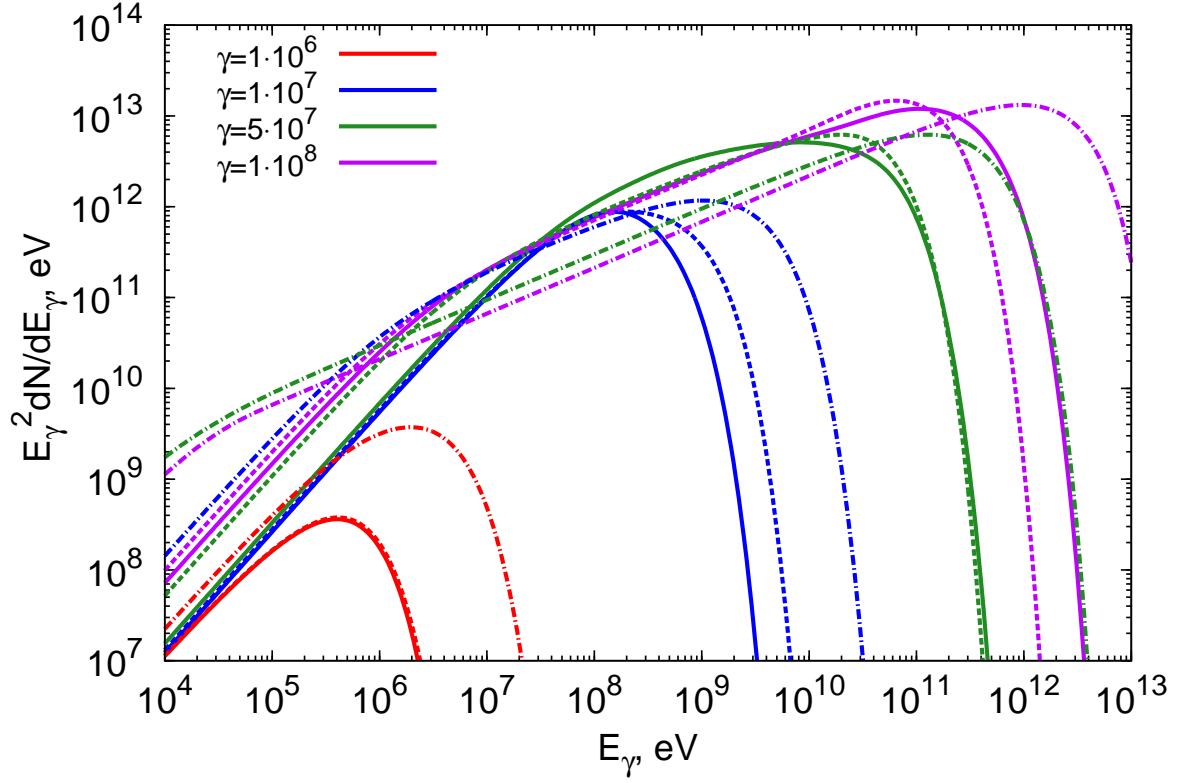


Figure 5.1: The cumulative (integrated along trajectory) radiation spectra of electrons calculated for the outer gap model of the pulsar magnetosphere. The curves are obtained for different initial Lorentz factors of electrons $\gamma = 10^6, 10^7, 5 \times 10^7, 10^8$, and for different initial directions relative to the magnetic field lines: along the drift trajectory (solid lines), along the magnetic field line (dashed lines), and at pitch angle $\alpha = 10\beta_D$ in the meridional plane opposite to the normal vector of magnetic field lines (dashed-dotted lines).

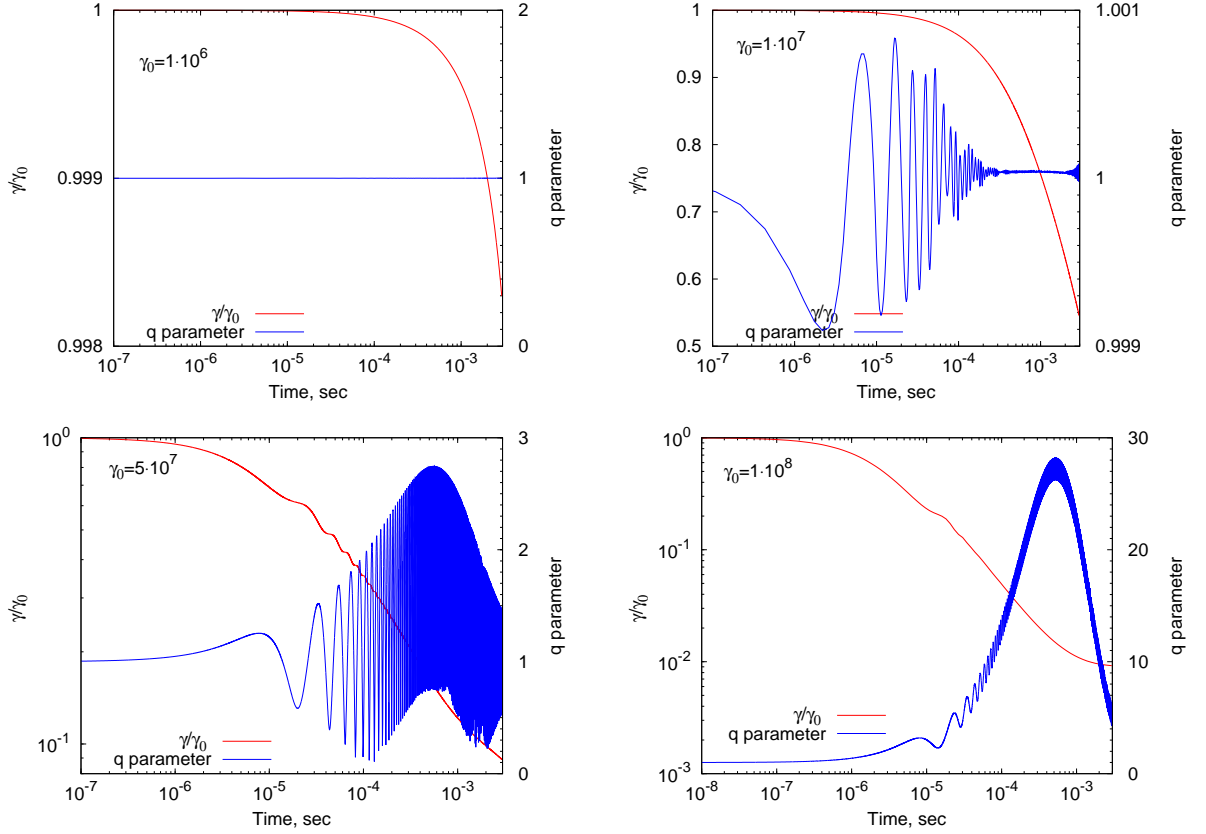


Figure 5.2: Time evolution of the q -parameter and the electron Lorentz factor in the outer gap model (complementary to Fig. 5.1). Four panels correspond to the initial Lorentz factor of electrons $\gamma = 10^6, 10^7, 5 \times 10^7, 10^8$ and their initial direction along the drift trajectory.

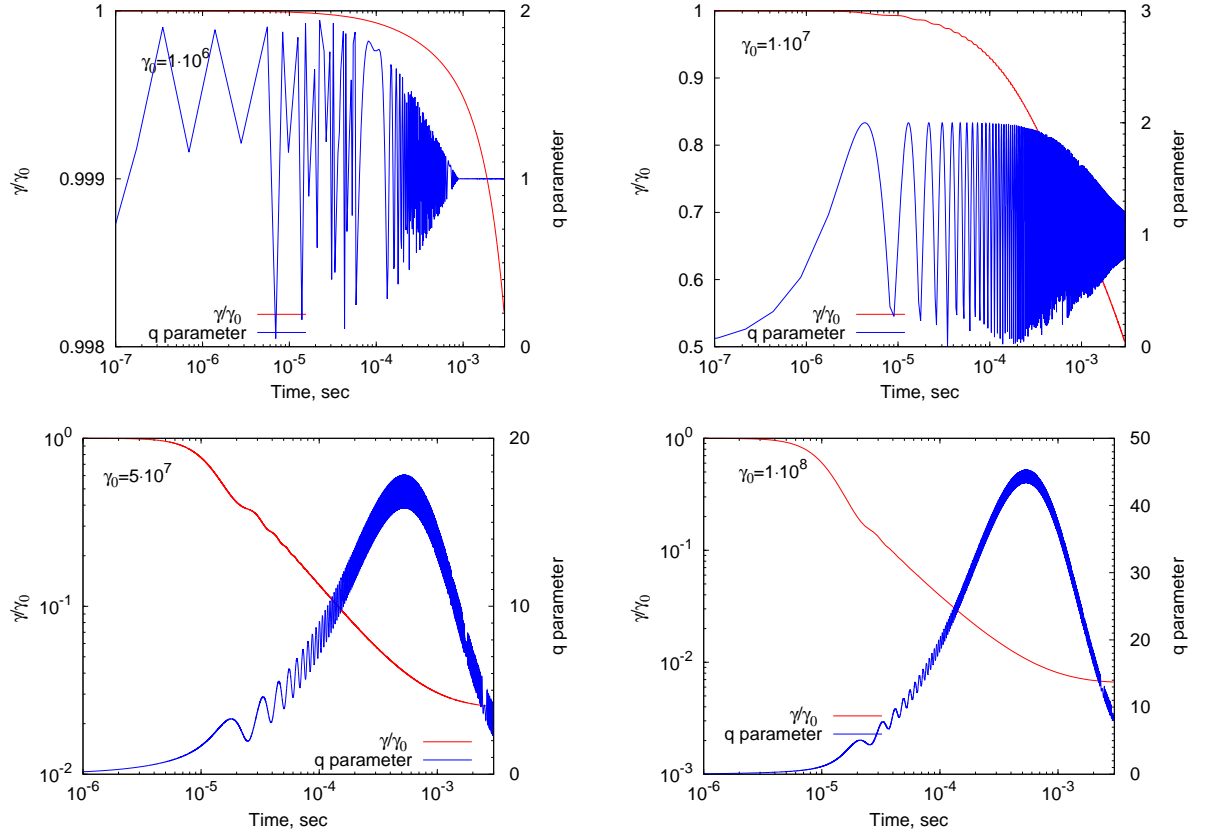


Figure 5.3: The same as in Fig.5.2, but for the initial direction of electrons along the magnetic field line.

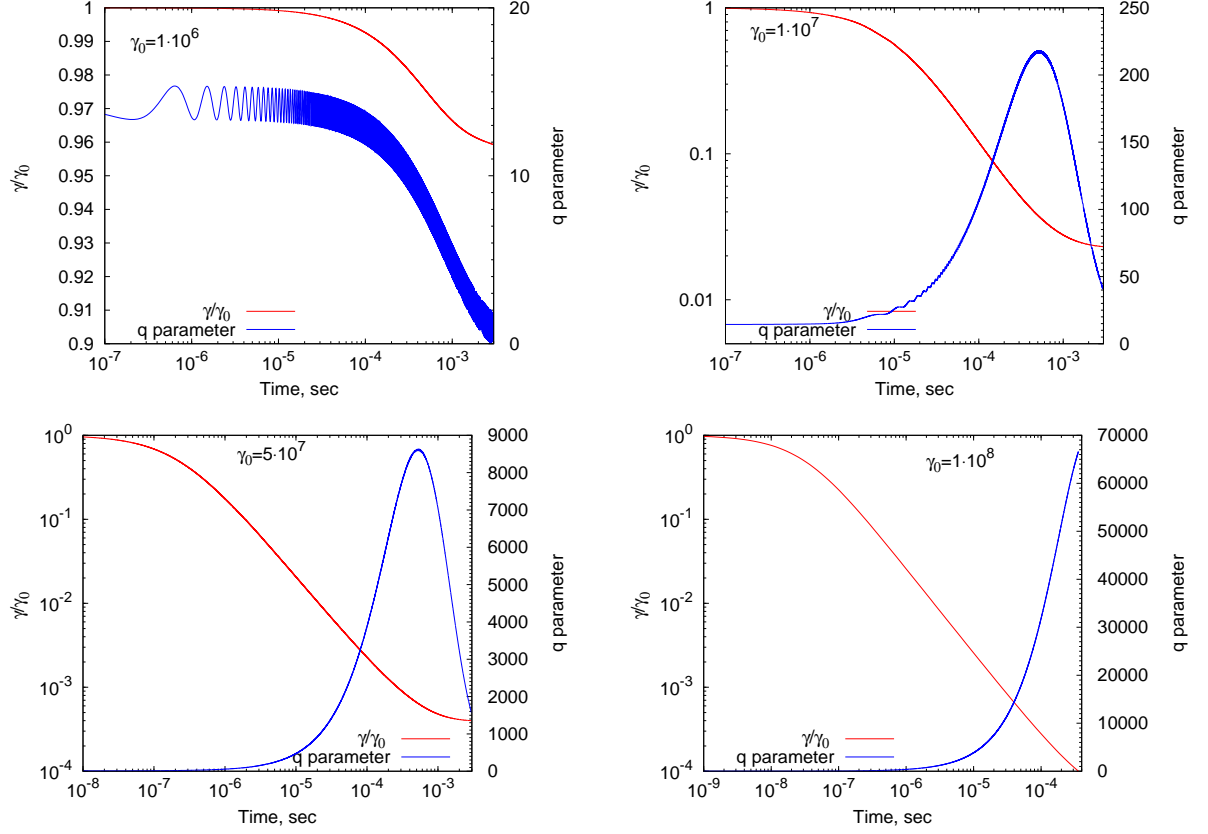


Figure 5.4: The same as in Fig.5.2, but for the initial direction of electrons at an angle $10\beta_D$.

5.6.2 Polar Cap

In the polar cap model electrons radiate in the region located close to the surface of the neutron star where the magnetic field is much stronger than in the outer gap model, approaching to $B \approx 10^{12}$ G. This results in much faster damping of the perpendicular component of motion. The very small drift velocity β_D implies that the drift trajectory and the magnetic field line almost coincide, thus even a small deflection from the magnetic field line produces radiation quite different from the curvature radiation. However, the transition to the curvature radiation regime occurs very fast. In the curvature regime, electrons radiate more energetic photons than in the outer gap model. But the curvature of the magnetic field lines in the polar cap model with $\theta_0 \sim 1^\circ$ is only an order of magnitude larger than in the outer gap since the curvature of the dipole magnetic field scales as $\sim \sin \theta / r$. Correspondingly, the maximum energy of curvature radiation at the polar cap is only an order of magnitude higher than in the outer gap.

The energy spectra of radiation calculated for the polar cap model are shown in Fig. 5.5. The complementary plots for the evolution of the q -parameter and the electron Lorentz factor are presented in Figs. 5.6, 5.7, and 5.8. The initial position of the particle is $R_0 = 10^6$ cm, and $\theta_0 = 3^\circ$. The spectra indicated by solid lines correspond to the case when the initial direction of particle is along magnetic field line. In this case the radiation is in the curvature regime. But at the initial stage, the radiation proceeds in a very fast synchro-curvature regime, but abruptly turns to the regime with $q \approx 1$ and fast oscillations caused by fine gyrations.

The abrupt change of the regimes leads to an interesting feature in the cumulative spectra for the case of an initial pitch angle $\alpha_0 = 1/\gamma_0$ (dashed lines). Because of small changes in energy and fast change of the q -parameter, the energy spectra consist of two peaks. The peak at higher energies is produced by synchrotron radiation ($q \gg 1$, see Fig. 5.7), while the lower energy peak corresponds to curvature radiation regime. The double-peak structure disappears for large initial pitch angles. For example, for the pitch angle $100/\gamma_0$ the transition to the curvature regime is very fast, and the electron enters into this regime with dramatically reduced Lorentz factor. Thus the peak of the curvature radiation not only is shifted to smaller energies, but also is too weak to be seen in the cumulative spectrum¹.

In very strong magnetic fields, namely when the parameter $\chi = B\gamma \sin \alpha / B_{cr} \geq 1$, the radiation is produced in the quantum regime. Let's assume that the initial pitch angle is inverse proportional to the initial Lorentz factor, $\alpha_0 = a/\gamma_0$. This makes the

¹Note that the pitch angle $100/\gamma_0$ which we treat as 'large', still is extremely small, $\sim 2(\gamma_0/10^7)^{-1}$ arcsec.

condition of radiation in the quantum regime independent on γ_0 :

$$\chi = \frac{B}{B_{cr}} \gamma \sin \alpha_0 = \frac{1 \cdot 10^{12} G}{2.94 \cdot 10^{13} G} a \approx 3.4 \cdot 10^{-2} a. \quad (5.31)$$

Thus, at the initial pitch angle with $a > 30$, the electrons radiate in quantum regime. Dash-dotted lines in Fig. 5.5 present radiation spectra for the initial pitch-angles $\alpha_0 = 100/\gamma_0$. Note that in the quantum regime almost the entire energy of the parent electron is transferred to the radiated photon. Thus we should expect abrupt cutoff in the radiation spectra. This effect is clearly seen in Fig. 5.5 (dot-dashed curves corresponding to the initial pitch angle $\alpha_0 = 100/\gamma_0$). The gamma rays produced in the quantum regime are sufficiently energetic to be absorbed in the magnetic field through the e^+e^- pair production. This will lead to the development of an electromagnetic cascade in the magnetic field. The spectrum of cascade gamma-rays that escape the pulsar magnetosphere will be quite different from the spectra shown in Fig. 5.5.

5.6.3 Protons in the Black Hole magnetosphere

The acceleration of the protons to ultrahigh energies in the potential gap of the spinning supermassive black hole should be accompanied by curvature radiation in the magnetic field which threads the black hole ([128], [26]). Here we briefly examine the radiation regimes and the gamma ray spectra of accelerated protons produced in this model. As before, we consider the radiation in the dipole magnetic field adopting the following (typical for a SMBH) parameters $B_* = 10^4$ G and $R_* = 10^{14}$ cm. The initial position of the particle is set at the polar angle $\theta_0 = 5^\circ$ relative to the magnetic dipole axis.

The larger (compared to electron) mass of proton leads to the larger drift velocity β_D . Therefore the spectra and the radiation regimes in the case of protons are less sensitive to the initial direction of motion. The radiation of protons deviates from the curvature radiation when the perpendicular component of proton's Lorentz factor exceed

$$\gamma_\perp = \gamma \beta_D = \frac{m_p c^2 \gamma^2}{e B r_0} = 2.7 \cdot 10^7 \left(\frac{\gamma}{10^{10}} \right)^2. \quad (5.32)$$

This is larger by the factor of $m_p/m_e \approx 2 \cdot 10^3$ compared to the same condition for electrons. It is interesting to note that for the same Lorenz factor, in the synchrotron regime protons radiates much weaker than electrons, whereas in the curvature regime they radiate equally.

The radiation spectra of protons with different initial pitch angles are presented in Fig. 5.9. The smallest angle α_0 is close to β_D , and the proton radiates in the synchro-

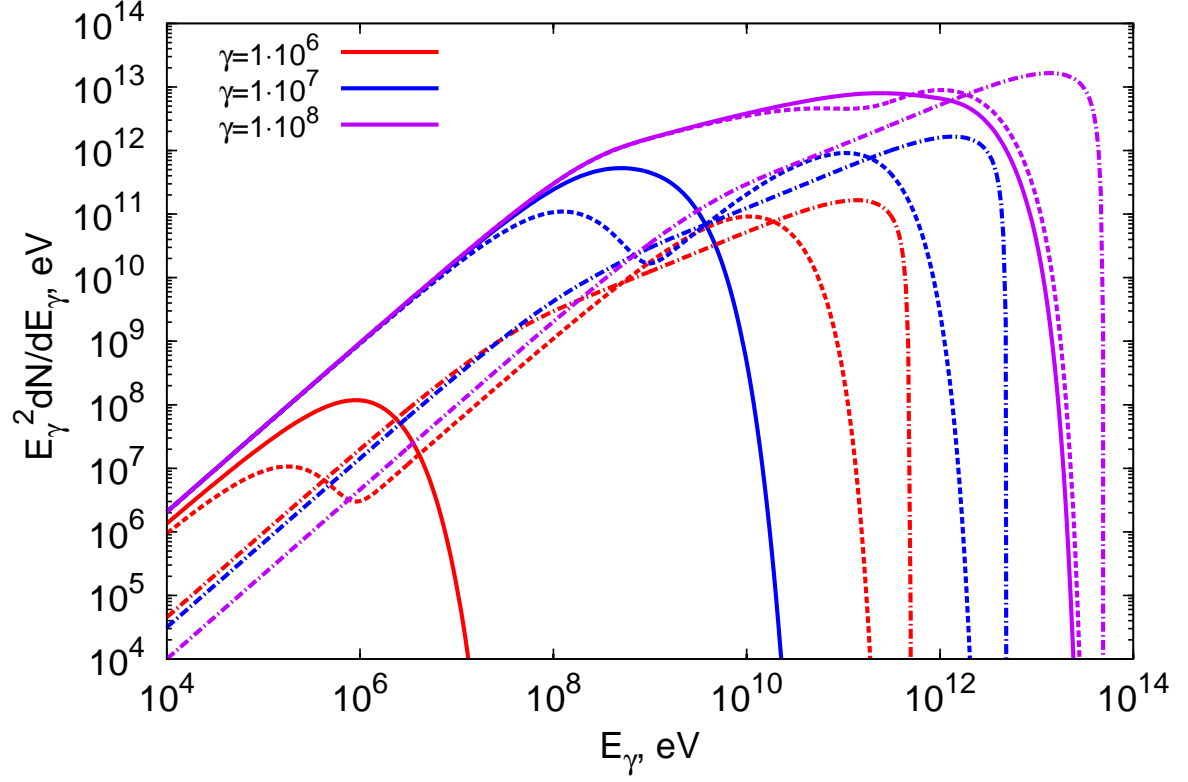


Figure 5.5: The cumulative (integrated along trajectory) radiation spectra of electrons calculated for the outer gap model of the pulsar magnetosphere. The curves are obtained for different initial Lorentz factors of electrons $\gamma = 10^6, 10^7, 10^8$, and for different initial directions relative to the magnetic field lines: along the magnetic field line (solid lines), and for two pitch angles $1/\gamma_0$ (dashed lines) and $100/\gamma_0$ (dashed-dotted lines).

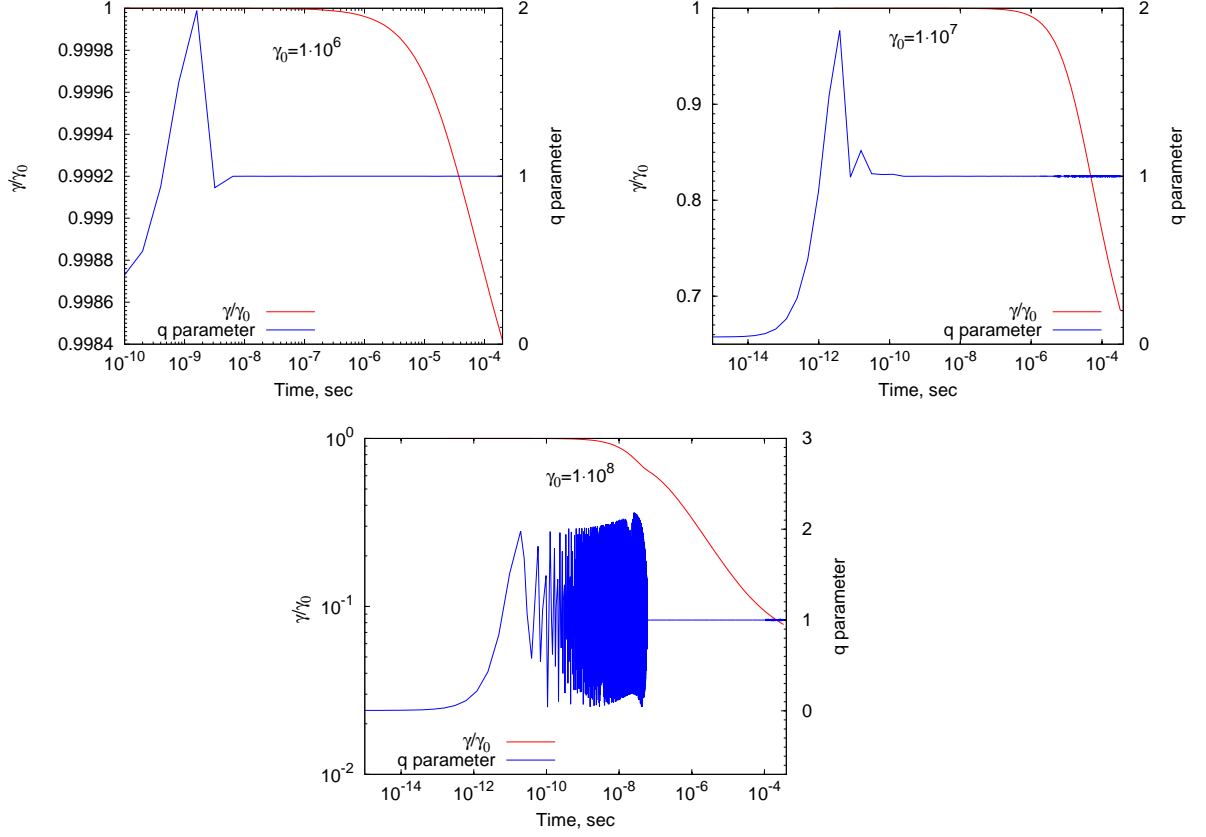


Figure 5.6: Time evolution of the q -parameter and the electron Lorentz factor in the outer gap model (complementary to Fig. 5.5). Three panels correspond to the initial Lorentz factor of electrons $\gamma = 10^6, 10^7, 10^8$ and their initial direction along the magnetic field line.

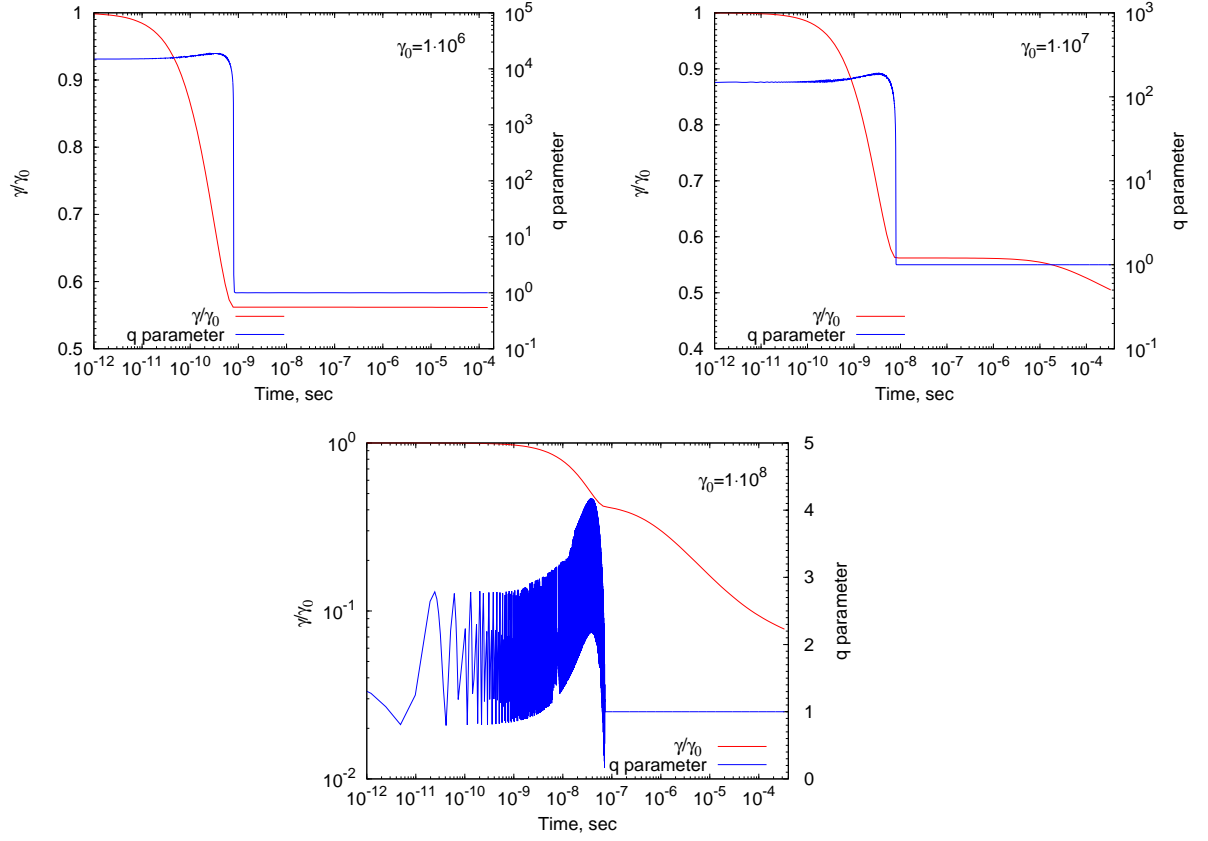


Figure 5.7: The same as in Fig.5.6, but for the initial direction of electrons at pitch angle $1/\gamma_0$.

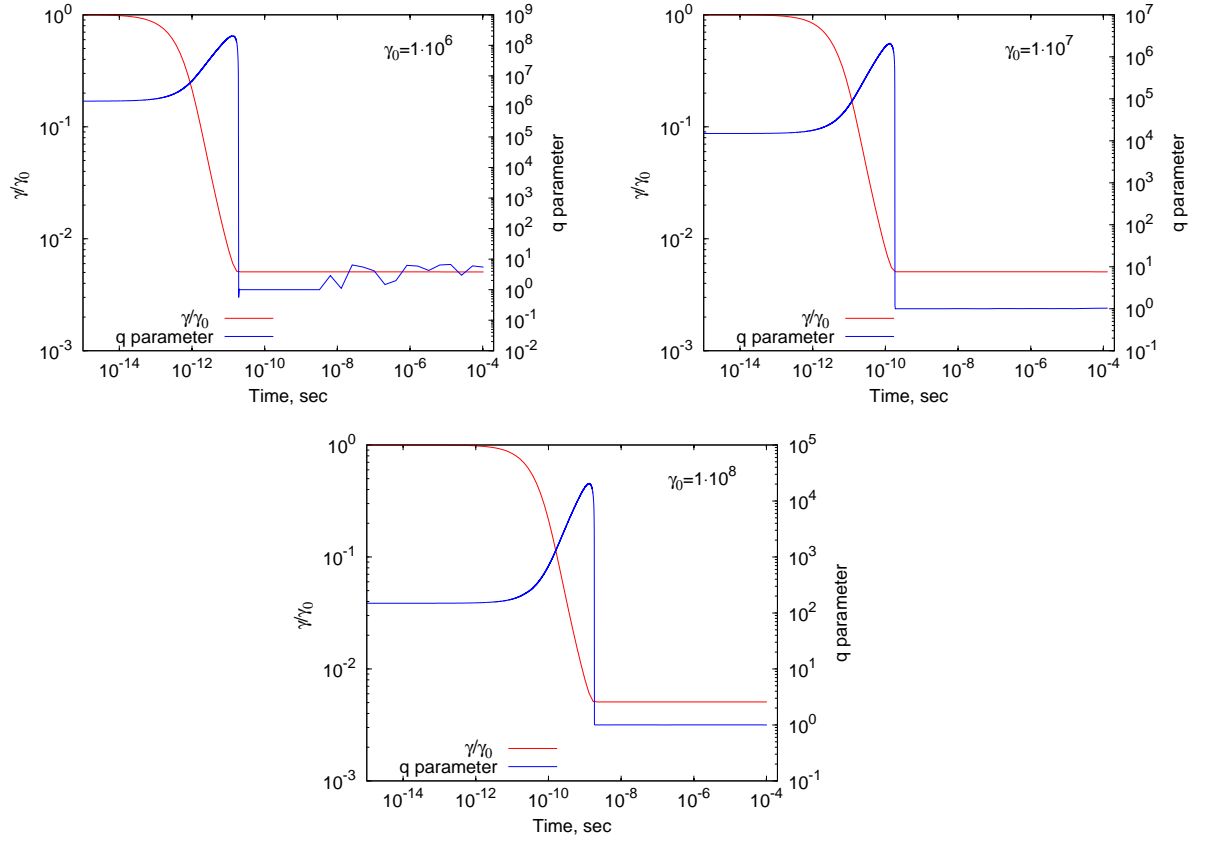


Figure 5.8: The same as in Fig.5.6, but for the initial direction of electrons at pitch angle $100/\gamma_0$.

curvature regime (solid lines). Because of high energy the gyration period is large, and in the case of $\gamma_0 = 10^{10}$ the particle makes only several gyrations before escaping the region with high magnetic field (see Fig. 5.11). After that, the proton radiates with a very low rate, and the q -parameter approaches zero. In the case of $\gamma_0 = 10^9$, the proton gyrates more frequently (see Fig. 5.10) and there is seen more pronounced tendency of q approaching to zero. The other curves correspond to the initial pitch angles $10\alpha_0$ and $100\alpha_0$. The spectra are shifted towards higher energies by the same factors of $q \approx 10$ and $q \approx 100$. Accordingly, for the Lorentz factor $\gamma_0 = 10^{11}$ which is not shown in figures, the proton will radiate predominantly in the curvature regime and the spectrum will be shifted by a factor of $(10^{11}/10^{10})^3 = 1000$ relative to the curvature spectrum of the proton with initial Lorentz factor $\gamma_0 = 10^{10}$. Despite the small energy losses relative to the initial energy, the amount of the radiated energy is quite large. As in the case of the pulsar polar cap model, for the chosen parameters the curvature radius of the magnetic field lines is larger by an order of magnitude compared to the gravitational radius of the black hole which usually is taken for evaluation of curvature radius. It yields smaller energy losses and increase the maximum Lorentz factor of acceleration compared to the case when the gravitational radius of the black hole is used as a curvature radius. To be more specific, the maximum Lorentz factor of a particle in radiative-loss limited regime scales with curvature radius R_c as $\sqrt{R_c/R_*}$ ([26], [128]).

5.7 Summary

The radiation of relativistic particles in a strong curved magnetic field is of a great astrophysical interest, in particular in the context of magnetospheric gamma-ray emission of rotation-powered pulsars. In these objects with very strong magnetic fields, the radiation proceeds in quite complex regimes, so it cannot be reduced merely to the consideration of the nominal synchrotron and curvature channels. For proper understanding of these radiation regimes and the transitions between them, the accurate treatment of the particle trajectory is a key issue. It can be done by solving the equations of motion taking into account energy losses of charged particles. In this chapter we followed this approach to explore the radiation features of ultrarelativistic particles in a dipole field which is a good approximation for the magnetic field structure in compact astrophysical objects. The accurate numerical solutions for the test particle trajectory allowed us to trace the radiation regimes and calculate self-consistently the radiation spectrum without any *a priori* assumption concerning the radiation regime.

We demonstrated that even small deflections of the initial particle motion from the magnetic field lines may result in a radiation spectrum quite different from the spectrum

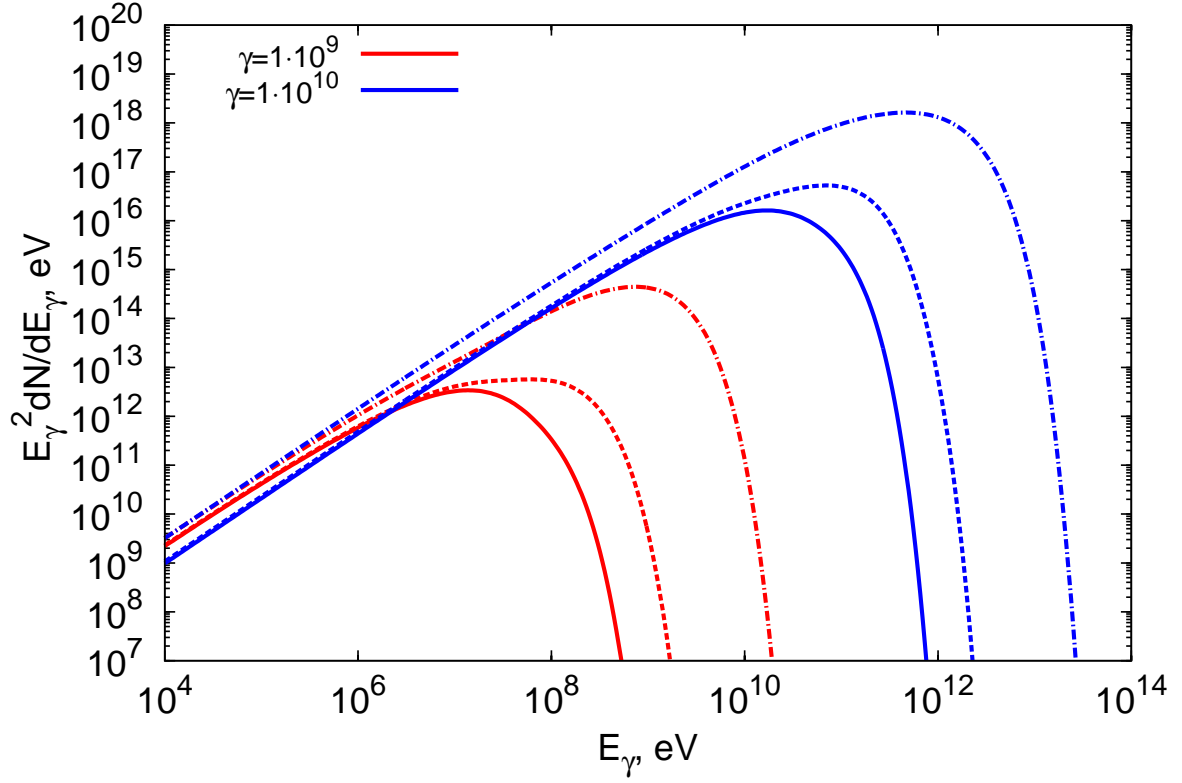


Figure 5.9: The cumulative (integrated along trajectory) radiation spectra of protons in the magnetic field of rotating supermassive black hole. The chosen parameters are described in the text. The spectra correspond to two different Lorentz factors and three different initial pitch angles relative to the magnetic field lines: 10^{-4} (solid), 10^{-3} (dashed), 10^{-2} (dash-dotted) radian for $\gamma_0 = 10^9$ (red) and 10^{-3} (solid), 10^{-2} (dashed), 10^{-1} (dash-dotted) radian for $\gamma_0 = 10^{10}$ (blue).

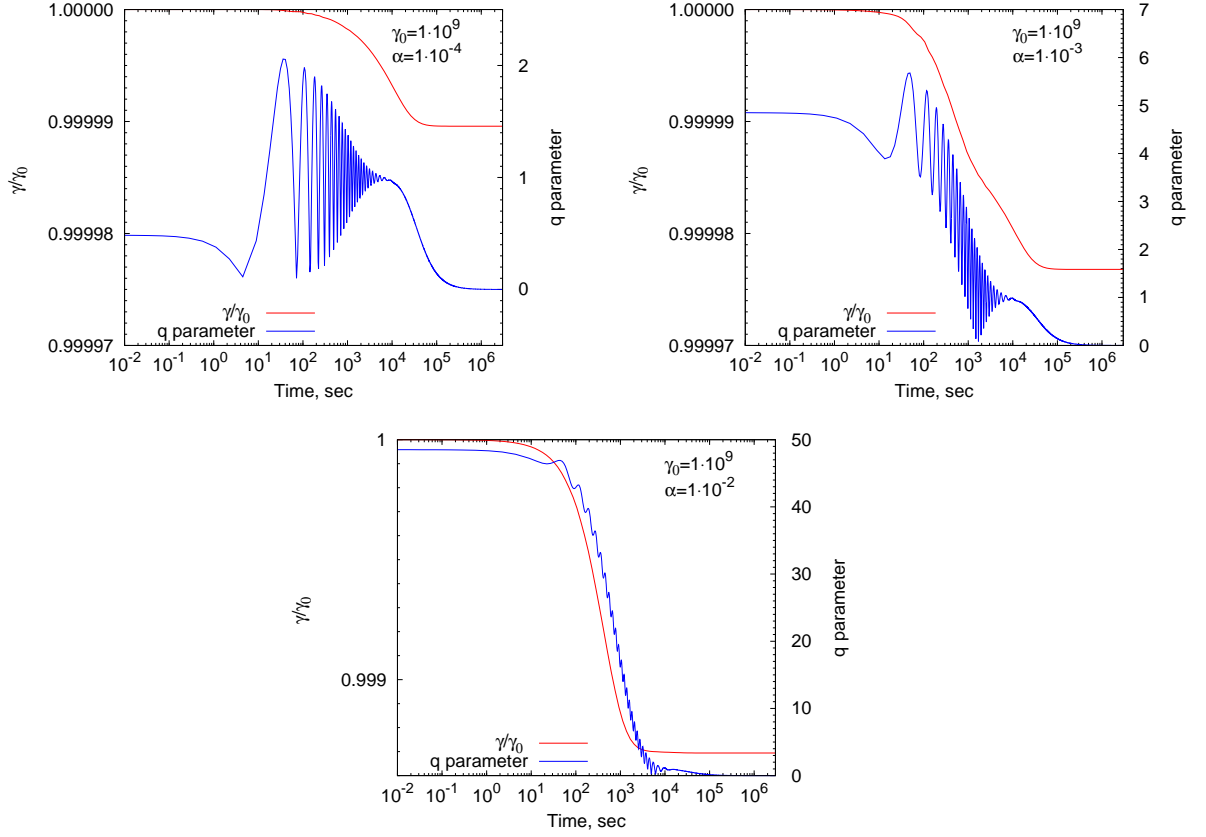


Figure 5.10: Time-evolution of the Lorentz factor and the q -parameter in the magnetic field of a supermassive black hole with the initial Lorentz factor of protons $\gamma_0 = 10^9$ and their initial pitch angles $\alpha = 10^{-4}$, 10^{-3} , and 10^{-2} .

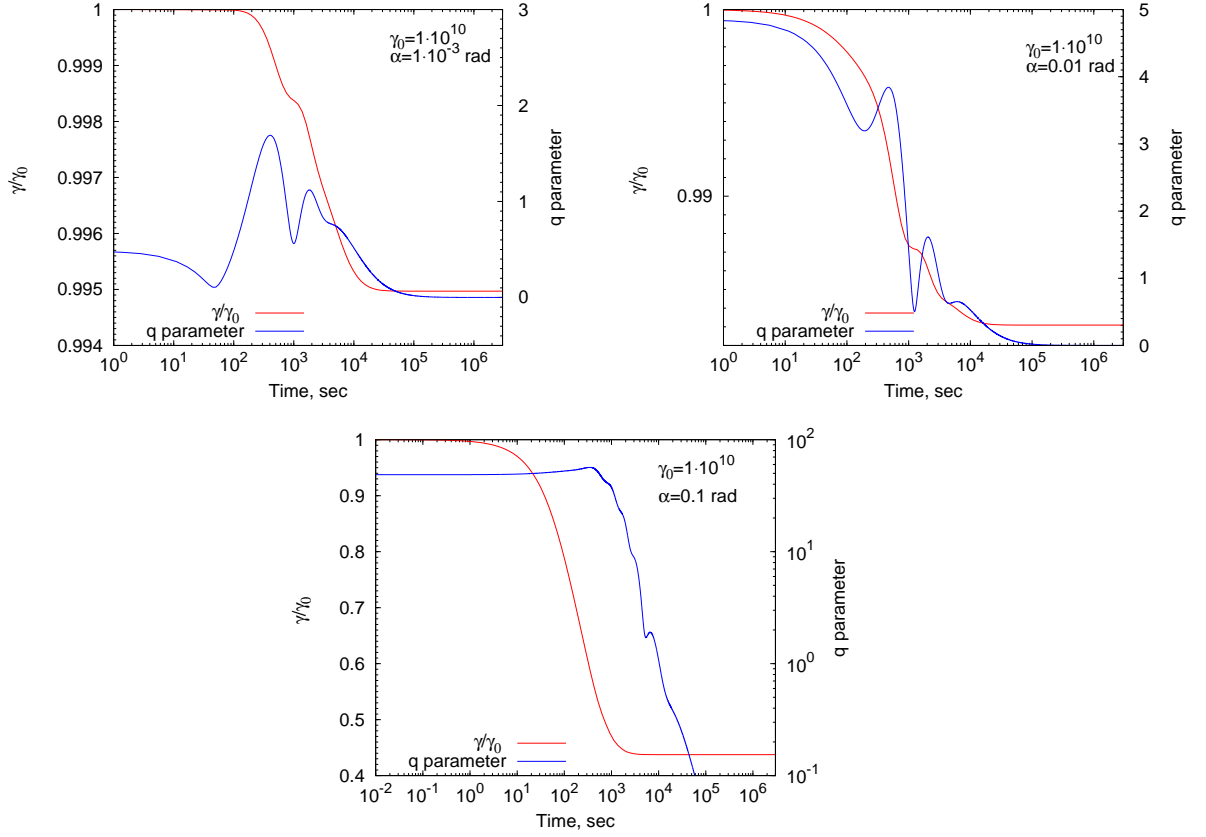


Figure 5.11: Time-evolution of the Lorentz factor and the q -parameter in the magnetic field of a supermassive black hole with the initial Lorentz factor of protons $\gamma_0 = 10^{10}$ and their initial pitch angles $\alpha = 10^{-3}$, 10^{-3} , and 10^{-1} .

the curvature radiation. For any initial pitch angle, the particle tends, while losing its energy, to turn to the curvature radiation regime and to move strictly along drift trajectory (although never can achieve the latter). In principle, the fast increase of curvature of the magnetic field lines can turn the regimes in inverse order.

In different environments (or different positions relative to magnetic dipole) the transition to the curvature radiation regime proceeds with different rate. While in the polar cap model the transition occurs almost instantly, in the outer gap the transition could last so long that the particle would not turn to the curvature regime while passing the gap. The spectrum of the radiation becomes very different from the spectrum of the curvature radiation if the pitch angle of the particle is greater than drift speed $\beta_D = v_D/c$, and quite similar if it is smaller than β_D . For the typical parameters of the polar cap model, $\beta_D = 2.2 \cdot 10^{-9}(\gamma/10^8)$. This implies that the even tiny deflection from the magnetic field line leads to the spectrum different from the curvature radiation spectrum.

Significant deviations of the radiation spectra from the nominal curvature radiation spectrum is expected also in the outer gap model. The particles do not move along magnetic field lines but gyrate around drift trajectory. This results in a different (more “energetic”) spectrum from the conventional curvature radiation spectrum. In the outer gap model, electrons with initial direction along magnetic field line start to radiate in the synchro-curvature regime, when the both the curvature of the magnetic field and its strength play equally important role. The effect is quite significant at large Lorentz factors of electrons, $\gamma \geq 10^7$.

Finally, we demonstrate the strong impact of the initial pitch angle on the radiation spectrum in the scenario of acceleration and motion of ultrahigh energy protons in the magnetosphere of a supermassive black hole.

Appendix: Energy losses in the quantum regime

In a very strong magnetic field, the ultrarelativistic electrons can radiate in the quantum regime, provided that

$$\chi = \frac{B}{B_{cr}} \gamma \sin \alpha \gtrsim 1, \quad (5.33)$$

where $B_{cr} = \frac{2m^2c^3}{3e\hbar} \approx 2.94 \cdot 10^{13}$ G. The energy lose rate can be written in the form [129, 125]

$$\left| \frac{dE}{dt} \right| = \frac{e^2 m^2 c^3}{\sqrt{3} \pi \hbar^2} \overline{H}(\chi), \quad (5.34)$$

where

$$\overline{H}(\chi) = \int_0^1 H(\tau, \chi) d\tau, \quad (5.35)$$

and

$$H(\tau, \chi) = \chi \left[(1 - \tau)F(x) + x\tau^2 K_{2/3}(x) \right], \quad x = \frac{\tau}{\chi(1 - \tau)}, \quad (5.36)$$

where $K_{2/3}(x)$ is the modified Bessel function of the order $2/3$, $F(x)$ is the emissivity function of the synchrotron radiation (see Eq. 5.20), $\tau = \epsilon/E$, where ϵ is the energy of the radiated photon, E is the energy of the radiating particle.

For calculations it is convenient to express $\overline{H}(\chi)$ in Eq.(5.34) in a simple approximate analytical form. Using asymptotics of this function

$$\begin{aligned} \overline{H}(\chi) &\approx \frac{8\pi\sqrt{3}}{27}\chi^2, \quad \chi \ll 1, \\ \overline{H}(\chi) &\approx \frac{32\pi\sqrt{3}}{243}2^{2/3}\Gamma\left(\frac{2}{3}\right)\chi^{2/3}, \quad \chi \gg 1. \end{aligned} \quad (5.37)$$

we have found the following approximation

$$\overline{H}(\chi) \approx \frac{8\pi\sqrt{3}}{27} \frac{\chi^2}{\left(1 + \frac{3}{4} \frac{(2\chi)^{2/3}}{\sqrt{\Gamma(\frac{2}{3})}}\right)^2} \times \left(1 + \frac{0.52\sqrt{\chi}(1 + 3\sqrt{\chi} - 3.2\chi)}{1 + 0.3\sqrt{\chi} + 17\chi + 11\chi^2}\right) \quad (5.38)$$

The first two terms (before the sign \times) of Eq. (5.38) give right asymptotics at $\chi \ll 1$ and $\chi \gg 1$ and provide an accuracy better than 10% for other values of χ , whereas the inclusion of the last term in the brackets makes the accuracy better than 0.1% for any χ .

The spectrum of the radiation in the quantum regime is expressed as

$$F_q(x, \tau) = (1 - \tau)F(x) + \tau^2 x K_{2/3}(x), \quad x = \frac{\tau}{1 - \tau} \frac{E}{\epsilon_c}, \quad (5.39)$$

where $\epsilon_c = \frac{3e\hbar B \sin \alpha}{2mc} \gamma^2$ is the characteristic energy of the emitted photon. To use this function in Eq. (5.18), the ϵ_c should be changed to $\hbar\omega_*$. An analytical approximation of this function can be obtained using the approximation for emissivity function of the synchrotron radiation [17]

$$F(x) \approx 2.15x^{1/3}(1 + 3.06x)^{1/6} \frac{1 + 0.884x^{2/3} + 0.471x^{4/3}}{1 + 1.64x^{2/3} + 0.974x^{4/3}} e^{-x}, \quad (5.40)$$

and

$$xK_{2/3}(x) \approx 1.075x^{1/3}(1 + 3.72x)^{1/6} \frac{1 + 1.58x^{2/3} + 3.97x^{4/3}}{1 + 1.53x^{2/3} + 4.25x^{4/3}} e^{-x}. \quad (5.41)$$

Both approximations provide an accuracy better than 0.2% for any value of the argument x .

Bibliography

- [1] R. U. Abbasi et al. First Observation of the Greisen-Zatsepin-Kuzmin Suppression. *Physical Review Letters*, 100(10):101101, March 2008.
- [2] R. U. Abbasi et al. Measurement of the flux of ultra high energy cosmic rays by the stereo technique. *Astroparticle Physics*, 32:53–60, August 2009.
- [3] J. Abraham et al. Observation of the Suppression of the Flux of Cosmic Rays above 4×10^{19} eV. *Physical Review Letters*, 101(6):061101, August 2008.
- [4] Pierre Auger Collaboration. The surface detector system of the Pierre Auger Observatory. *Nuclear Instruments and Methods in Physics Research A*, 586:409–420, March 2008.
- [5] The Pierre Auger Collaboration. The Fluorescence Detector of the Pierre Auger Observatory. *ArXiv e-prints*, July 2009.
- [6] C. Bonifazi and Pierre Auger Collaboration. The angular resolution of the Pierre Auger Observatory. *Nuclear Physics B Proceedings Supplements*, 190:20–25, May 2009.
- [7] J. Abraham et al. Measurement of the Depth of Maximum of Extensive Air Showers above 10^{18} eV. *Physical Review Letters*, 104(9):091101, March 2010.
- [8] R. U. Abbasi et al. Indications of Proton-Dominated Cosmic-Ray Composition above 1.6 EeV. *Physical Review Letters*, 104(16):161101, April 2010.
- [9] K. Kotera and A. V. Olinto. The Astrophysics of Ultrahigh-Energy Cosmic Rays. *Annu. Rev. Astron. Astrophys.*, 49:119–153, September 2011.
- [10] M. Lemoine and E. Waxman. Anisotropy vs chemical composition at ultra-high energies. *J. Cosmol. Astropart. Phys.*, 11:9, November 2009.
- [11] P. Blasi and A. V. Olinto. Magnetized local supercluster and the origin of the highest energy cosmic rays. *Phys. Rev. D*, 59(2):023001, January 1999.

- [12] E. Waxman and J. Miralda-Escude. Images of Bursting Sources of High-Energy Cosmic Rays: Effects of Magnetic Fields. *Ap. J. Letters*, 472:L89, December 1996.
- [13] G. Sigl, F. Miniati, and T. A. Enßlin. Ultrahigh energy cosmic ray probes of large scale structure and magnetic fields. *Phys. Rev. D*, 70(4):043007, August 2004.
- [14] K. Dolag, D. Grasso, V. Springel, and I. Tkachev. Constrained simulations of the magnetic field in the local Universe and the propagation of ultrahigh energy cosmic rays. *J. Cosmol. Astropart. Phys.*, 1:9, January 2005.
- [15] N. Globus, D. Allard, and E. Parizot. Propagation of high-energy cosmic rays in extragalactic turbulent magnetic fields: resulting energy spectrum and composition. *Astr. Ap.*, 479:97–110, February 2008.
- [16] K. Kotera and M. Lemoine. Inhomogeneous extragalactic magnetic fields and the second knee in the cosmic ray spectrum. *Phys. Rev. D*, 77(2):023005, January 2008.
- [17] F. A. Aharonian, S. R. Kelner, and A. Y. Prosekin. Angular, spectral, and time distributions of highest energy protons and associated secondary gamma rays and neutrinos propagating through extragalactic magnetic and radiation fields. *Phys. Rev. D*, 82(4):043002, August 2010.
- [18] T. Stanev. Ultra-High-Energy Cosmic Rays and the Large-Scale Structure of the Galactic Magnetic Field. *ApJ*, 479:290, April 1997.
- [19] K. Kotera, D. Allard, and M. Lemoine. Detectability of ultrahigh energy cosmic-ray signatures in gamma-rays. *Astr. Ap.*, 527:A54, March 2011.
- [20] J. Einasto. Large scale structure. *New Astronomy Reviews*, 45:355–372, March 2001.
- [21] A. M. Beck, M. Hanasz, H. Lesch, R.-S. Remus, and F. A. Stasyszyn. On the magnetic fields in voids. *MNRAS*, 429:L60–L64, February 2013.
- [22] T. Akahori and D. Ryu. Faraday Rotation Measure due to the Intergalactic Magnetic Field. II. The Cosmological Contribution. *ApJ*, 738:134, September 2011.
- [23] D. Ryu, H. Kang, J. Cho, and S. Das. Turbulence and Magnetic Fields in the Large-Scale Structure of the Universe. *Science*, 320:909–, May 2008.
- [24] P. Abreu et al. Update on the correlation of the highest energy cosmic rays with nearby extragalactic matter. *Astroparticle Physics*, 34:314–326, 2010.

- [25] P. Abreu et al. Large-scale Distribution of Arrival Directions of Cosmic Rays Detected Above 10^{18} eV at the Pierre Auger Observatory. *ApJS*, 203:34, December 2012.
- [26] F. A. Aharonian, A. A. Belyanin, E. V. Derishev, V. V. Kocharovsky, and V. V. Kocharovsky. Constraints on the extremely high-energy cosmic ray accelerators from classical electrodynamics. *Phys. Rev. D*, 66(2):023005, July 2002.
- [27] J. W. Cronin. The highest-energy cosmic rays. *Nuclear Physics B Proceedings Supplements*, 138:465–491, January 2005.
- [28] K. Greisen. End to the Cosmic-Ray Spectrum? *Physical Review Letters*, 16:748–750, April 1966.
- [29] G. T. Zatsepin and V. A. Kuz'min. Upper Limit of the Spectrum of Cosmic Rays. *Soviet Journal of Experimental and Theoretical Physics Letters*, 4:78, August 1966.
- [30] D. Allard, N. G. Busca, G. Decerprit, A. V. Olinto, and E. Parizot. Implications of the cosmic ray spectrum for the mass composition at the highest energies. *J. Cosmol. Astropart. Phys.*, 10:33, October 2008.
- [31] S. R. Kelner and F. A. Aharonian. Energy spectra of gamma rays, electrons, and neutrinos produced at interactions of relativistic protons with low energy radiation. *Phys. Rev. D*, 78(3):034013, August 2008.
- [32] V. Berezhinsky, A. Gazizov, and S. Grigorieva. On astrophysical solution to ultra-high energy cosmic rays. *Phys. Rev. D*, 74(4):043005, August 2006.
- [33] A. Mücke, R. Engel, J. P. Rachen, R. J. Protheroe, and T. Stanev. Monte Carlo simulations of photohadronic processes in astrophysics. *Computer Physics Communications*, 124:290–314, February 2000.
- [34] M. Lemoine. Acceleration and propagation of ultrahigh energy cosmic rays. *Journal of Physics Conference Series*, 409(1):012007, February 2013.
- [35] M. Vietri. The Acceleration of Ultra-High-Energy Cosmic Rays in Gamma-Ray Bursts. *ApJ*, 453:883, November 1995.
- [36] E. Waxman. Cosmological Gamma-Ray Bursts and the Highest Energy Cosmic Rays. *Physical Review Letters*, 75:386–389, July 1995.
- [37] M. Milgrom and V. Usov. Possible Association of Ultra-High-Energy Cosmic-Ray Events with Strong Gamma-Ray Bursts. *Ap. J. Letters*, 449:L37, August 1995.

- [38] P. G. Tinyakov and I. I. Tkachev. Deflections of cosmic rays in a random component of the Galactic magnetic field. *Astroparticle Physics*, 24:32–43, September 2005.
- [39] D. Ryu, H. Kang, and P. L. Biermann. Cosmic magnetic fields in large scale filaments and sheets. *Astr. Ap.*, 335:19–25, July 1998.
- [40] A. Neronov and I. Vovk. Evidence for Strong Extragalactic Magnetic Fields from Fermi Observations of TeV Blazars. *Science*, 328:73–, April 2010.
- [41] K. Dolag, M. Kachelriess, S. Ostapchenko, and R. Tomàs. Lower Limit on the Strength and Filling Factor of Extragalactic Magnetic Fields. *Ap. J. Letters*, 727:L4, January 2011.
- [42] F. Tavecchio, G. Ghisellini, L. Foschini, G. Bonnoli, G. Ghirlanda, and P. Coppi. The intergalactic magnetic field constrained by Fermi/Large Area Telescope observations of the TeV blazar 1ES0229+200. *MNRAS*, 406:L70–L74, July 2010.
- [43] A. M. Taylor, I. Vovk, and A. Neronov. Extragalactic magnetic fields constraints from simultaneous GeV-TeV observations of blazars. *Astr. Ap.*, 529:A144, May 2011.
- [44] S. Ando and A. Kusenko. Evidence for Gamma-ray Halos Around Active Galactic Nuclei and the First Measurement of Intergalactic Magnetic Fields. *Ap. J. Letters*, 722:L39–L44, October 2010.
- [45] R. M. Kulsrud and E. G. Zweibel. On the origin of cosmic magnetic fields. *Reports on Progress in Physics*, 71(4):046901, April 2008.
- [46] L. M. Widrow. Origin of galactic and extragalactic magnetic fields. *Reviews of Modern Physics*, 74:775–823, 2002.
- [47] P. P. Kronberg, H. Lesch, and U. Hopp. Magnetization of the Intergalactic Medium by Primeval Galaxies. *ApJ*, 511:56–64, January 1999.
- [48] R. Engel, D. Seckel, and T. Stanev. Neutrinos from propagation of ultrahigh energy protons. *Phys. Rev. D*, 64(9):093010, November 2001.
- [49] K. Kotera, D. Allard, and A. V. Olinto. Cosmogenic neutrinos: parameter space and detectability from PeV to ZeV. *J. Cosmol. Astropart. Phys.*, 10:13, October 2010.

- [50] A. Elyiv, A. Neronov, and D. V. Semikoz. Gamma-ray induced cascades and magnetic fields in the intergalactic medium. *Phys. Rev. D*, 80(2):023010, July 2009.
- [51] W. Essey, O. E. Kalashev, A. Kusenko, and J. F. Beacom. Secondary Photons and Neutrinos from Cosmic Rays Produced by Distant Blazars. *Physical Review Letters*, 104(14):141102, April 2010.
- [52] W. Essey, O. Kalashev, A. Kusenko, and J. F. Beacom. Role of Line-of-sight Cosmic-ray Interactions in Forming the Spectra of Distant Blazars in TeV Gamma Rays and High-energy Neutrinos. *ApJ*, 731:51, April 2011.
- [53] W. Essey and A. Kusenko. A new interpretation of the gamma-ray observations of distant active galactic nuclei. *Astroparticle Physics*, 33:81–85, March 2010.
- [54] F. Aharonian, W. Essey, A. Kusenko, and A. Prosekin. TeV gamma rays from blazars beyond $z=1$? *Phys. Rev. D*, 87(6):063002, March 2013.
- [55] F. A. Aharonian, P. S. Coppi, and H. J. Voelk. Very high energy gamma rays from active galactic nuclei: Cascading on the cosmic background radiation fields and the formation of pair halos. *Ap. J. Letters*, 423:L5–L8, March 1994.
- [56] V. S. Berezhinsky and A. I. Smirnov. Cosmic neutrinos of ultra-high energies and detection possibility. *Astrophys. Space Sci.*, 32:461–482, February 1975.
- [57] P. S. Coppi and F. A. Aharonian. Constraints on the Very High Energy Emissivity of the Universe from the Diffuse GeV Gamma-Ray Background. *Ap. J. Letters*, 487:L9, September 1997.
- [58] O. E. Kalashev, D. V. Semikoz, and G. Sigl. Ultrahigh energy cosmic rays and the GeV-TeV diffuse gamma-ray flux. *Phys. Rev. D*, 79(6):063005, March 2009.
- [59] S. Gabici and F. A. Aharonian. Gamma ray signatures of ultra high energy cosmic ray accelerators: electromagnetic cascade versus synchrotron radiation of secondary electrons. *Astrophys. Space Sci.*, 309:465–469, June 2007.
- [60] F. A. Aharonian. Proton-synchrotron radiation of large-scale jets in active galactic nuclei. *MNRAS*, 332:215–230, May 2002.
- [61] S. Gabici and F. A. Aharonian. Pointlike Gamma Ray Sources as Signatures of Distant Accelerators of Ultrahigh Energy Cosmic Rays. *Physical Review Letters*, 95(25):251102, December 2005.

- [62] A. Y. Prosekin, S. R. Kelner, and F. A. Aharonian. Non-variable cosmologically distant gamma-ray emitters as a propagation imprint of ultra-high-energy protons. *Astr. Ap.*, 536:A30, December 2011.
- [63] L. Eyges. Multiple Scattering with Energy Loss. *Physical Review*, 74:1534–1535, November 1948.
- [64] V. S. Remizovich, D. B. Rogozkin, and M. I. Riazanov. *Charged Particles Path-Length Fluctuation*. Energoatomizdat, Moscow, 1988.
- [65] F. A. Aharonian, A. N. Timokhin, and A. V. Plyasheshnikov. On the origin of highest energy gamma-rays from Mkn 501. *Astr. Ap.*, 384:834–847, March 2002.
- [66] R. J. Protheroe and P. L. Biermann. A new estimate of the extragalactic radio background and implications for ultra-high-energy gamma-ray propagation. *Astroparticle Physics*, 6:45–54, December 1996.
- [67] C. Alcock and S. Hatchett. The effects of small-angle scattering on a pulse of radiation with an application of X-ray bursts and interstellar dust. *ApJ*, 222:456–470, June 1978.
- [68] A. Crusius and R. Schlickeiser. Synchrotron radiation in random magnetic fields. *Astr. Ap.*, 164:L16–L18, August 1986.
- [69] A. Franceschini, G. Rodighiero, and M. Vaccari. Extragalactic optical-infrared background radiation, its time evolution and the cosmic photon-photon opacity. *Astr. Ap.*, 487:837–852, September 2008.
- [70] W. B. Atwood, A. A. Abdo, M. Ackermann, W. Althouse, B. Anderson, M. Axelsson, L. Baldini, J. Ballet, D. L. Band, G. Barbiellini, and et al. The Large Area Telescope on the Fermi Gamma-Ray Space Telescope Mission. *ApJ*, 697:1071–1102, June 2009.
- [71] B. D. Lehmer, W. N. Brandt, D. M. Alexander, F. E. Bauer, D. P. Schneider, P. Tozzi, J. Bergeron, G. P. Garmire, R. Giacconi, R. Gilli, G. Hasinger, A. E. Hornschemeier, A. M. Koekemoer, V. Mainieri, T. Miyaji, M. Nonino, P. Rosati, J. D. Silverman, G. Szokoly, and C. Vignali. The Extended Chandra Deep Field-South Survey: Chandra Point-Source Catalogs. *ApJS*, 161:21–40, November 2005.
- [72] P. Romano, S. Campana, R. P. Mignani, A. Moretti, M. Mottini, M. R. Panzera, and G. Tagliaferri. The Brera multi-scale wavelet Chandra survey. I. Serendipitous source catalogue. *Astr. Ap.*, 488:1221–1236, September 2008.

- [73] S. R. Kelner, A. Y. Prosekin, and F. A. Aharonian. Mechanics and kinetics in the Friedmann-Lemaître-Robertson-Walker space-times. *Phys. Rev. D*, 84(4):044016, August 2011.
- [74] W. Essey and A. Kusenko. On Weak Redshift Dependence of Gamma-Ray Spectra of Distant Blazars. *Ap. J. Letters*, 751:L11, May 2012.
- [75] A. M. Taylor, M. Ahlers, and F. A. Aharonian. Need for a local source of ultrahigh-energy cosmic-ray nuclei. *Phys. Rev. D*, 84(10):105007, November 2011.
- [76] K. Katarzyński, G. Ghisellini, F. Tavecchio, J. Gracia, and L. Maraschi. Hard TeV spectra of blazars and the constraints to the infrared intergalactic background. *MNRAS*, 368:L52–L56, May 2006.
- [77] F. W. Stecker and S. T. Scully. The spectrum of 1ES0229 + 200 and the cosmic infrared background. *Astr. Ap.*, 478:L1–L3, January 2008.
- [78] E. Lefa, F. M. Rieger, and F. Aharonian. Formation of Very Hard Gamma-Ray Spectra of Blazars in Leptonic Models. *ApJ*, 740:64, October 2011.
- [79] F. A. Aharonian, D. Khangulyan, and L. Costamante. Formation of hard very high energy gamma-ray spectra of blazars due to internal photon-photon absorption. *MNRAS*, 387:1206–1214, July 2008.
- [80] A. de Angelis, M. Roncadelli, and O. Mansutti. Evidence for a new light spin-zero boson from cosmological gamma-ray propagation? *Phys. Rev. D*, 76(12):121301, December 2007.
- [81] D. Horns and M. Meyer. Indications for a pair-production anomaly from the propagation of VHE gamma-rays. *J. Cosmol. Astropart. Phys.*, 2:33, February 2012.
- [82] R. J. Protheroe and H. Meyer. An infrared background-TeV gamma-ray crisis? *Physics Letters B*, 493:1–6, November 2000.
- [83] K. Murase, C. D. Dermer, H. Takami, and G. Migliori. Blazars as Ultra-high-energy Cosmic-ray Sources: Implications for TeV Gamma-Ray Observations. *ApJ*, 749:63, April 2012.
- [84] S. Razzaque, C. D. Dermer, and J. D. Finke. Lower Limits on Ultrahigh-energy Cosmic Ray and Jet powers of TeV Blazars. *ApJ*, 745:196, February 2012.

- [85] W. Essey, S. Ando, and A. Kusenko. Determination of intergalactic magnetic fields from gamma ray data. *Astroparticle Physics*, 35:135–139, October 2011.
- [86] H.E.S.S. Collaboration. VHE γ -ray emission of PKS 2155-304: spectral and temporal variability. *Astr. Ap.*, 520:A83, September 2010.
- [87] I. P. Williamson. Pulse broadening due to multiple scattering in the interstellar medium. *MNRAS*, 157:55, 1972.
- [88] K. Ichiki, S. Inoue, and K. Takahashi. Probing the Nature of the Weakest Intergalactic Magnetic Fields with the High-Energy Emission of Gamma-Ray Bursts. *ApJ*, 682:127–134, July 2008.
- [89] K. Murase, K. Takahashi, S. Inoue, K. Ichiki, and S. Nagataki. Probing Intergalactic Magnetic Fields in the GLAST Era through Pair Echo Emission from TeV Blazars. *Ap. J. Letters*, 686:L67–L70, October 2008.
- [90] A. P. Szabo and R. J. Protheroe. Implications of particle acceleration in active galactic nuclei for cosmic rays and high energy neutrino astronomy. *Astroparticle Physics*, 2:375–392, October 1994.
- [91] C. D. Dermer, M. Cavadini, S. Razzaque, J. D. Finke, J. Chiang, and B. Lott. Time Delay of Cascade Radiation for TeV Blazars and the Measurement of the Intergalactic Magnetic Field. *Ap. J. Letters*, 733:L21, June 2011.
- [92] F. Aharonian et al. A low level of extragalactic background light as revealed by γ -rays from blazars. *Nature*, 440:1018–1021, April 2006.
- [93] R. C. Gilmore, R. S. Somerville, J. R. Primack, and A. Domínguez. Semi-analytic modelling of the extragalactic background light and consequences for extragalactic gamma-ray spectra. *MNRAS*, 422:3189–3207, June 2012.
- [94] L. Costamante. Constraints on the optical-IR extragalactic background from γ -ray absorption studies. In R. J. Tuffs and C. C. Popescu, editors, *IAU Symposium*, volume 284 of *IAU Symposium*, pages 420–428, August 2012.
- [95] F. Tavecchio, G. Ghisellini, G. Ghirlanda, L. Costamante, and A. Franceschini. The hard TeV spectrum of 1ES 0229+200: new clues from Swift. *MNRAS*, 399:L59–L63, October 2009.
- [96] F. Aharonian et al. (HESS Collaboration). New constraints on the mid-IR EBL from the HESS discovery of VHE γ -rays from 1ES 0229+200. *Astr. Ap.*, 475:L9–L13, November 2007.

- [97] J. Aleksić et al. (MAGIC Collaboration). MAGIC Observations and multiwavelength properties of the quasar 3C 279 in 2007 and 2009. *Astr. Ap.*, 530:A4, June 2011.
- [98] S. V. Bogovalov and F. A. Aharonian. Very-high-energy gamma radiation associated with the unshocked wind of the Crab pulsar. *MNRAS*, 313:504–514, April 2000.
- [99] F. Aharonian, D. Khangulyan, and D. Malyshev. Cold ultrarelativistic pulsar winds as potential sources of galactic gamma-ray lines above 100 GeV. *Astr. Ap.*, 547:A114, November 2012.
- [100] O. Zacharopoulou, D. Khangulyan, F. A. Aharonian, and L. Costamante. Modeling the Hard TeV Spectra of Blazars 1ES 0229+200 and 3C 66A with an Internal Absorption Scenario. *ApJ*, 738:157, September 2011.
- [101] T. Kifune. Invariance Violation Extends the Cosmic-Ray Horizon? *Ap. J. Letters*, 518:L21–L24, June 1999.
- [102] F. W. Stecker and S. L. Glashow. New tests of Lorentz invariance following from observations of the highest energy cosmic γ -rays. *Astroparticle Physics*, 16:97–99, October 2001.
- [103] U. Jacob and T. Piran. Inspecting absorption in the spectra of extra-galactic gamma-ray sources for insight into Lorentz invariance violation. *Phys. Rev. D*, 78(12):124010, December 2008.
- [104] M. Simet, D. Hooper, and P. D. Serpico. Milky Way as a kiloparsec-scale axion-scope. *Phys. Rev. D*, 77(6):063001, March 2008.
- [105] A. Prosekin, W. Essey, A. Kusenko, and F. Aharonian. Time Structure of Gamma-Ray Signals Generated in Line-of-sight Interactions of Cosmic Rays from Distant Blazars. *ApJ*, 757:183, October 2012.
- [106] P. L. Biermann and P. A. Strittmatter. Synchrotron emission from shock waves in active galactic nuclei. *ApJ*, 322:643–649, November 1987.
- [107] A.-C. Davis, M. Lilley, and O. Törnkvist. Relaxing the bounds on primordial magnetic seed fields. *Phys. Rev. D*, 60(2):021301, July 1999.
- [108] D. Grasso and H. R. Rubinstein. Magnetic fields in the early Universe. *Phys. Rep.*, 348:163–266, July 2001.

- [109] A. Kandus, K. E. Kunze, and C. G. Tsagas. Primordial magnetogenesis. *Phys. Rep.*, 505:1–58, August 2011.
- [110] V. Berezhinsky, A. Z. Gazizov, and S. I. Grigorieva. Signatures of AGN model for UHECR. *ArXiv Astrophysics e-prints*, October 2002.
- [111] A. A. Abdo et al. Bright Active Galactic Nuclei Source List from the First Three Months of the Fermi Large Area Telescope All-Sky Survey. *ApJ*, 700:597–622, July 2009.
- [112] E. Prandini, G. Bonnoli, and F. Tavecchio. Estimating the redshift of PKS 0447-439 through its GeV-TeV emission. *Astr. Ap.*, 543:A111, July 2012.
- [113] A. Zech, B. Behera, Y. Becherini, C. Boisson, B. Giebels, M. Hauser, M. A. Kastendieck, S. Kaufmann, K. Kosack, J. P. Lenain, M. de Naurois, M. Punch, M. Raue, H. Sol, S. Wagner, and H.E.S.S. Collaboration. Discovery of VHE emission from PKS 0447-439 with H.E.S.S. and MWL studies. In *25th Texas Symposium on Relativistic Astrophysics*, 2010.
- [114] H. Landt. Optical spectroscopy of the γ -ray bright blazars PKS 0447-439 and PMN J0630-24. *MNRAS*, 423:L84–L86, June 2012.
- [115] S. Pita, P. Goldoni, C. Boisson, Y. Becherini, L. Gérard, J.-P. Lenain, and M. Punch. High energy blazars spectroscopy with X-shooter on the VLT. In F. A. Aharonian, W. Hofmann, and F. M. Rieger, editors, *American Institute of Physics Conference Series*, volume 1505 of *American Institute of Physics Conference Series*, pages 566–569, December 2012.
- [116] M. Fumagalli, A. Furniss, J. M. O’Meara, J. X. Prochaska, D. A. Williams, and E. P. Farina. On the redshift of the blazar PKS 0447-439. *Astr. Ap.*, 545:A68, September 2012.
- [117] G. Ghisellini. Extragalactic relativistic jets. In F. A. Aharonian, W. Hofmann, and F. M. Rieger, editors, *American Institute of Physics Conference Series*, volume 1381 of *American Institute of Physics Conference Series*, pages 180–198, September 2011.
- [118] K. Murase, J. F. Beacom, and H. Takami. Gamma-ray and neutrino backgrounds as probes of the high-energy universe: hints of cascades, general constraints, and implications for TeV searches. *J. Cosmol. Astropart. Phys.*, 8:30, August 2012.

- [119] S. Kelner and F. Aharonian. Small pitch-angle magnetobremsstrahlung in inhomogeneous curved magnetic fields. *ArXiv e-prints*, July 2012.
- [120] H. Alfven and C. G Falthammar. *Cosmical Electrodynamics*. Oxford University Press, 1963.
- [121] L. D. Landau and E. M. Lifshitz. *The Classical Theory of Fields*. Butterworth-Heinemann, Oxford, 1975.
- [122] K. S. Cheng, C. Ho, and M. Ruderman. Energetic radiation from rapidly spinning pulsars. I - Outer magnetosphere gaps. II - VELA and Crab. *ApJ*, 300:500–539, January 1986.
- [123] B. A. Trubnikov. Conservation Law for the Binormal Momentum in the Presence of Charge Drift in a Magnetic Field. *Soviet Journal of Experimental and Theoretical Physics*, 91:479–482, September 2000.
- [124] Julian Schwinger. On the classical radiation of accelerated electrons. *Phys. Rev.*, 75:1912–1925, Jun 1949.
- [125] V. B. Berestetskii, E. M. Lifshitz, and L. P Pitaevskii. *Quantum Electrodynamics*. Butterworth-Heinemann, Oxford, 1982.
- [126] J. Takata, S. Shibata, and K. Hirotani. A pulsar outer gap model with trans-field structure. *MNRAS*, 354:1120–1132, November 2004.
- [127] K. Hirotani. Outer-Gap versus Slot-Gap Models for Pulsar High-Energy Emissions: The Case of the Crab Pulsar. *Ap. J. Letters*, 688:L25–L28, November 2008.
- [128] A. Levinson. Particle Acceleration and Curvature TeV Emission by Rotating, Supermassive Black Holes. *Physical Review Letters*, 85:912–915, July 2000.
- [129] V. N. Bayer, V. M. Katkov, and V. S. Fadin. *Radiation of Relativistic Electrons*. Atomizdat, Moscow, 1973.